Surface acoustic wave assisted chemical reactions to produce hydrogen gas

Dissertation

zur Erlangung des akademischen Grades
Dr. rer. nat.

eingereicht an der
Mathematisch-Naturwissenschaftlich-Technischen Fakultät
der Universität Augsburg

von

Sixuan Wang

Augsburg, Juli 2020

Erstgutachter: Prof. Dr. Achim Wixforth
Zweitgutachter: Prof. Dr. Ursula Wurstbauer
Tag der mündlichen Prüfung: 26.10.2020

Acknowledgements

First, I would like to express my sincere appreciation to my major professor Dr. Achim Wixforth to give me the opportunity to work on this PhD project. His knowledge and valuable guidance helped me a lot in this thesis work.

Then, I would like to also acknowledge Dr. Christoph Westerhausen and Dr. Rudolf Herrmann for their guidance and support in the lab work, such as atomic force microscopy measurements and scanning electron microscopy measurements.

It was pleasure to work with such supportive and helpful people at the chair of experimental physics I. I would like to especially thank Lukas G. Schnitzler and Manuel Brugger for supporting me in micro lithographical fabrication, and I would like to extend my appreciation to Mathis Eggle-Sievers for his home-made temperature sensor. I also acknowledge Mathias Küß for all his helpful discussions about surface acoustic waves, also Andreas Hörner and Andreas Spörhase for their help with my setups. Additionally, I also appreciate Alexander Reiner for his support.

Moreover, I would like to thank for the financial support from the European Union's 2020 research and innovation program under the Marie Sklodowska-Curie grant agreement No 642688. It was nice to meet all the ERS fellows in every training network. Particularly I would like to thank my SAW train co-supervisor Dr. Cinzia Caliendo for all the support during my secondments at the CNR Rome, and for the helpful guidance on the Matlab code to calculate SAW velocities.

Thanks to Prof. Dr. Ursula Wurstbauer and Elmar Mitterreiter from Technical University of Munich. The cooperation with you was crucial for the electrochemical part of my project.

Finally, I would like to thank my friends and family back in China for all the moral support extending across time zones. Special my parents for their unconditional love, to whom I dedicate this thesis report.

Contents

Abstract

This thesis addresses the application of Rayleigh type acoustic waves on the chemical hydrogen production reaction and studies the mechanism behind the reaction promoted by surface acoustic waves (SAW). TiO_2 is the most widely used photocatalyst for the water splitting reaction to generate clean fuel of hydrogen, but the energy conversion efficiency of it is still low, mainly due to the easy recombination of photo-generated electron/hole pairs. In order to promote the efficiency of the catalyst, a device type catalyst with controllable SAW functions is designed in this experiment by employing a 128°y-cut $LiNbO_3$ substrate to generate Rayleigh-type SAW with a frequency of 150MHz under a Pt modified TiO_2 catalyst. The effect of SAW on the activation of the Pt/TiO_2 catalyst for the hydrogen production from the photo-splitting of a gaseous methanol/water mixture was examined by an indirect formaldehyde production. The experimental results convincingly show that the photo-dehydrogenation of methanol is clearly enhanced by the SAW propagation on the deposited Pt/TiO_2 catalyst film, and exhibits a nonlinear positive relationship with the SAW power. The mechanism of the surface acoustic wave excitation effect on the catalyst is accounted for the electric field produced by the displacement of the $LiNbO_3$, which hinders the recombination of photo-generated electron/hole pairs.

Besides the photocatalysis water splitting reaction, electrolysis of water is an attractive energy generation method to obtain hydrogen gas. However, the most efficient catalyst for this reaction is Pt, which makes this approach expensive. Thereby, there are many studies focusing on enhancing the hydrogen producing efficiency of other inexpensive catalysts. In this study, an Au electrode and Au supported Pt/TiO_2 electrode were chosen as non-Pt catalyst for the electrochemical hydrogen evolution reaction (HER) in acidic solution, and a 70MHz Rayleigh type SAW was used to promote the HER. The results demonstrate that SAW application has a tunable effect on these electrodes. Under the influence of the SAW, they exhibit a better HER activity with a higher current density, whereas the promotion effect disappears immediately when the SAW is turned off. Moreover, the bigger exchange current density and the decreased overpotential indicate a better catalytic activity of these catalysts under influence of SAW, and this positively relates with the applied SAW power level. Analyzing the Tafel equation and the recorded current with/without the effect of SAW suggests that the enhanced HER activity of these catalysts can be attributed to the SAW-induced microstreaming effect, which could dissipate the electric double layer near the electrode surface, thus minimizing the required work

for transferring protons through the Helmholtz layer, and finally lead to a decrease of the free energy of activation for the hydrogen evolution reaction. This study might be a first step towards extensive combination of SAW with different catalysts for the electrochemical hydrogen production.

Chapter 1
Photocatalysis and TiO_2

In this present chapter, we first introduce the energy and environment problem we have to face in the future. Here, the photocatalysis water splitting reaction represents a promising method to solve these problems, because it could produce hydrogen gas, the most environmentally friendly energy fuel. Then, basic information about the mechanism of photocatalysis and a detailed description of the property of TiO_2 will be presented. Afterwards, we will focus on the phototcatalysis water splitting reaction and the enhancement method by using Pt modified TiO_2 and using methanol as sacrifice material.

1.1 Energy crisis and environment problem

Energy and environmental issues at a global level are important topics. The consumption of energy increases with the promotion of technology and rapid human population growth. Currently, 85% of energy supply is coming from fossil fuel. Based on the current consumption rate, it is estimated that coal can be used for 400 more years, oil for 80 years and natural gas for 150 years. Moreover, a far more serious problem is the impact on the environment by using of fossil fuels, in particular CO_2, which contribute to global warming. Nowadays, The CO_2 level in the atmosphere has risen to 349ppm, and it still rises at a speed of 2ppm every year. According to the International Panel on Climate Change (IPCC), the average temperature will increase more than 2°C when the concentration of CO_2 is above 450ppm, and such temperature rise could cause adverse impact on human society and ecosystems [1, 2]. Because of this, it is indispensable to construct clean and sustainable energy systems to lessen our dependence on fossil fuel and reduce the exhaust of CO_2, although a multitude of power technologies have developed, solar technologies such as photovoltaics and photocatalysis are superior among them in the long term, because they directly convert energy from sunlight without having diverse effect on atmosphere. In the future, solar technology will possibly drive the transition from oil economy to solar economy.

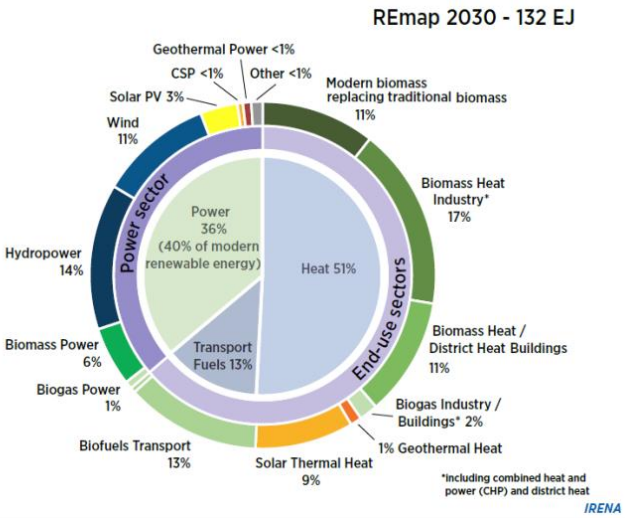

Fig. 1.1 Breakdown of global renewable energy use in REmap 2030, IRENA [3].

Solar energy is a renewable source, and it has enough earthbound energy potential. If the total solar irradiation would be all converted to usable energy by using current photovoltaic devices, it could generate about $2.05 \times 10^{25} J \cdot yr^{-1}$ usable energy, and it almost 4.5 times more than world's energy consumption in 2013 [4]. Thus, and very probable, solar energy will become an important component in the future. Since the solar power is intermittent because of clouds, seasons and the day – night cycle, we have to face the problem how to store the solar energy. One of the most attractive solution is to transfer solar energy into chemical energy, which is stored in the chemical bonds of chemical fuels. The advantage of chemical fuels is that they are relative stable and can be easily transported. The often used chemical fuels include methanol, hydrogen, methane and etc. Almost all such chemical fuels contain carbon except hydrogen, so after burning the chemical fuels which contains carbon, CO_2 will be emitted, a serious cause for the greenhouse effect. Based on this consideration, converting solar energy into hydrogen seems to be a more environmentally friendly method, because no pollution is emitted by burning hydrogen, and the gravimetric energy density of hydrogen is $143 MJ \cdot kg^{-1}$, which is higher than other chemical fuels [5].

Table 1.1 Gravimetric energy densities of several fuels (at 1 bar) [5].

Fuel	Gravimetric energy density ($MJ \cdot kg^{-1}$)
Methanol	20
Petrol	44
Diesel	46
Natural gas	54
Hydrogen	143

Hydrogen is a colorless and odorless gas, and it doesn't exist abundantly in nature, but it can be extracted from hydrogen containing compounds. Hydrogen is the most abundant element in the universe, 75% of the universe's mass consists of it, and the most abundant source of hydrogen on the earth is water. Water can be decomposed into oxygen and hydrogen. Thermodynamically, it is an uphill reaction under standard conditions, with 257kJ·mol^{-1} Gibbs free energy. A positive Gibbs energy change means this reaction cannot happen spontaneously.

$$2H_2O(l) + 4h^+ \leftrightarrow O_2(g) + 4H^+ \qquad E^0_{ox} = -1.229V \quad vs.\ NHE \tag{1.1}$$

$$4H^+(aq) + 4e^- \leftrightarrow 2H_2(g) \qquad E^0_{red} = 0.000V \quad vs.\ NHE \tag{1.2}$$

Equation (1.1) and (1.2) are water splitting half-reactions at standard concentrations (1mol/L, 1bar) and temperature (298K). Because $\Delta G = -n\Delta EF$, where n is the number of transferred electrons, and F is Faraday constant, the electrochemical voltage $\Delta E = -1.23V$ corresponds to a Gibbs free energy of +257kJ/mol.

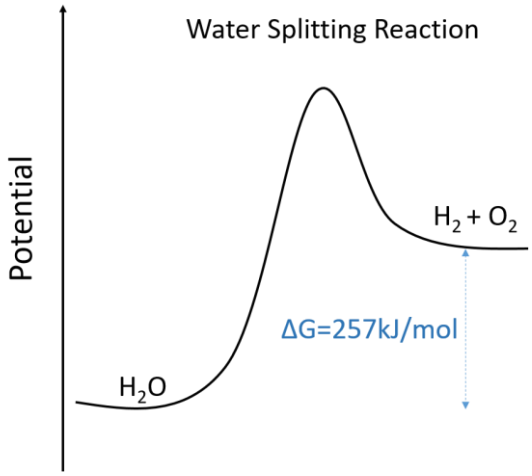

Fig. 1.2 energy scale of water splitting reaction.

In order to make a water splitting reaction to occur, enough energy to overcome the positive Gibbs free energy change should be supplied to the reaction system. Conventionally, there are at least three methods to achieve a water splitting reaction: One way is to thermolyse water by using extreme high temperatures, up to T=2200°C, so this method needs much heat energy [6]. An alternative method is to apply a sufficiently large electrical potential, more than 2.3V, to water, then hydrogen will be generated at the cathode and oxygen will be formed at the anode [7]. This method needs much electric energy, and the price of electric energy is relative expensive in many countries. Alternatively, energy could be also supplied by sunlight, where the light-responsive photocatalyst adsorbs the photon energy from the sunshine to excite electron-hole pairs [8]. The electron can reduce the water into hydrogen gas, and the hole will oxidize the water into oxygen gas under the condition that the energy of the photon exceeds

E=1.23eV at 0 pH. It is the most environmental friendly way to producing hydrogen because solar energy is a kind of free and abundant renewable source. As a result, the photocatalytic water splitting method has attracted much attention and it is being highly investigated these years. For the aspect of energy, it harvests and stores solar energy into chemical bonds of hydrogen and oxygen which are photocatalytical reaction products.

The water splitting reaction can be written as [9]:

$$2H_2O \xrightarrow{hv,photocatalyst,\ photoelectrode} 2H_2 + O_2 \quad (1.3)$$

The produced hydrogen and oxygen can be relative easily transported, which allows for convenient hauling and utilization of stored solar energy.

1.2 Theoretical concepts of photocatalysis

1.2.1 Photocatalysis process

The word photocatalysis composes of two parts: the prefix “photo” and the word “catalysis”, this means it needs light and a sort of catalyst in a photocatalytic reaction. A more scientific definition from the book is “a change in the rate of a chemical reaction or its initiation under the action of light radiation (ultraviolet, visible or infrared) in the presence of a substance or semiconductor (the photocatalyst) that adsorbs light continuously with interactions and regeneration of electron/holes during a photochemical activation” [10]. Photocatalytic reactions can happen homogeneously and heterogeneously, while most of the photocatalytic reactions occur heterogeneously because the commonly used catalyst are in solid phase and the reactant always in either gas or liquid phase. Heterogeneous photocatalysis is defined as the acceleration of a photoreaction in the presence of a photocatalyst in a different phase as the reactants. Mostly, semiconductor catalysts are used for photocatalysis reactions. There are two main applications for the heterogeneous photocatalysis: One is to actively clean polluted air or water, and another one is to produce hydrogen gas from water. Photocatalysis is ussally initiated by photoexcitation to generate electron-hole pairs, and then these charge carriers move to the surface of the photocatalyst to drive the chemical reaction. The life time of the charge carriers, the diffusion length and the crystallinity and particle size of the catalyst are very important factors for a successful photocatalysis.

The process of heterogeneous photocatalysis can be generally described into three steps:

1) Light harvesting

A semiconductor photocatalyst is illuminated by light where the photon energy of the light must be equal to or greater than its band gap energy. After absorbing the photon, the electrons can be excited from the valence band to the conduction band, leaving some positively charged holes in the valence band.

2) Charge carrier transfer and surface chemical reaction

Once the photogenerated electrons and holes are separated, they may and migrate to the surface of the semiconductor and the react with adsorbed species nearby. The transferred electron on the surface reduces some adsorbed species when the reduction ability of adsorbed species is lower than that of electron in conduction band; The transferred hole on the surface oxides the adsorbed species under the condition that the oxidation ability of adsorbed species is lower than that of hole on valence band [11].

3) Recombination of electron and hole

Recombination of electron and hole before reaching the surface can also occur, and this is a competition process with step (2). Some electrons and holes recombine during migration, and then release the adsorbed photon energy as heat or a phonon, depending on the band structure of the catalyst. As a result, reduction and oxidation reaction will be strongly reduced or not happen at all.

Understanding the fundamental processes in heterogeneous photocatalysis is thus an important issue, because it is crucial for further development of photocatalysis. In order to increase the efficiency of the photocatalyst, many approaches have been developed to effectively suppress the recombination of electrons and holes. Then, more electrons and holes can move to surface of the catalyst and subsequently react with adsorbed species such as water, oxygen, certain organic and inorganic substances.

1.2.2 Photocatalyst-TiO_2

Interest in heterogeneous photocatalysis can be traced back to the discovery of photo-electrochemically water splitting with a TiO_2 electrode by Fujishima and Hondain in 1972 [12]. From that time on, much research has been carried out to generate hydrogen from water in photocatalysis reaction by using various semiconductor catalysts. In a photocatalysis system,

the photocatalyst first should have suitable conduction and valence band levels. The bottom of the conduction band has to be more electronegative than the redox potential $\varphi(H^+/H_2)$, while the top level of valence band has to be more positive than the redox potential $\varphi(O_2/H_2O)$. Moreover, the width of the bandgap should not be too wide, otherwise the semiconductor photocatalyst cannot harvest the required energy of UV or even visible photons. In addition, a good catalyst should also have the property to be environmentally safe and robust against photocorrosion [11].

Table 1.2: band gap energy and corresponding radiation wavelength needed for the excitation of electron-hole pairs in different semiconductors [13].

Semiconductor	Band gap Energy (eV)	Wavelength (nm)
ZnS	3.6	344
ZnO	3.2	388
TiO_2(anatase)	3.2	388
TiO_2(rutile)	3.0	413
WO_3	2.8	443
CdS	2.4	517
Fe_2O_3	2.3	539
GaAs	1.4	886

Photocatalysis has been commercialized in recent years, and more and more companies sell functioning products employing a photocatalytic reaction to produce hydrogen or degrade poisonous pollutants from air and water [14]. Some of the most promising materials are metal oxide semiconductors, which exhibit good resistance to photo-corrosion and are usually water stable. Moreover, most metal dioxides show low toxicity and can be manufactured at low cost which is good for commercialization. Among various semiconductor photocatalysts, TiO_2 is the most suitable one for industrial usage, because it exhibits a relative good photoactivity, high stability in water, even in solutions with a wide range of pH value, and can be produced at low cost. Moreover, it is very safe to humans since it has been used as a kind of white pigment from ancient time to nowadays. On the other side, the majority disadvantage of TiO_2 photocatalyst is its wide bandgap (around $E_G \approx 3.0$ eV [13]), i.e., the photon wavelength must be less than 410nm for proper function. This large band gap leads to the fact that it can only be excited by UV light. However, the UV part of the solar spectrum adds only about 5%-8% of to the available intensity of natural sunlight [15]. Another drawback is its low absorption coefficient, since TiO_2 represents an indirect band semiconductor.

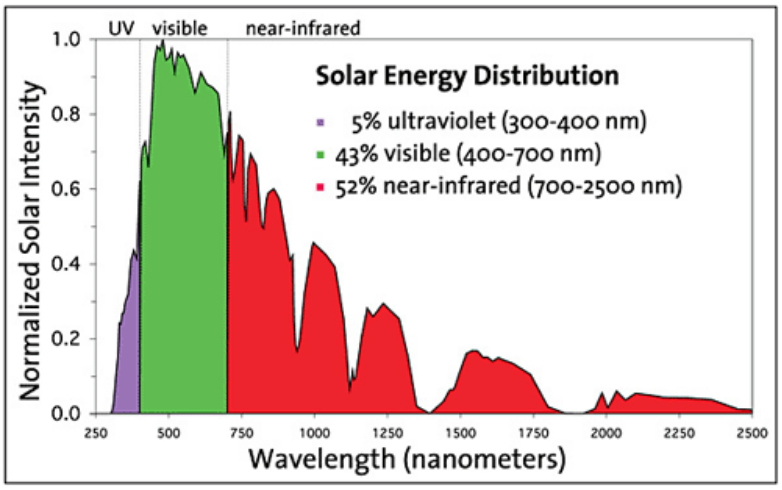

Fig. 1.3 Natural solar energy spectrum distribution [16].

TiO_2 exists mainly in three different crystalline structures: anatase, rutile and brookite, and the physical properties of these three types of TiO_2 crystal are different. Some physical properties of the commonly used Rutile and Anatase phase TiO_2 are depicted in Table 1.3.

Table 1.3 some physical properties of rutile TiO_2 and anatase TiO_2 [13]

Properties at 298K	Rutile	Anatase
Density/ $g \cdot cm^{-3}$	4.250	3.894
Specific heat / $J \cdot K \cdot mol^{-1}$	55.06	55.52
Refractive index	2.616	2.554
Relative permittivity, ε(0)	167, 86	30
Bandgap energy (eV)	3.0 (direct)	3.8(direct), 3.2(indirect)
Effective mass (hole)	20	0.8
Mobility / $cm^2 \cdot v^{-1} \cdot s^{-1}$	0.1	4-20
Isoelectric point	5.6	6.1

In TiO_2, the distance between the Ti atom and the O atom is about 195pm, and the stable ionic states of Ti is Ti^{4+} and the stable ionic states of O is O^{2-}. The ionic radii of Ti^{4+} and O^{2-} are 74pm and 122pm, respectively [13]. The ratio of ionic radii is thus $\frac{Ti^{4+}}{O^{2-}} = \frac{74}{122} = 0.59$, so like most metal oxides, the crystalline structure of TiO_2 resides in the 6-coordinate structure, in which the O^{2-} is closely located at the six apices of a regular octahedron, and the Ti^{4+} is located at the center of it. The crystalline structure of TiO_2 is represented by a regular octahedron as a basic unit. The structures of anatase, rutile and brookite phases can be described as distorted TiO_6 octahedral with different arrangements or symmetries (Fig. 1.5). The length of the Ti-O bonds plays a very important role in the structural and electronic features of the different phases

of TiO_2. Rutile is the most stable phase, while brookite and anatase are the metastable forms, and they are readily transformed to rutile phase at a certain temperature.

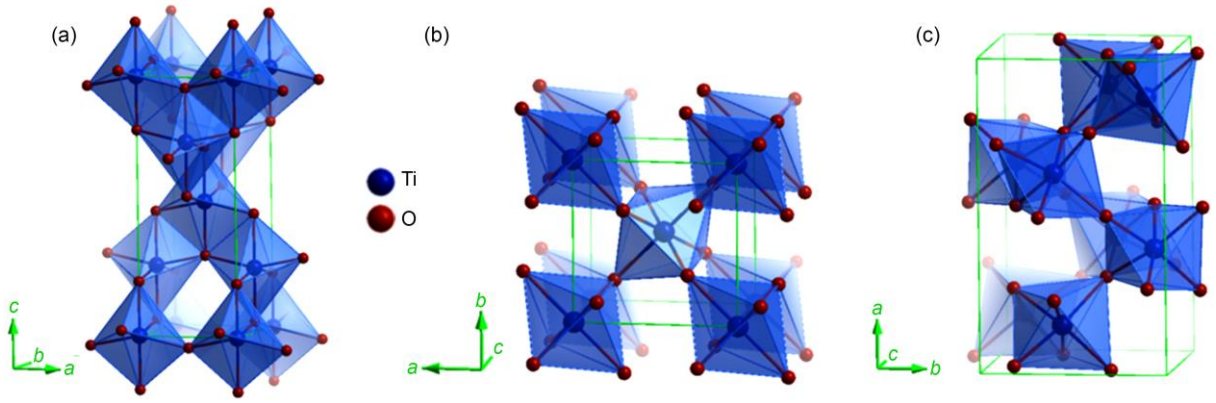

Fig. 1.5 Representations of the TiO_2 (a) Anatase, (b) Rutile, and (c) Brookite forms. Anatase (tetragonal, a = 0.3785 nm, c = 0.9513 nm), Rutile (tetragonal, a = 0.4593 nm, c = 0.2959 nm), and Brookite (orthorhombic, a = 0.9181 nm,b = 0.5455 nm, c = 0.5142 nm)[17]

It is well known that the structure and microstructure of TiO_2 crystal decides about its photoactive properties [13]. The bonding character of metal oxides is highly polar or even ionic, so that the electrons are almost localized. The electronic structure of the Ti atom can be described as Ti: $1s^2 2s^2 2p^6 3s^2 3p^6 3d^2 4s^2$; and the electronic structure of the oxygen atom can be described as O: $1s^2 2s^2 2p^4$. Fig. 1.6 clearly shows the chemical bonds are formed not only by overlap between the O and Ti orbitals but also the hybridization between them. In general, in the bulk of TiO_2, the conduction bands (CB) of anatase, rutile and brookite TiO_2 are mostly composed by the 2p orbital of the oxygen atom, and the valence bands (VB) of TiO_2 are mostly composed by 3d orbital of the titanium atom. However, at the surface of the TiO_2 material, free electrons in TiO_2 are sometimes trapped by Ti^{4+}, where they reduce Ti^{4+} to Ti^{3+}. This is different from bulk TiO_2, because the electronic structure is distorted at the surface due to disruption of the lattice symmetry.

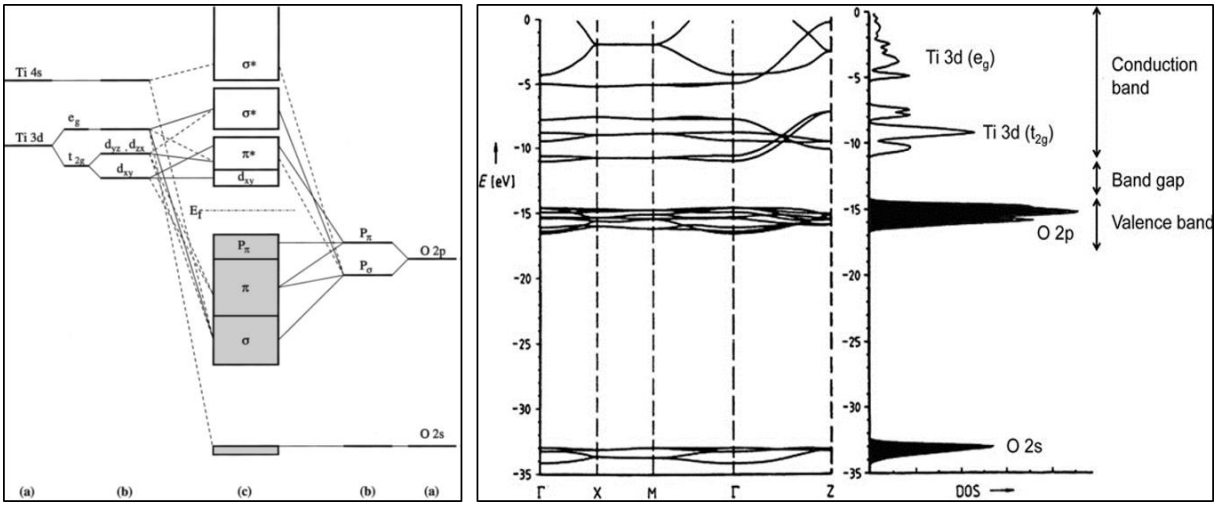

Fig. 1.6 left panel: Molecular orbital structure for anatase TiO_2: (a) is atomic levels, (b) is crystal-field split levels, and (c) is final interaction states. The thin-solid and dashed lines represent large and small contributions [18]. Right panel depicts the electronic band structure E-k curves and density-of-states (DOS) of rutile TiO_2. The black parts of the DOS indicate completely filled bands. (Adapted from Hoffmann [19], pp. 31, copyright Wiley- VCH Verlag GmbH & Co. KGaA. Reproduced with permission)

The electronic band structure is depicted in figure 1.6, which shows a fairly horizontally oriented, flat dispersion. The electronic band structure provides three information: the first one is the nature of the optical transition which depends on the type of band (direct band or indirect band); The second one is the effective mass influencing the charge mobility, because the effective mass relates to the curvature of the band like $m^* = \frac{h^2}{\partial^2 E / \partial k^2}$, and the charge mobility relates to the effective mass $\mu = \frac{q \cdot \tau}{m^*}$. The mobility of charge carrier in TiO_2 is very small, because compared to the s orbital and the p orbital, the 3d orbital of the transition metal Ti is fairly contracted and shows less overlap with neighboring atoms. Less overlap between atomic wave functions in turn leads to a narrow bandwidth, and also results in hindered electron or hole transport through the material; The third information that can be drawn from the band structure is the density of states (DOS). It represents the number of allowed electronic states per unit energy interval. From the DOS one can identify various bands and band widths, since the highest DOS occurs at energies where the E-k curve is flat. Moreover, the DOS can give a rough impression of the optical transition probability between different bands according to Fermi's golden rule [19].

1.3 Photocatalytic water splitting

1.3.1 Mechanism of water splitting process

Heterogeneous photocatalysis methods have been studied for water/air purification before, and in recent years, it was used to produce hydrogen gas due to environmentally friendly and its low cost. Normally, a photocatalyst is used to absorb the photon energy which is equal or greater than its band gap in a photocatalytic reaction. The band structure, including the bandgap, the position of the band edges of the conduction band and the valence band with respect to a vacuum level, are important parameters. This is because the bandgap determines the light adsorption properties and the potentials of the CB and VB's band edges determine the thermodynamic feasibility of a redox reaction that can happen at the surface of the photocatalyst. For catalysis, in order to obtain a fast reaction rate, it is critical to provide an overpotential [11] to drive the

electron transfer and to initiate a redox reaction. This is consistent with the fact that the lowest edge of the conduction band should be higher than the redox potential of $\varphi(H^+/H_2)$ and the highest edge of valence band should be lower than the redox potential of $\varphi(O_2/H_2O)$. Then, the electron transfer will be thermodynamically favorable, as it is shown in Fig. 1.7.

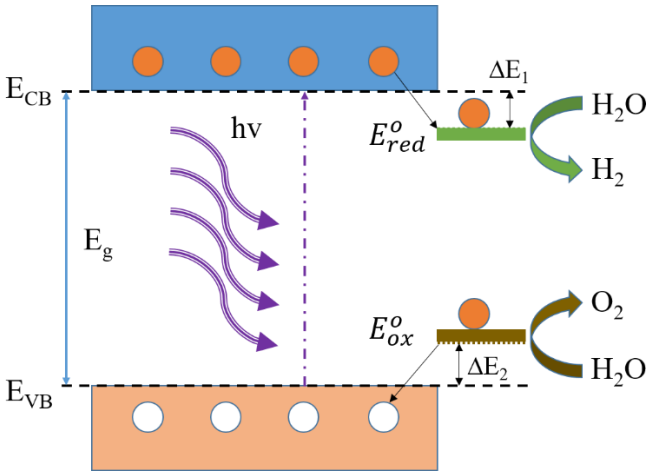

Fig. 1.7 Thermodynamic favor of the electron transfer between a water molecule and the conduction/valence band. ΔE_1 represents the kinetic overpotential of the reduction process and ΔE_2 represents the kinetic overpotential of the oxidation process.

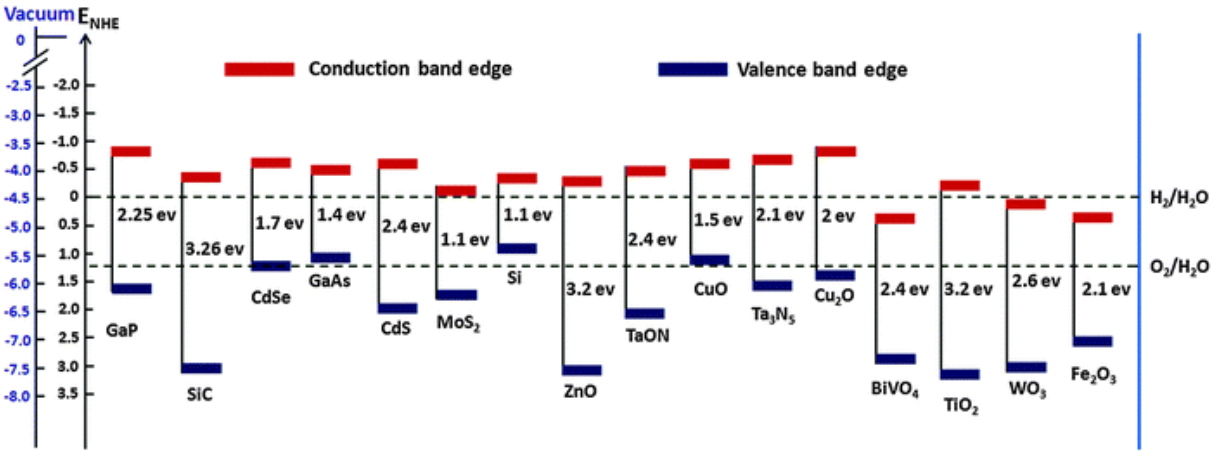

Fig. 1.8 Band edge positions of various semiconductors in contact with an aqueous electrolyte at pH = 0 relative to NHE (standard hydrogen electrode) and the vacuum level. For comparison the HER and OER redox potentials are also presented [20].

After adsorbing a photon in the catalyst, some electrons are excited from the valence band into the conducting band and leave holes in the valence band behind.

$$TiO_2 + hv \rightarrow e^-(TiO_2) + h^+(TiO_2) \tag{1.6}$$

Then, the resulting electron-hole pairs can migrate to the surface of the catalyst to initiate a redox reaction with any adsorbed water molecules. In detail, these photo-generated election-hole pairs are further involved in the following processes:

(1) the charge carriers diffuse to the surface of the TiO_2, and then transfer to an adsorbed water molecule. In the water splitting reaction, four holes being generated in the valence band are used to oxidize one water molecule, which means that a four-step oxidation from water to oxygen is involved. This process is shown in Fig. 1.9 below. On the other hand, one excited electron interacting with a hydrogen ion forms one H· radical. Two H· radicals combining with each other and then may form hydrogen gas. Thus, water is split into oxygen gas and hydrogen gas. The water oxidation is often the bottleneck for the overall water splitting reaction, because it requires multiple intermediate steps which involve a four-electron transfer and reaction. Moreover, the water oxidation kinetically competes with the fast electron-hole recombination, surface oxygen adsorption, and self-oxidation of the TiO_2 catalyst. The major drawback for TiO_2 nanoparticle catalysts is that both oxidation and reduction takes place on the same site of the material, which enhances the backward reaction, namely converting O_2 and H_2 back to H_2O. This situation also inadvertently facilitates short-circuit reactions, such as the parasitic reduction of oxygen to superoxide instead of the transition of protons to hydrogen gas. There is also an additional concern about a potentially explosive mixture of H_2 and O_2 in the same space.

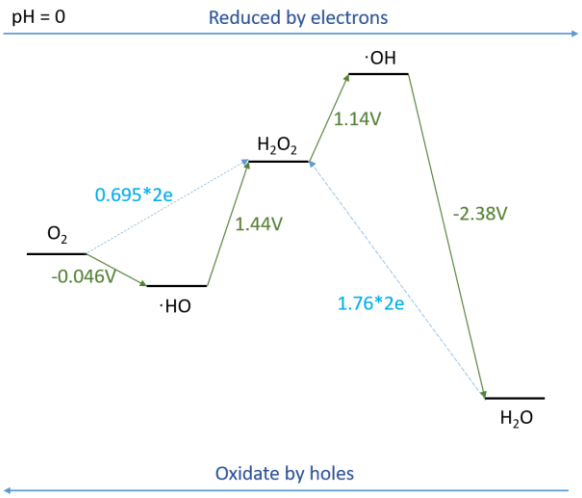

Fig. 1.9 Relative free energy change during the process of water is oxidized into oxygen, and the energy is in unite of eV [11].

(2) The charge carriers can be trapped either by surface defects or bulk defect sites in the TiO_2, and subsequently form trapped electrons and trapped holes respectively. Electrons are trapped at the Ti sites in the TiO_2 lattice where the Ti^{4+} is then reduced to Ti^{3+} [21]. During the trapping process, the electrons lose around 0.5eV of energy. The holes, on the other hand, prefer to stay

at the site of an under-coordinated surface oxygen atom, where the trapped holes were assigned to Ti-O· on the TiO_2 lattice. This is because the Ti-O-Ti bond traps the hole first and then dissociates to form Ti-O·[22]. The described electron trapping can prolong the lifetime of the hole and thus promote the hole photochemistry reaction. Moreover, although the defect can help to separate the electron and the hole, it can also serve as an electron and hole recombination site. Charge recombination and charge separation /migration are two competitive processes inside the TiO_2 semiconductor catalyst, and these processes affect the efficiency of photocatalytic reactions. Similar to the other semiconductors, the fast electron-hole recombination is the main reason for the low photocatalytic efficiency of TiO_2. Electrons and holes recombine and release their energy in form of photon or phonon. Usually, recombination is what we don't want, since it reduces the chance for charge carriers to initiate the desired photocatalytic reaction.

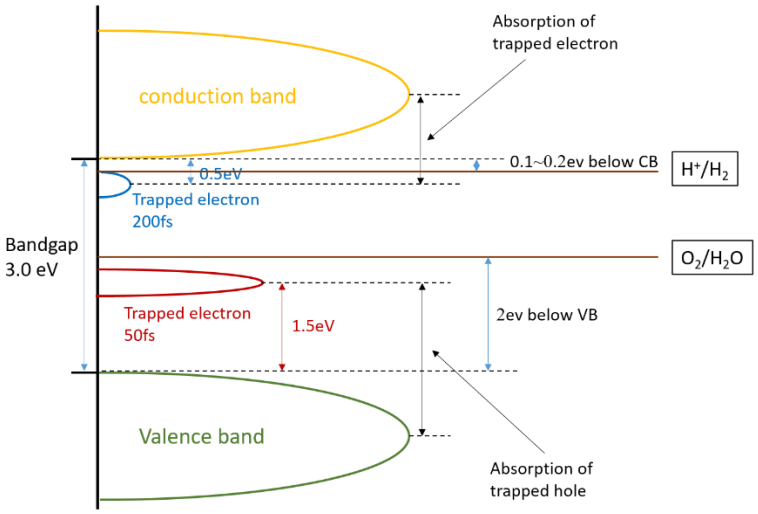

Fig. 1.10 Schematic illustration energy levels of trapped carriers and corresponding absorption bands, as being obtained by measuring transient absorption spectra for a TiO_2 film [11].

Some questions still remain open: How exactly do the charge carriers transfer through the lattice to reach the catalyst's surface, and what are the relative time scales for charge carrier transport, trapping and reaction?

Yamakata and coworkers observed water splitting reaction kinetics on a TiO_2 catalyst by using time-resolved IR absorption spectroscopy [23]. They found that the photogenerated holes immediately (within 2 μs) oxidized the water when 10 Torr H_2O vapor was exposed to bare TiO_2. The photogenerated electrons are trapped in shallow midgap states as described above and gradually reduced the water molecules in a time range between 10 μs and 900 μs. These

reactions compete with the undesired electron-hole recombination, which has a much faster time scale from 0.1μs to 0.3s (measured in vacuum) [23].

With regard to water and air cleaning and remediation, the holes in the valence band (VB) are very important because they induce the oxidative decomposition of possible environmental pollutants. In some recent research [24,25] it has been show that the positive holes in the valence band can directly oxidize organic or inorganic pollutants, but most of this research also reveals that the mechanism of the oxidation process is quite complex. First, the holes react with adsorbed water or hydroxide ions (OH^-) to produce a hydroxyl radical (·OH). This hydroxyl radical is a very strong oxidant with an oxidation potential of 2.8V (compare to NHE). Since it is not stable, it will rapidly attack any pollutant at the surface or in solution near the surface as well. After several steps, the pollutant can be mineralized into carbon dioxide, carbon oxide, water, etc. The nature of the radical production also depends on the exact reaction condition, such as with oxygen or without oxygen [26]. However, in terms of catalyst, TiO_2 is the most popular one for the above degradation reaction.

1.3.2 Platinum modified TiO_2

In order to improve the described surface electrochemical reaction and the photocatalytic efficiency of TiO_2, some proper co-catalysts are usually deposited on the surface of the semiconductor catalysts to serve as reaction site and thus further improve the catalysis reaction [27]. As mentioned above, the photogenerated electrons and holes are likely (and unwanted) to recombine if there are no suitable active sites available on the surface. Therefore, it is important to provide suitable co-catalysts to accelerate the relative slow surface reactions, which happen on time scales of order of 10^{-8}s – 10^{-3}s. These reactions compete with the fast recombination process of electrons and holes (on the order of 10^{-9}s) [28]. Until now, many efforts have been made for the described modification [29-31]. Some of them try to functionalize the TiO_2 surface with other semiconductors having different band levels and hence to alter the charge transfer properties [32,33]. There is also plenty of literature [34,35] in which the authors try to sensitize TiO_2 with colored organic or inorganic compounds to extend its optical adsorption into the visible-light region (wavelength = 400 to 700nm). Nonmetallic elements and metal ion doping have been primarily used to extend the photon adsorption edge from the UV light spectrum to the visible light region. Doping, which is a bulk modification, can also make the photocatalyst a good adsorber in the visible spectrum, because of the light induced excitation of electrons from the dopant levels into the

conduction band of the TiO_2. The mostly used dopant element is including metal ion doping (Fe, Ni, Cu, etc.) [36-39], nonmetallic element doping (N, S, etc.) [40-43]. However, a dopant can also act as a recombination center for electrons and holes, which will decrease then photocatalytic efficiency. Not only the nature of the dopant but also the doping concentration need to be adapted and optimized for the specific application [44].

My work in this thesis was focused on surface modified Pt-loaded TiO_2 nanoparticles, since surface metal loading method is relative simple as compared to other modification methods, such as doping. The photocatalytic property of a TiO_2 nanoparticle is more active than TiO_2 bulk powder because of its significant large surface area to volume ratio, which leads to a high chemical activity. After loading with Pt, TiO_2 exhibits a better photocatalytic activity, because the Pt nanoparticle enhances the efficiency of photogenerated electron-hole separation [45].

Platinum is a frequently used metal for surface modification of TiO_2, because it has the highest working function and the smallest H_2 evolution potential as compared to other already tested metals. Such surface loaded Pt nanoparticles are also called co-catalysts, and it acts as electrons acceptor and reduction center for water molecules [46]. Under ultraviolet light illumination, photogenerated electrons prefer to transfer from the TiO_2 surface to the loaded Pt nanoparticles because the work function of Pt is lower than the conduction band level of TiO_2, and holes are left in TiO_2. Thus, the recombination of electrons and holes will be suppressed and lifetime of charge carriers will be prolonged.

$$Pt - TiO_2 + hv \rightarrow h_{VB}^{+} + e_{CB}^{-} \tag{1.7}$$

$$Pt + e_{CB}^{-} \rightarrow Pt^{-} \tag{1.8}$$

Trasatti has tested many metals in this context and found a volcano shaped relationship between the M-H strength (M present transition metal and H is hydrogen atom) and the exchange current for H_2 production [47]. Pt is on the peak of the volcano shape, this means it requires the lowest activation energy to produce hydrogen gas. This is why Pt is considered to be the most suitable cocatalyst for H_2 evolution. In the water splitting reaction, the proton is reduced by the electrons located on Pt the co-catalysts.

$$2H^{+}(ad) + Pt^{-} \rightarrow H_2(g) \tag{1.9}$$

Another advantage of loading Pt nanoparticles is that the contact interface of Pt and TiO_2 forms a Schottky barrier [48], which can facilitate charge separation. This Schottky barrier causes an increase of the in built-in potential and narrows the width of the depletion region, which leads to an efficient electron-hole separation [49].

However, when the amount of the co-catalysts exceeds its optimum value, the space charge layer becomes so narrow that the penetration depth of light exceeds the depletion region, and charge carrier recombination becomes more favorable than charge separation, thereby decreasing the photocatalytic efficiency. Moreover, the administration of the metal on the TiO_2 surface is achieved by deprotonation of Ti-O-H and formation of Ti-O-M bonds (M is metal) [11]. This means that a larger percentage of metal on the surface causes a smaller amount of surface hydroxyl groups, and as a result, the photoactivity will be reduced. Moreover, the loaded metal acts as a recombination center as well as an electron trapping site at the same time. On the other hand, the color of TiO_2 will become more grey when the amount of loaded metal increases. The grey color could reduce the photon flux toward the TiO_2 and in turn lead to less excited electrons in the conduction band.

1.3.3 Adsorption of water molecule

Under air, the surface of TiO_2 is covered with several layers of water molecules, and the TiO_2 surface is covered with three water layers [50] containing distinct water species: (1) the innermost layer with highly immobilized water, (2) the intermediate layer consisting of relatively mobile water, and (3) the outermost layer with mobilized water under the chemical exchange with water vapor.

As a result, a built-in electric field is formed at the interface. Water molecules in the air can be adsorbed on the surface of TiO_2, and then dissociate to generate a –OH surface termination [51]. These acquired –OH terminations can be treated as electronic surface states which are located within the bandgap of TiO_2. Since the energy level of these surface states are lower than the lowest level of the conduction band, electrons in the conduction band will be trapped into these surface states. The trapping of electrons in turn leads to a space charge layer with a width of a few nanometers below the interface, and the surface shows negative charge. To preserve electrical neutrality, a layer of positive charge will be formed within the TiO_2. These space charges lead to build-in electric fields and an upward bending of the bands at the surface [52]. However, the adsorbed water can be regarded as an effective recombination center for electrons and holes [53]. We know that the efficiency of photoelectrochemical processes depends on the competition between the desired reaction and a loss of photogenerated carriers by electron-hole recombinations. The recombination can not only take place in the bulk of a semiconductor, but also via surface states [52]. This surface recombination is particular important for

nanostructured semiconductor electrodes because nanoparticles have very large surface to volume ratios.

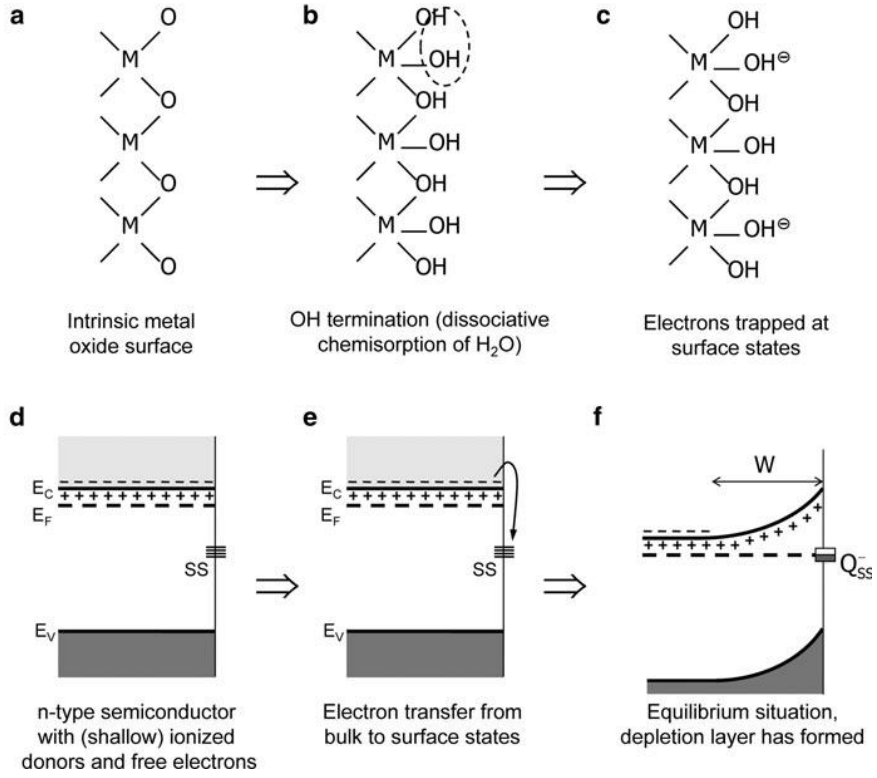

Fig. 1.11 Simplified illustration of the formation of a space charge region (SCR) at a metal oxide semiconductor surface when exposed to (humid) air [52].

Even in vacuum, a build-in electric field will be formed because TiO_2 inevitably has a lot of surface defects – oxygen vacancies (O_v), which also behave as electronic surface states that are able to trap electrons.

1.3.4 Sacrifice material – methanol

In the water splitting reaction, the formation rate of hydrogen and oxygen gas is very low because of the fast recombination rate of photo-induced holes and electrons, and also because the driving force for the backward reaction ($H_2 + O_2 = H_2O$) is very large [54]. In order to enhance the formation rate for hydrogen gas, sacrificing reagents are usually used in water splitting systems, for example, methanol (CH_3OH), ethanol (CH_3CH_2OH), and ethylenediaminetetraacetic acid (EDTA) and so on. Methanol is called a hole scavenger as it reacts irreversibly with the photo-induced holes at the surface of TiO_2. Therefore, it can prevent the electron-hole recombination and prolong the life time of electrons. Moreover, the radicals ($\cdot CH_2OH$) produced by the hole trapping are themselves good electron donors, so it can inject electrons to the conduction band of TiO_2 and this way increase the potential for the evolution

of hydrogen gas [55]. As a result, it leads to a double yield of hydrogen gas. This phenomenon is called “double effect”. As a hydrogen containing sacrificing reagent, it is believed that methanol could also contribute its hydrogen atoms to produce hydrogen gas.

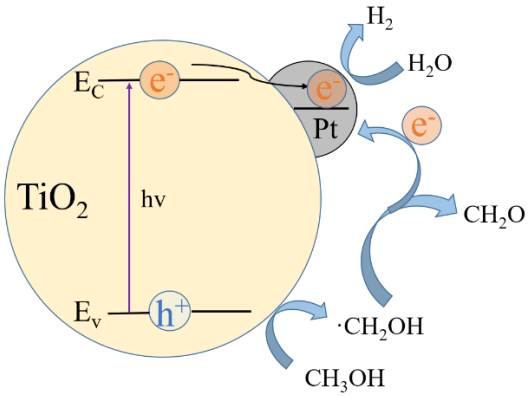

Fig. 1.12 Schematic illustration of electron and hole transfer in water splitting reaction with methanol as sacrifice material on catalyst Pt loaded TiO_2.

1.4 Reference:

[1] "The Copenhagen diagnosis: updating the world on the latest climate science," *Choice Rev. Online*, 2012.

[2] J. Oppenheim and E. D. beinhocker, "Climate change and the economy - Myths versus Realities," *Davos, Switzerland. McKinsey & Company*, Inc. 2009.

[3] D. Saygin, R. Kempener, N. Wagner, M. Ayuso, and D. Gielen, "The Implications for renewable energy innovation of doubling the share of renewables in the global energy mix between 2010 and 2030," *Energies*, 2015.

[4] World Energy Council, "About the World Energy Council About Issues Monitor." pp. 50–52, 2019.

[5] I. Papagiannis, E. Doukas, A. Kalarakis, G. Avgouropoulos, and P. Lianos, "Photoelectrocatalytic H_2 and H_2O_2 production using visible-light-absorbing photoanodes," *Catalysts*, 2019.

[6] G. Zini and P. Tartarini, "Solar hydrogen energy systems: science and technology for the hydrogen economy". *Springer Science & Business Media*, 2012.

[7] A. Ursúa, L. M. Gandía, and P. Sanchis, "Hydrogen production from water electrolysis: Current status and future trends," IEEE, 2012.

[8] A. Kudo and Y. Miseki, "Heterogeneous photocatalyst materials for water splitting," *Chem. Soc. Rev.*, 2009.

[9] T. Hisatomi, J. Kubota, and K. Domen, "Recent advances in semiconductors for photocatalytic and photoelectrochemical water splitting," *Chem. Soc. Rev.*, 2014.

[10] M. Nic, J. Jirat, and B. Kosata, Compendium of Chemical Terminology, *Blackwell Scientific Publication*, Oxford, 2012.

[11] J. Schneider, D. Bahnemann, J. Ye, G. L. Puma, and D. D. Dionysiou, "Photocatalysis: fundamentals and perspectives". *Royal Society of Chemistry*, 2016, ISBN 978-1-78262-041-9

[12] A. Fujishima and K. Honda, "Electrochemical photolysis of water at a semiconductor electrode," *Nature*, 1972.

[13] Y. Nosaka and A. Nosaka, "Introduction to Photocatalysis: From Basic Science to Applications". *Royal Society of Chemistry, 2019*. ISBN 978-1-78262-320-5

[14] F. Zhang et al., "Recent advances and applications of semiconductor photocatalytic technology," *Applied Sciences (Switzerland)*. 2019.

[15] "Introduction to Solar Radiation". *www.newport.com*. Archived from the original on 29 October 2013.

[16] K. Biernat, A. Malinowski, and M. Gnat, "The possibility of future biofuels production using waste carbon dioxide and solar energy," in *Efficiency and Sustainability in Biofuel Production: Environmental and Land-Use Research, 2015.*

[17] *D. Dambo*urnet, I. Belharouak, and K. Amine, "Tailored preparation methods of TiO_2 anatase, rutile, brookite: Mechanism of formation and electrochemical properties," *Chem. Mater.,* 2010.

[18] R. Asahi, Y. Taga, and W. Mannstadt, "Electronic and optical properties of anatase," *Physical Review B - Condensed Matter and Materials Physics,* 2000.

[19] R. Bertani, "Solids and surfaces. A chemist's view of bonding in extended structures.," *Inorganica Chim. Acta,* 1990.

[20] A. G. Tamirat, J. Rick, A. A. Dubale, W.-N. Su, and B.-J. Hwang, "Using hematite for photoelectrochemical water splitting: a review of current progress and challenges," *Nanoscale Horizons,* 2016.

[21] Y. Nakaoka and Y. Nosaka, "ESR Investigation into the effects of heat treatment and crystal structure on radicals produced over irradiated TiO_2 powder," *J. Photochem. Photobiol. A Chem.,* 1997.

[22] J. Zhang and Y. Nosaka, "Mechanism of the OH radical generation in photocatalysis with TiO_2 of different crystalline types," *J. Phys. Chem. C,* 2014.

[23] A. Yamakata, T. A. Ishibashi, and H. Onishi, "Water- and oxygen-induced decay kinetics of photogenerated electrons in TiO_2 and Pt/TiO_2: A time-resolved infrared absorption study," *J. Phys. Chem. B,* 2001.

[24] D.W. Bahnemann, M. Hilgendorff, R. Memming, "Charge carrier dynamics at TiO_2 particles: reactivity of free and trapped holes," J. Phys. Chem. B. 101 (1997) 4265–4275.

[25] J. Montoya, M. Atitar, F., D.W. Bahnemann, J. and Peral, P. Salvador, "Comprehensive Kinetic and Mechanistic Analysis of TiO_2 Photocatalytic Reactions According to the Direct-Indirect (DI) Model: II) Experimental Validation," *J. Phys. Chem. C.,* 2014.

[26] M. Hartmann, S. Kullmann, and H. Keller, "Wastewater treatment with heterogeneous Fenton-type catalysts based on porous materials," *J. Mater. Chem.,* 2010.

[27] J. Wen, X. Li, W. Liu, Y. Fang, J. Xie, and Y. Xu, "Photocatalysis fundamentals and surface modification of TiO_2 nanomaterials," *Cuihua Xuebao/Chinese Journal of Catalysis*., 2015.

[28] W. Fan, Q. Zhang, and Y. Wang, "Semiconductor-based nanocomposites for photocatalytic H2 production and CO_2 conversion," Physical Chemistry Chemical Physics. 2013.

[29] X. You, F. Chen, J. Zhang, and M. Anpo, "A novel deposition precipitation method for preparation of Ag-loaded titanium dioxide," *Catal. Letters,* 2005.

[30] C. H. Li, Y. H. Hsieh, W. T. Chiu, C. C. Liu, and C. L. Kao, "Study on preparation and

photocatalytic performance of Ag/TiO_2 and Pt/TiO_2 photocatalysts," *Sep. Purif. Technol.*, 2007.

[31] A. M. Ruiz, G. Dezanneau, J. Arbiol, A. Cornet, and J. R. Morante, "Insights into the Structural and Chemical Modifications of Nb Additive on TiO_2 Nanoparticles," *Chem. Mater.*, 2004.

[32] J. Zhao et al., "Enhancement of solar hydrogen evolution from water by surface modification with CdS and TiO_2 on porous $CuInS_2$ photocathodes prepared by an electrodeposition-sulfurization method," *Angew. Chemie-Int. Ed.*, 2014.

[33] M. A. Habib, M. T. Shahadat, N. M. Bahadur, I. M. I. Ismail, and A. J. Mahmood, "Synthesis and characterization of ZnO-TiO_2 nanocomposites and their application as photocatalysts," *Int. Nano Lett.*, 2013.

[34] T. Umebayashi, T. Yamaki, S. Tanaka, and K. Asai, "Visible light-induced degradation of methylene blue on S-doped TiO_2," *Chem. Lett.*, 2003.

[35] W. Wang, D. Yang, W. Yang, J. Sun, and H. Hou, "Efficient visible-light driven photocatalysts: coupling TiO_2(AB) nanotubes with g-C_3N_4 nanoflakes," *J. Mater. Sci. Mater. Electron.*, 2017.

[36] A. Di Paola et al., "Preparation of polycrystalline TiO_2 photocatalysts impregnated with various transition metal ions: Characterization and photocatalytic activity for the degradation of 4-nitrophenol," *J. Phys. Chem. B*, 2002.

[37] T. Ohno, Z. Miyamoto, K. Nishijima, H. Kanemitsu, and F. Xueyuan, "Sensitization of photocatalytic activity of S- or N-doped TiO_2 particles by adsorbing Fe^{3+} cations," *Appl. Catal. A Gen.*, 2006.

[38] D. Jing, Y. Zhang, and L. Guo, "Study on the synthesis of Ni doped mesoporous TiO_2 and its photocatalytic activity for hydrogen evolution in aqueous methanol solution," *Chem. Phys. Lett.*, 2005.

[39] S. Xu and D. D. Sun, "Significant improvement of photocatalytic hydrogen generation rate over TiO_2 with deposited CuO," Int. J. Hydrogen Energy, 2009.

[40] S. Sato, "Photocatalytic activity of NOx-doped TiO_2 in the visible light region," *Chem. Phys. Lett.*, 1986.

[41] R. Asahi, T. Morikawa, T. Ohwaki, K. Aoki, and Y. Taga, "Visible-light photocatalysis in nitrogen-doped titanium oxides," *Science.*, 2001.

[42] H. Irie, Y. Watanabe, and K. Hashimoto, "Nitrogen-concentration dependence on photocatalytic activity of TiO_2-xNx powders," *J. Phys. Chem. B*, 2003.

[43] T. Ohno, M. Akiyoshi, T. Umebayashi, K. Asai, T. Mitsui, and M. Matsumura, "Preparation of S-doped TiO_2 photocatalysts and their photocatalytic activities under visible light," *Appl. Catal. A Gen.*, 2004.

[44] W. Shao, H. Wang, and X. Zhang, "Elemental doping for optimizing photocatalysis in

semiconductors," *Dalt. Trans.*, 2018.

[45] Y. Wang *et al.*, "The preparation, characterization, photoelectrochemical and photocatalytic properties of lanthanide metal-ion-doped TiO_2 nanoparticles," *J. Mol. Catal. A Chem.*, 2000.

[46] J. Yang, D. Wang, H. Han, and C. Li, "Roles of cocatalysts in photocatalysis and photoelectrocatalysis," *Acc. Chem. Res.*, 2013.

[47] S. Trasatti, "Work function, electronegativity, and electrochemical behaviour of metals. III. Electrolytic hydrogen evolution in acid solutions," *J. Electroanal. Chem.*, 1972.

[48] G. A. Hope, A. J. Bard, and A. J. Bard', "Platinum/titanium dioxide (rutile) interface. Formation of ohmic and rectifying junctions More About This Article Piatinum/Titanium Dioxide (Rutile) Interface. Formation of Ohmic and Rectifying Junctions," *J. Phys. Chem*, 1983.

[49] A. W. Xu, Y. Gao, and H. Q. Liu, "The preparation, characterization, and their photocatalytic activities of rare-earth-doped TiO_2 nanoparticles," *J. Catal.*, 2002.

[50] C. Y. Wu, K. J. Tu, J. P. Deng, Y. S. Lo, and C. H. Wu, "Markedly enhanced surface hydroxyl groups of TiO_2 nanoparticles with Superior water-dispersibility for photocatalysis," *Materials (Basel).*, 2017.

[51] R. Van de Krol and M. Grätzel, "Photoelectrochemical hydrogen production Electronic materials: science & technology. *New York: Springer*; 2010." p. 321, 2012.

[52] M. Grätzel, "photoelectrochemical hydrogen production" *Springer*, 2012, ISBN 978-1-4614-1379-0

[53] A. L. Linsebigler, G. Lu, and J. T. Yates, "Photocatalysis on TiO_2 Surfaces: Principles, Mechanisms, and Selected Results," *Chem. Rev.*, 1995.

[54] M. Ni, M. K. H. Leung, D. Y. C. Leung, and K. Sumathy, "A review and recent developments in photocatalytic water-splitting using TiO_2 for hydrogen production," *Renewable and Sustainable Energy Reviews*. 2007.

[55] F. Guzman, S. S. C. Chuang, and C. Yang, "Role of methanol sacrificing reagent in the photocatalytic evolution of hydrogen," *Ind. Eng. Chem. Res.*, 2013.

Chapter 2
Electrochemistry

In this chapter, I will lay out the fundamentals to understand the basics of electrochemistry. Then, two kinds of interfaces will be in illustrated in detail: One is the interface between a metal and a liquid electrolyte, and the other one is the interface between a semiconductor (metal oxide) and a liquid electrolyte. Subsequently, the main structure of an electrochemical setup and its function will be described. At the end, we introduce the method of cyclic voltammetry since it is the most important examination method in my experiments.

2.1 Electrochemical potential

First, we start with the chemical potential. The chemical potential represents, how difficult it is to add a chemical species into a phase (α), or to remove a chemical species out of a phase (α) under the condition of constant pressure and temperature. The value of the chemical potential can be calculated by differentiation of Gibbs free energy (G) with respect to the amount of chemical species (n) [1].

$$\mu_i^{\alpha} = (\frac{\partial G}{\partial n_i})_{T,P,n_{i\neq j}} \tag{2.1}$$

For a solution in liquid phase, the chemical potential of an ion relates to its activity a_i [2], which is the effective concentration of the ion. We know that the movement of ion is not totally free in real solution due to the interaction between positive and negative ions, so the concentration of an ion (c_i) should be replaced by the activity of an ion (a_i) [3]. In very dilute solution, $c_i \approx a_i$.

$$\mu_i = \mu_i^0 + RTln(\frac{a_i}{a_i^0}) \tag{2.2}$$

μ_i^0 is the standard chemical potential, R is universal gas constant, T is temperature, a_i is activity of the ion and $a_i^0 = 1$.

For a charged species in solution, such as ions and electrons, additional energy is required to bring a charge to this chemical species. Therefore, the electrochemical potential has to be replaced by the chemical potential describing the charged species [4].

$$\mu_i' = \mu_i + z_i F\emptyset \tag{2.3}$$

Here z_i is electron number, F is the Faraday constant and $\emptyset$ is the potential in Volt. Under equilibrium conditions, the chemical potential must be constant everywhere, even in different phases.

When a redox reaction takes place, electrons will transfer from one chemical species to another chemical species.

$$Red \leftrightarrow Ox + e^- \tag{2.4}$$

Here, *Red* denotes the reduced reagent and *Ox* is the oxidized reagent. After reaching equilibrium condition,

$$\mu_{red} = \mu_{ox} + \mu_{e,redox} \tag{2.5}$$

$$\mu_{e,redox} = \mu_{red} - \mu_{ox} = \mu_{red}^0 - \mu_{ox}^0 - RTln\left(\frac{a_{ox}}{a_{red}}\right) = \mu_{e,redox}^0 - RTln\left(\frac{a_{ox}}{a_{red}}\right) \tag{2.6}$$

where μ_e is the electrochemical potential of the electrons, and μ_e^0 is the standard electrochemical potential . The electrochemical potential is in units of Joule·mol^{-1}, It can be transcribed into unit Volt be equation (2.7)

$$E_{redox} = \frac{\mu_{e,redox}}{F} \tag{2.7}$$

Here, U_{redox} is redox potential for a half electrochemical reaction and U_{redox}^0 is the standard redox potential. It describes the potential required to drive a redox potential under standard conditions (temperature T=0^{o}C, pressure p=101kPa and the activity of reduced and oxidized reagent equal to 1), so the equation (6) can be written as

$$E_{redox} = E_{redox}^0 - \frac{RT}{zF}\ln(\frac{a_{ox}}{a_{red}}) \tag{2.8}$$

According to equation (2.8), we know that the redox potential not only depends on the activity of reductant and oxidant, but also rely on the pressure and temperature of the redox system. In my lab, the variation of the pressure and temperature is very small, so the impact of these factors can be neglected.

Since the chemical potential in metals or semiconductors is also called Fermi level, the electrochemical potential $\mu_{e,redox}$ is equivalent to the Fermi level of a redox system which is first introduced by Gerischer [5]. The Fermi level in redox systems can be considered as the highest energy level being occupied by electrons, and the difference is that the Fermi level in redox systems can be adjusted by changing the concentration of reduced reagent and oxidized reagent. The redox potential represents the potential required to drive an oxidation or reduction reaction. The more positive the redox potential is, the stronger the reductant's affinity for

electrons is, and it is more likely to be reduced; Vice versa, the more negative the redox potential is, the weaker the reductant's affinity for electrons is, and it is more likely to be oxidized.

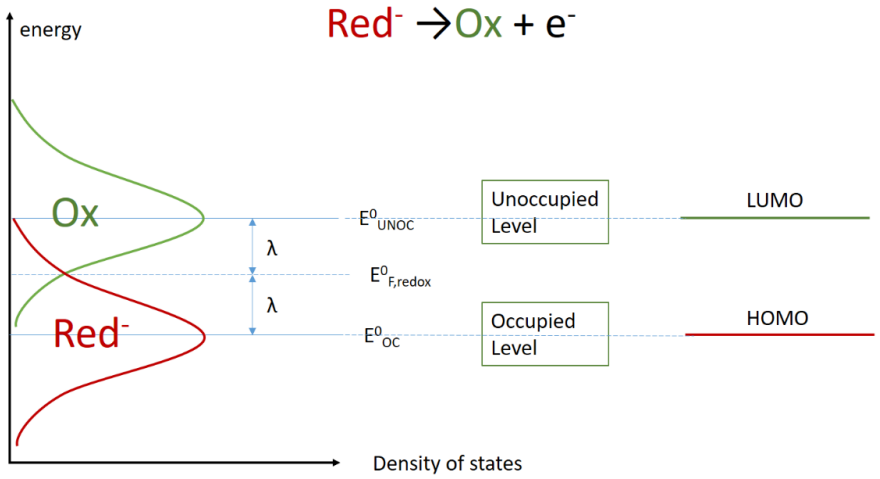

Fig. 2.1 Gerischer model for the energy of redox system.

For an electrochemical reaction, almost all the important reaction steps take place at the interface between the solid electrode and a liquid electrolyte, so the chemical potentials of solid/liquid interface are particularly interesting. When an electrode begins to make contact to an electrolyte and when the Fermi energy of metal is not identical with the redox potential of the electrolyte, electron transfer across the metal/electrolyte interface will take place. If the Fermi energy of the metal electrode is higher than the redox potential, electrons will transfer from the electrode to the electrolyte to elevate the redox potential of the electrolyte until it reaches the same level of the Fermi energy of the metal. Vice versa, if the Fermi energy of the metal is lower than the redox potential of the electrolyte, electrons will transfer from the electrolyte to the metal to lower the redox potential. During the electron transfer process, redox reactions are forced to take place at the interface. After the Fermi level and redox potential align with each other, the forward- and backward reaction rates are equal and the system is in dynamic equilibrium. In order to drive the forward reaction or the backward reaction, a potential cell is used to raise or lower the Fermi level of the metal by applying an electric potential to it. The working mechanism of the potential cell will be discussed later.

2.2 Electrochemical electrode

2.2.1 Standard hydrogen

The standard redox potential in electrochemistry is a relative value, where the reference is the redox potential of the standard hydrogen electrode (SHE) consisting of a platinum electrode in

contact with a proton solution and hydrogen gas [6]. The activity of the proton solution is 1 and the hydrogen gas is saturated in the proton solution at standard pressure. For SHE, the electrochemical half reaction $H_2 = 2H^+ + 2e^-$ takes place on a platinum electrode, and the redoxpotential of it is defined as to be zero [7]; for the other electrochemistry half reactions, their standard redox potential is the relative value compared to the redox potential of SHE.

As introduced before, the redox potential for a half reaction is the electrochemical potential of an electron in this half reaction, and the reference is the electrochemical potential of the electron in the SHE half reaction. In metal and semiconductor physics, the so called vacuum level is taken as the reference value, and in order to connect the knowledge of semiconductor physics and electrochemistry, their reference level can be linked by following expression [8]:

$$E_{vac} = -4.5eV - eE_{redox} \tag{2.9}$$

E_{vac} is the energy with respect to the above vacuum level in eV, E_{redox} is the potential versus the SHE in electrochemistry in Volt, and e is the elementary electronic charge.

When some half reaction takes place in an acid solution and a proton was involved in the reaction, for the purpose of convenient calculation, we can adjust the redox potential of the standard reference half reaction $H_2 = 2H^+ + 2e^-$ according to the concentration of protons. Since the pH value represents the concentration of protons, the reverse hydrogen electrode (RHE) is used here to include the pH dependent redox potential of reference [2], so

$$E_{RHE} = E_{SHE} + 0.059pH \tag{2.10}$$

The electrolyte employed in my experiments is 0.1mol·L^{-1} H_2SO_4 solution, so the pH value of the solution is pH=1, consequently $E_{RHE} = E_{SHE} + 0.059pH = 0.059V$.

2.2.2 Ag/AgCl reference

The advantage of a standard hydrogen electrode is its quickly establishing and reproducible redox potential. On the other hand, the disadvantage of SHE is its weak stiffness. The proton activity of the solution must be well defined because a(H^+) can influence the redox potential of SHE, and the solution should be oxygen free. Moreover, the platinum wire should also be renewed frequently because it easily adsorbs diluted species on it [7]. As a result, another commonly-used reference electrode is chosen to be used in my experiment, namely a silver/silver chloride electrode, which is often used as reference in reduction potential measurements. The reference electrode functions as a redox electrode, and the potential of it

is decided by the equilibrium between a silver wire and its surrounding silver chloride layer in 3 mol·L^{-1} KCl solution. The corresponding half reaction can be presented simply as following [7]:

$$AgCl \leftrightarrow Ag^{+} + Cl^{-} \tag{2.11}$$

The Nernst equation [9] shows that the redox potential depends on the activity of chloride ions, $E_{Agcl/Ag} = E^{0}_{Agcl/Ag} - \frac{RT}{zF}\ln \alpha(cl^{-})$. The activity of Cl^{-1} is 3 mol·L^{-1}, so the calculated redox potential of the silver/silver chloride electrode is 0.205V Vs RHE, where RHE=0.0059V.

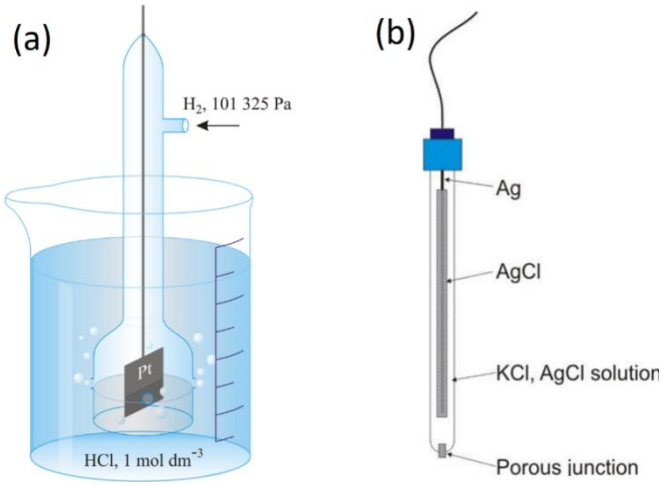

Fig. 2.2 structure of reference electrode: (a) standard hydrogen electrode [10], and (b) silver/silver chloride electrode. (source: https://www.corrosion-doctors.org/Corrosion-Thermodynamics/Reference-Half-Cells-Silver.htm, Aug. 01.2020)

2.2.3 Metal working electrode

As already mentioned before, when a metal electrode and liquid electrolyte are brought into contact, electrons will transfer between the interface of the metal and the solution to align their Fermi levels. During the process, the non-grounded electrode will be charged, so it will attract ions which have opposite charges in the electrolyte solution due to electrostatic attraction. Consequently, these ions accumulate and orient near the interface in the solution, and these counter charges in the metal and the electrolyte start forming a double layer which behaves like capacitor [11]. For example, when a metal which has a high Fermi energy contacts with a solution which has a low Fermi energy, electrons will transfer from the metal to the solution, and the metal electrode will be consequently positive charged. Because there are abundant electrons and their mobility is very high in the metal, no space charge region will be created in the metal phase. At the same time, equivalent negative ions in the electrolyte are attracted to the interface as it is shown in Fig. 2.3 (a). The positive charges in the metal and the equivalent negative charges in the solution form the electrical double layer and this is described by the

Helmholtz model [12]. Due to Brownian motion, these attracted ions are not immobilized and thus are causing a diffuse layer, whose thickness depends on the ionic activity in the electrolyte, and this is described by the Gouy–Chapman model [13]. In the more advanced Stern model [14], the solution part of double layer actually consists of two layers, the "inner Helmholtz layer" and the "outer Helmholtz layer". The inner Helmholtz layer is close to the electrode at a distance of a few Angstroms, it is formed by specially adsorbed ions and some solvent molecules. The formation of the outer Helmholtz layer is also at a few Angstroms distance and it is due to the electrostatic force between positive charged electrode and negative ions in solution. These ions are also called "non-specifically adsorbed ions". In the famous Stern model, a fixed Helmholtz layer and an additional diffusing layer was combined [14]. Because all the ions in the solution are surrounded by some water molecules, this solvation cloud prevents them from approaching the electrode surface closer than a few Angstroms.

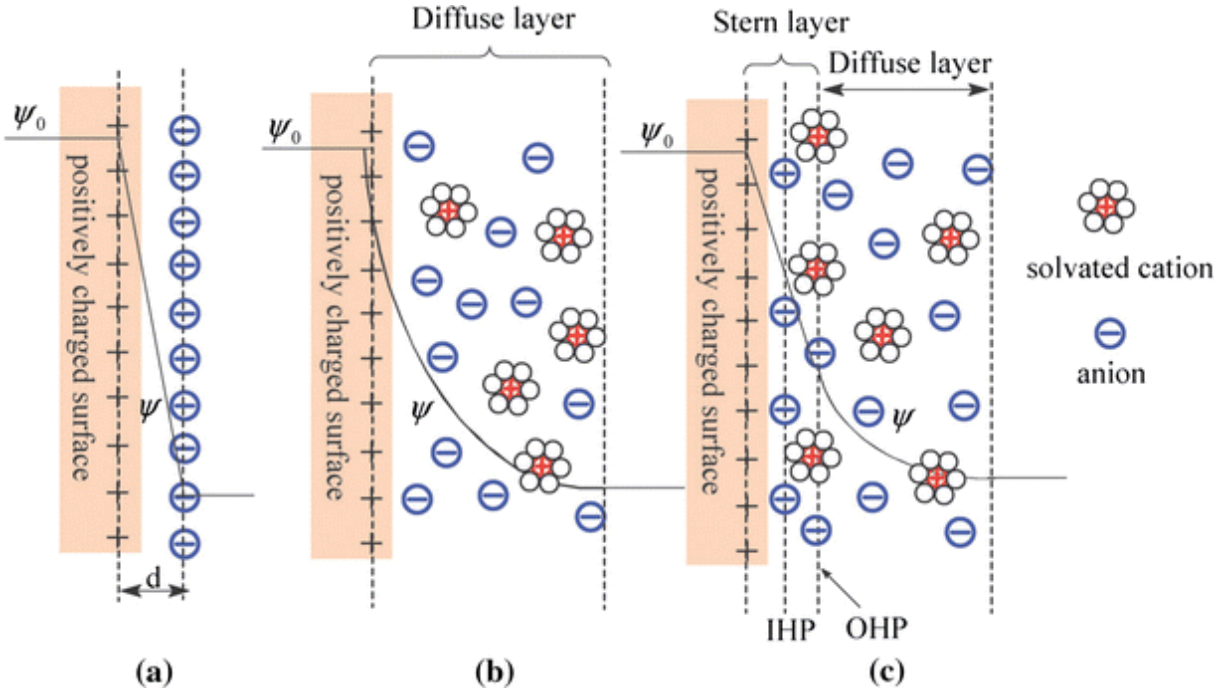

Fig. 2.3 Schematic Models of the electrical double layer at a positively charged surface: (a) the Helmholtz model, (b) the Gouy–Chapman model, and (c) the Stern model [15].

2.2.4 Semiconductor working electrode

If a semiconductor electrode and an electrolyte solution are brought into contact, the Fermi level of the semiconductor and the electrochemical potential of the solution will also align each other by transferring electrons at the interface. After alignment, the semiconductor electrode will be also charged, and in contrast to the metal electrode, these additional charges cause a band bending of the conduction band and the valence band close to the interface. This is

because the semiconductor has a much smaller charge carrier density and a lower charge carrier mobility. The counter charge will distribute over a certain distance below the interface, which is called space charge layer. When the Fermi energy of the SC is higher than the electrochemical potential of the electrolyte, electrons transfer from the SC to the solution. In turn, a quite large number of positive charges accumulate near the interface, the bands of SC bend upwards and create said depletion layer. Vice versa, when the Fermi energy of the SC is lower than the electrochemical potential of the electrolyte, electrons transfer from the solution to the SC, resulting in many negative charges to accumulate near the interface, a downward bend bending of the SC and the creation of an accumulation layer. When the difference between Fermi energy of the SC and the electrochemical potential of the electrolyte is very large, the band bending will become so strong that an inversion layer is created. The charge density on a logarithmatic scale at the depletion layer, accumulation layer and inversion layer and the caused band bending at these layer are depicted in Fig. 2.4. When the conduction band and the valence band bend upwards, holes accumulate in front of the depletion layer and electrons diffuse toward the bulk of the SC; When the conduction band and valence band bend downwards, electrons accumulate at the depletion layer and holes diffuse toward the bulk of SC.

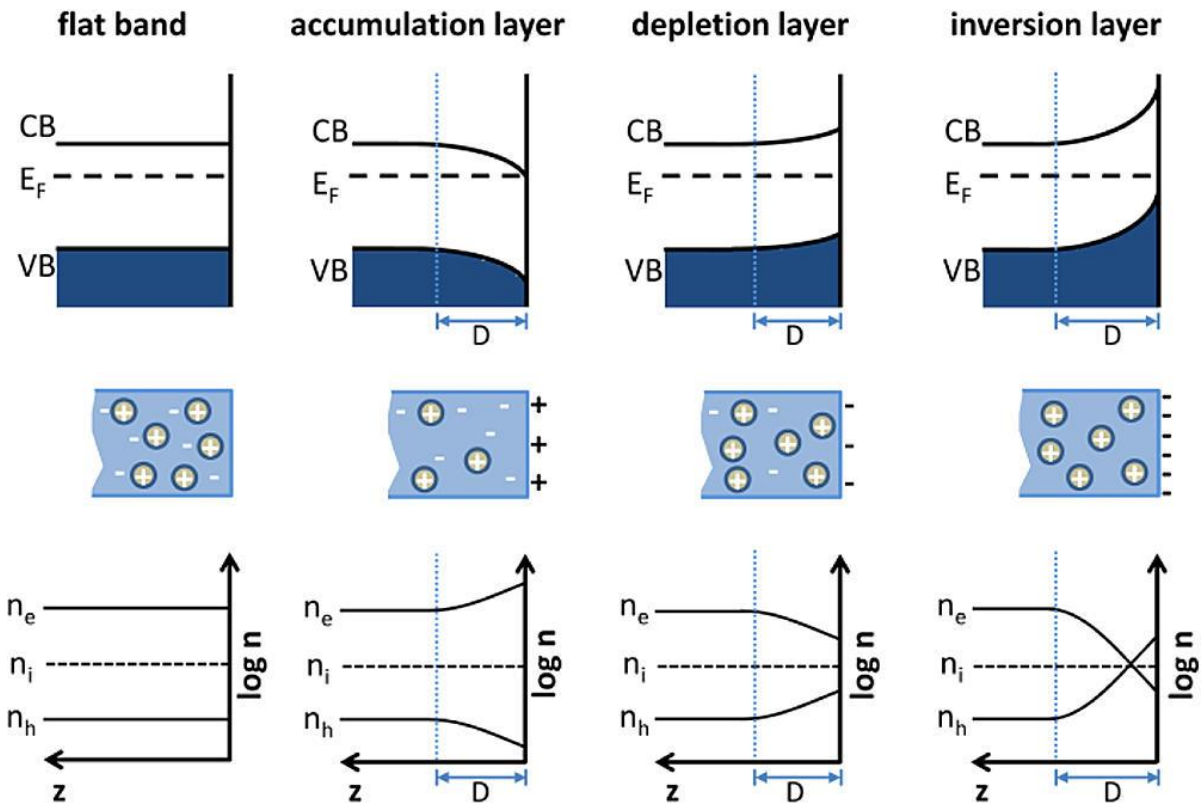

Fig. 2.4. Schematic diagrams of band energy level of n-type semiconductor and its free charge carrier densities (on logarithmic scale) from the surface to the bulk. D is the thickness of space charge region. n_e is free electron

density, n_h is free hole density, and ni is intrinsic carrier density. CB represent the conduction band, VB represent the valence band and EF is the Fermi level of the semiconductor [16].

As described in chapter one, water can be adsorbed on the surface of TiO_2 and generate a surface termination, which can be treated as surface states. These surface states lead to a built-in electric field and upward band bending at the TiO_2 surface.

When a semiconductor is immersed in an aqueous solution, H^+ and OH^- ions in the electrolyte solution will continuously adsorb and desorb from the surface until equilibrium is established,

$$M - OH \overset{K_a}{\leftrightarrow} MO^- + H^+_{aq} \quad (2.12)$$

$$M - OH + H^+_{aq} \overset{K_b}{\leftrightarrow} M - OH^+_2 \quad (2.13)$$

Hence, the net total charge adsorbed at the surface depends on the pH of the solution and the Bronsted acidity [17] of the semiconductor surface. As a result, the charge of semiconductor surface can be positive, zero, or negative, because it consists of electrons (or holes) trapped in surface states plus the specifically adsorbed ions described in above reactions (2.12) and (2.13).

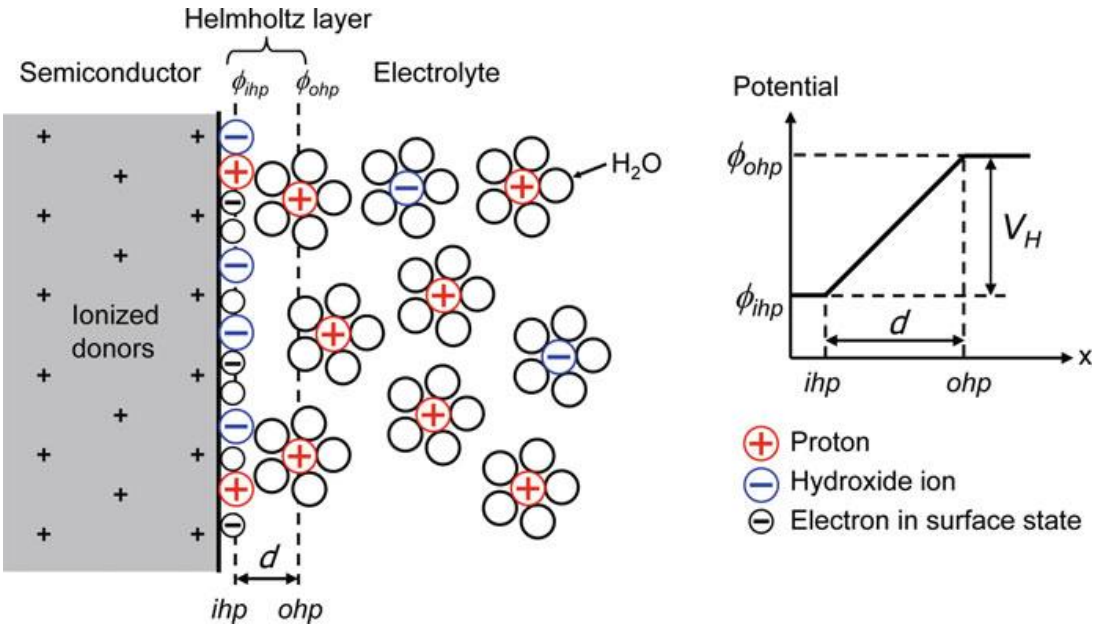

Fig. 2.5 Schematic model of the semiconductor/electrolyte interface and the Helmholtz layer. The inner Helmholtz plane (ihp) consists of specifically adsorbed H+ and OH- ions at the semiconductor surface; The distance of outer Helmholtz plane (ohp) determined from the closest approach for ions to the surface of electrode, which is only a few Angstroms [18].

Since the surface of the semiconductor electrode is charged, a double layer will also be formed in the solution. The total width of Helmholtz layer is around 2 to 5 Angstroms, and the dielectric constant of water which is around ε=6 on such a small scale [19]. The potential drop across this Helmholtz layer can be calculated by the following equation:

$$V_H = \delta d = \frac{Qsd}{\varepsilon_0 \varepsilon_r} \tag{2.14}$$

So the potential drop across the Helmholtz layer id typically around 0.1 to 0.5 V for a surface charge of Q_s = 1013cm^{-2}, and the Helmholtz capacitance is 10-20 μF·cm^{-2} [19]. Moreover, the depletion layer in TiO_2 and the Helmholtz layer act as two capacitors in series.

2.2.5 Current-voltage characteristic at the interface between metal electrode and liquid surface

When an extra potential is applied to a metal electrode, the Fermi energy of the metal becomes shifted against the electrochemical potential in the solution as illustrated in figure 2.6, and the equilibrium between electrode and electrolyte solution is disturbed. This causes an electron transfer at the interface. According to Gerischer model [20], the redox system provides empty electronic states (D_{ox}) and occupied electronic states (D_{red}). Upon negative polarization, the Fermi level of electrode becomes higher, and more electrons transfer from the occupied states in the metal into the empty states (D_{ox}) of the redox system. Vice versa, upon positive polarization, the Fermi energy of the metal becomes lower and more electrons transfer from the occupied states (D_{red}) of the redox system to the empty states in the metal electrode. The difference between the applied potential ($\emptyset$) and the equilibrium potential ($\emptyset_0$) is called "overpotential (E)", and $\eta = \emptyset - \emptyset_0$. First, a certain overpotential forces charge carriers to pass through the interface, and then the redox reaction is promoted in forward direction or in backward direction. Finally, mass flow will also increase because the amount of redox species is increased or reduced by the redox reaction.

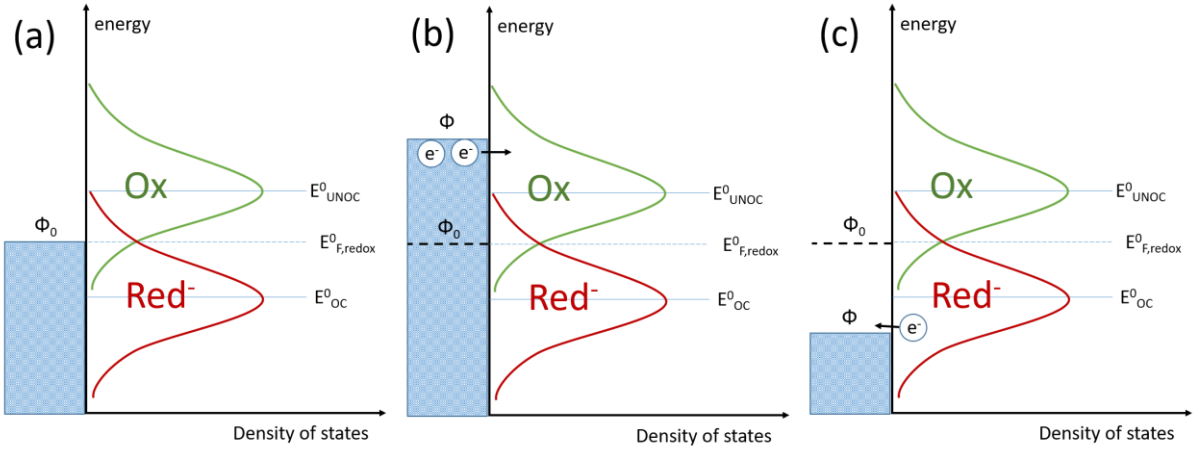

Fig. 2.6 Schematic energy diagrams and electrons transfer upon equilibrium condition (a), upon negative polarization (b) and upon positive polarization (c). when the Fermi energy of metal is aligned with electrochemical potential of solution, electrons transfer at the interface reach dynamic equilibrium; Upon negative polarization, the Fermi energy of metal shift higher than electrochemical potential of solution, and more electrons transfer from

metal to solution; Upon positive polarization, the Fermi energy of metal shift lower than electrochemical potential of the solution, and more electrons transfer from the solution to the metal electrode.

These kinetically controlled processes are called irreversible reactions, and the current density j is used to qualitatively describe amount of the transferring electrons. At the interface of the electrode, forward and backward electrochemical reactions occur simultaneously. The oxidation of the redox system produces an anodic current density j_a, and the reduction of redox system produces a cathodic current density j_c. j_a and j_c can be expressed by equation (2.15) and (2.16) [9].

$$j_a = e \cdot k^+ c_{red} \tag{2.15}$$

$$j_c = e \cdot k^- c_{ox} \tag{2.16}$$

c_{red} and c_{ox} are concentration of the reduced species and oxidized species; k^+ and k^- are rate constants. According to Marcus theory [21] and Nernst equation the rate constant k^+ and k^- relate to the overpotential η and electron transfer factor α.

$$k^+ = k_0^+ exp\left[\frac{(1-\alpha)\cdot e\cdot \eta}{k\cdot T}\right] \tag{2.17}$$

$$k^- = k_0^- exp\left[\frac{(-\alpha)\cdot e\cdot \eta}{k\cdot T}\right] \tag{2.18}$$

The overall current density which flow across the interface is called exchange current density j, and it is the summation of the anodic current density j_a and the cathodic current density j_c. Hence

$$j = j_a + j_c = j_0\left[exp\frac{(1-\alpha)\cdot e\cdot \eta}{k\cdot T} - \exp(-\frac{\alpha\cdot e\cdot \eta}{k\cdot T})\right] \tag{2.19}$$

here, e denotes the elementary electronic charge, k is the Boltzmann constant, and T is the temperature. The value of the electron transfer factor lies in a range between 0.4 to 0.6, being deduced from an empirical approach [9]. j0 is the exchange current at equilibrium (η=0). In equilibrium, the forward reaction and backward reaction are in balance and the value of the anodic current is equal to the cathodic current ($j_a = j_c$). Equation (2.19) is known as the Butler-Volmer relation in traditional electrochemistry. It is only valid when the diffusion of the redox species to the electrode interface is sufficiently fast. The curve of the anodic current density j_a, the cathodic current density j_c, and total current density are shown in the above picture of Fig. 2.7.

When the overpotential η is sufficient large, $\frac{e\cdot \eta}{k\cdot T} \gg 1$, one of the exponential terms in the Butler-Volmer equation can be neglected, and the current density can be expressed on logarithmatic scale:

$$lnj = lnj^+ = lnj_0 + \frac{(1-\alpha)\cdot e\cdot \eta}{k\cdot T} \tag{2.20}$$

Or $$lnj = lnj^{-} = lnj_0 - \frac{\alpha \cdot e \cdot \eta}{k \cdot T} \quad (2.21)$$

Equation (2.20) and (2.21) are called Tafel equations [22], and the below panel of figure 7 shows the relationship between the logarithms of the current density and the overpotential η. We can see that at higher overpotential, the value of lnj exhibits a linear dependence on the overpotential. The slope of the linear dependence is called Tafel slope, which equal to $\frac{(1-\alpha)\cdot e\cdot \eta}{k\cdot T}$ or $-\frac{\alpha\cdot e\cdot \eta}{k\cdot T}$. The point of intersection between the Tafel slope and the y axis is the exchange current j_0. The determination of the Tafel slope is a powerful tool for gaining information about the rate-limiting step of a reaction.

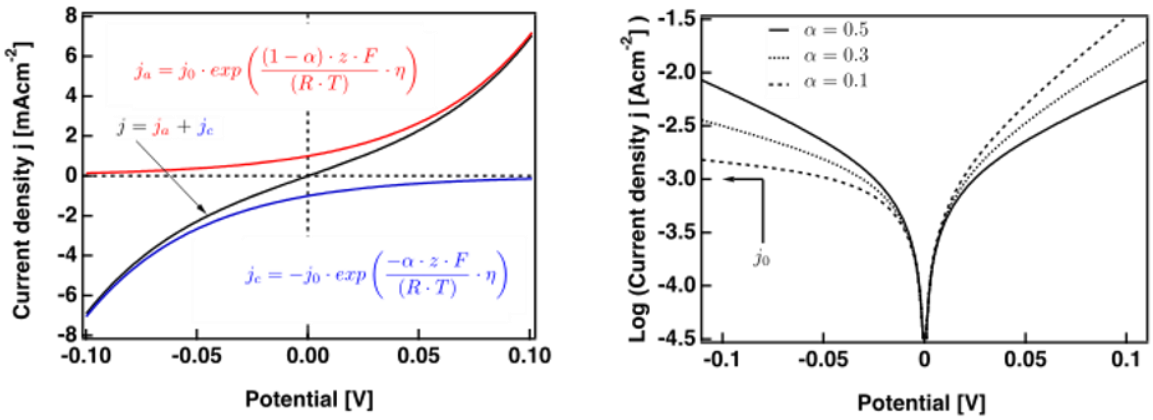

Fig. 2.7 The upper graph shows the current density as function of the overpotential η. The anodic and cathodic current densities are represented as j_a and j_c, respectively for $\alpha=\alpha_a=\alpha_c=0.5$ and j_0 =1mA·cm^{-2}. The lower graph shows the logarithm of the current density versus the overpotential η, also called Tafel plot, and they are ploted for different values of α. (source: https://en.wikipedia.org/wiki/Butler-Volmer_equation, Jun. 07, 2020)

2.2.6 Current-voltage characteristic at interface between semiconductor electrode and liquid phase

When a certain bias is applied to the working electrode, the potential difference will be distributed over the space charge layer and the Helmholtz layer. Since these layers act like two capacitors in series, both of them carry the same charge Q. The potential distribution is given by $\frac{\Delta V_{SC}}{\Delta V_H} = \frac{C_H}{C_{SC}}$, and any change of the applied bias will fall across the depletion layer of the semiconductor because of $C_H >> C_{SC}$ for low or moderately doped semiconductors. In this case, the sign of the band bending Φ_{SC} is decided by the applied voltage V_A and the flat band potential U_{fb}, it can be replaced by $U - U_{fb}$, where U is the applied potential ($U = eV_A$). In figure 2.8, the change of band bending according to the supplied voltage is illustrated. Any change of the applied potential drops across the space charge layer, whereas V_H remains constant. In the left

panel, a positive potential eV_A is applied to the semiconductor, so the band bending is significant; In the right panel, a negative potential $-eV_A$ is applied to the semiconductor, and its value is equal to flat band potential, so $\emptyset_{SC} = U - U_{fb} = 0$, there is not any band bending.

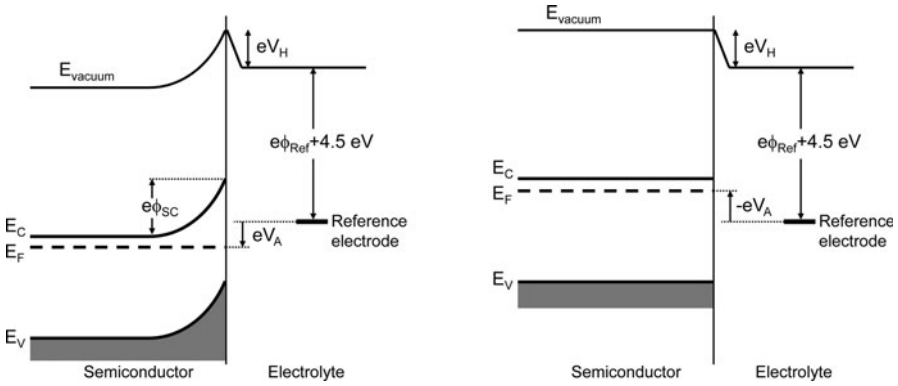

Fig. 2.8 Effect of applying a bias voltage (V_A) to an n-type semiconductor electrode. In the left picture, a positive potential is applied to the semiconductor, and in the right picture, the band bending reduce to zero when a sufficiently negative bias is applied. The reference electrode is SHE, and its potential is 4.5eV when take vacuum as the energy reference. [18]

The qualitative description of the current-potential relationship at a semiconductor electrode is different from that at a metal electrode. At the surface of a semiconductor, electrons transfer may arise between the electrolyte and the conduction band of the SC, or between the electrolyte species and the valence band of the SC. The situation is a little more complex, so the corresponding current depends on the position of the band energy and the occupation of the energy states in the band. For example, when a semiconductor electrode is immersed into H_2SO_4 solution without any redox system, under negative polarization, these electrons transfer from the semiconductor to the protons in the solution to reduce the proton and to form H_2. Under positive polarization, on the other hand, the electrode is dissolved. Such processes may even occur at some noble metal electrodes. The current -potential curves for n-type and p-type semiconductor electrodes are very different. For a n-type semiconductor electrode, the cathodic current caused by the reduction of H^+ rises sharply with an increasing negative polarization, whereas there is a very small current with an increasing negative polarization for a p-type semiconductor. This current, however, can be increased when the p-type semiconductor is illuminated by light, because then more electrons are excited to the conduction band. This also reveals that the electrons needed for the proton reduction come from the conduction band of the semiconductor. The positive polarization leads to an electrons transfer to the valence band of the semiconductor and displays an anodic current. For a n-type semiconductor, the anodic current is very small because there are not so many holes at valence band, but the current also

rises when the n-type semiconductor is excited by light because of the increased number of holes in valence band; for a p-type semiconductor, the anodic current increases steeply with the increasing of positive polarization. In addition, during flat band potential conditions which denotes the onset of the current, the electrons don't lose any energy during this horizontal transfer process. According to the Frank-Condon principle, the electron transfer is much faster than any reorganization of the solvation shell or of the solvent dipoles [4]. The example for n-type semiconductor under an increasing negative polarization is shown in figure 2.9.

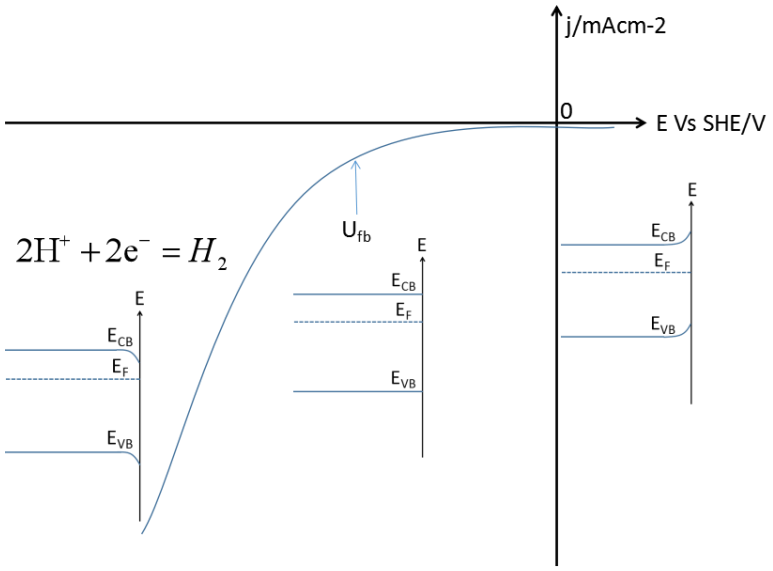

Fig. 2.9 A current-potential curve for a n-type semiconductor in H_2SO_4 solution, and the change of band bending under increasing negative polarization.

Let us now focus on the electron transfer between conduction band and redox system. The cathodic current via the conduction band reads as:

$j_c^-: occupied_{conduction\ band} \xrightarrow{e^-} empty_{redox\ system}$

$$j_c^- = -e k_c^- n_s c_{ox} \tag{2.22}$$

here, k_c^+ is rate constant, $k_c^- = k_{c,\max}^- \exp[-\frac{(E_c - E_{F,redox}^0 - \lambda)}{4kT\lambda}]$, n_s is the density of free electrons at the semiconductor's surface which relates to the bulk electron density n_0 by the Boltzmann distribution $n_s = n_0 \exp(-\frac{e\Delta\Phi_{SC}}{kT})$, λ is the reorganization energy, and $\lambda = \lambda_i + \lambda_0$, λ_i relates to bond length and angles, and λ_0 is solution change energy. C_{ox} is the concentration of oxidized species.

The reverse current, anodic current at conduction band

$j_c^+ : occupied_{redox\ system} \xrightarrow{e^-} empty_{conduction\ band}$

$$j_c^+ = e k_c^+ N_c c_{red} \tag{2.23}$$

In which k_c^+ is rate constant, $k_c^+ = k_{c,\max}^+ \exp[-\frac{(E_c - E_{F,redox}^0 - \lambda)}{4kT\lambda}]$, N_c is the density of energy states within few kT above the conduction band edge: $N_c = \frac{2(2\pi m_e^* kT)^{3/2}}{h^3}$, λ is the reorganization energy. C_{red} is the concentration of reduced species.

From equation (2.22) and (2.23) we can see that the anodic current at the conduction band does not depend on the applied potential, but the cathodic current at the conduction band depend on the applied potential. Any potential various just occur across the space charge layer, and change the band bending $\Delta U_A = \Delta(\Delta\Phi_{SC})$, then the changed band bending vary the density of free electrons at the semiconductor's surface according to the Boltzmann distribution. As a result, the cathodic current at conduction band j_c^- becomes potential-dependent. The potential dependence of anodic and cathodic partial currents at the conduction band and the valence band is shown in figure 2.10.

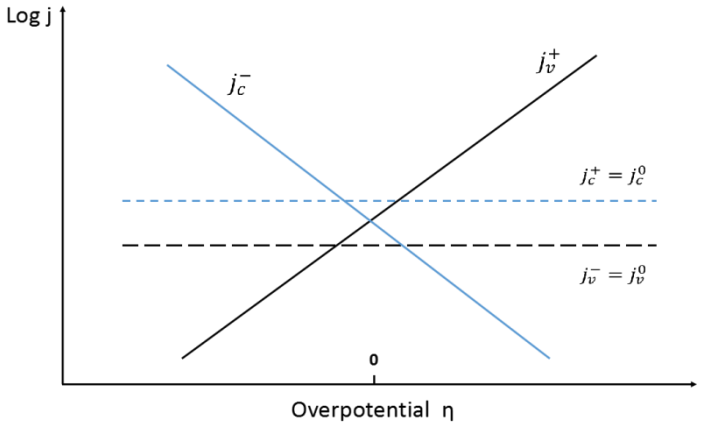

Fig. 2.10 potential dependence of cathodic and anodic partial current at conduction band and valence band of semiconductor electrode [4].

2.3 Electrochemical cell

2.3.1 Electrochemical workstation

An electrochemical workstation is always used in electrochemistry to be able to apply an external overpotential to the electrode and to measure the current flow at the interface of the electrode. The schematics of a work station is illustrated in Fig. 11. Since the electrochemical

reactions are forced by an applied external potential which is given by the potentiostate, an electric energy is converted into a chemical energy through electrochemical reactions. Electrochemical reactions take place in an electrochemical cell which contains a working electrode (WE), a counter electrode (CE), sometimes a reference electrode (RE), and an electrolyte solution. The electrochemistry reaction under investigation occurs at the working electrode, and the commonly used material for working electrode is platinum, gold and carbon. First, the transfer of electrons at the interface of these material is fast and stable; second, these materials are very inactive, so the transferring electrons most likely will not destroy the electrode. The counter electrode is used for closing the electric circuit. It should not limit the reaction which takes place on the working electrode and influence the measured current-potential curve, so the surface of the counting electrode should be sufficiently large. Often used material for the CE for this reason is platinum. A third electrode, the reference electrode, is often used in electrochemical cell to provide a reference potential. The RE is not involved in the redox reaction, so no current will flow across the interface of the RE. Therefore, an equilibrium is enabled at its interface, and this equilibrium ensure a stable reference potential. There are many choices for the reference electrode, such as SHE and Ag/AgCl reference electrode as mentioned before.

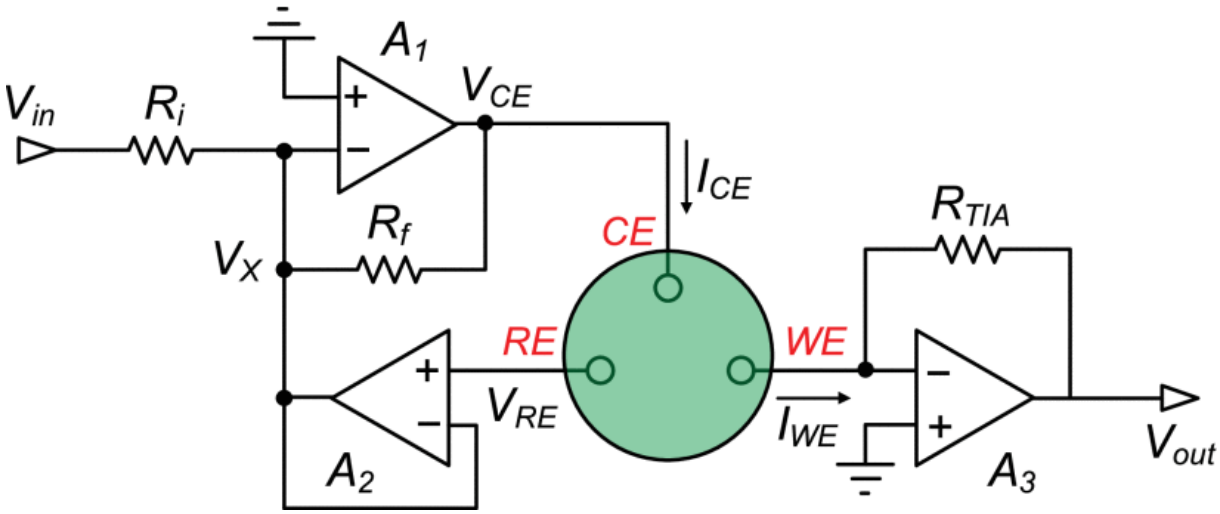

Fig. 2.11 Simple schematic of a potentiostatic circuit [23].

A typical energy diagram for an electrochemical cell is illustrated in figure 2.12. The material of the working electrode is a semiconductor, indicated by its conduction band (VB), valence band (CB), and Fermi level (E_F); the counter electrode is a metal and has a certain Fermi energy (E_F). Because of the double layer in the electrolyte solution, the potential changes across the layer.

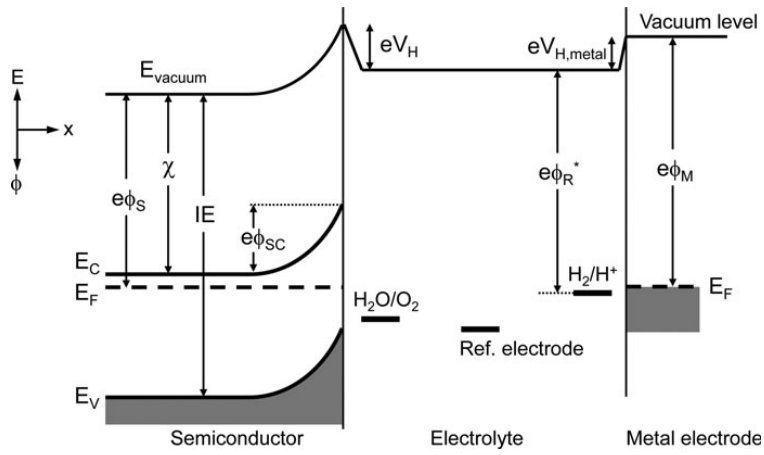

Fig. 2.12 Energy diagram for an electrochemical cell based on a n-type semiconductor working electrode and a metal counter electrode. Helmholtz layer is also present at the semiconductor/electrolyte and metal/electrolyte interfaces, and the potential changes across these layers. The vacuum energy level is taken as a reference; this is the energy of an electron in vacuum at infinite distance. Here χ is the electron affinity and IE is ionization energy, and they are materials constants. Note that the semiconductor work function ($e\phi s$) also depends on the distance to the surface. [18]

2.3.2 Cyclic voltammetry (CV)

There are many kinds of electrochemical measurement methods in electrochemistry to obtain information of property of electrode surface and a redox system. The adopted method in my experiment is called cyclic voltammetry (CV), and it is a type of potentio-dynamic electrochemical measurement. In a cyclic voltammetry measurement, the potential of the working electrode ramps linearly versus time, and the rate of voltage change over time is called scan rate $v = \left|\frac{dE}{dt}\right|$ with a unit of V/s. The voltage is swept at a constant scan rate from a determined limited voltage E1 to another limited voltage E_2, and then goes back to E_1. This way, a triangular voltage profile results as being depicted in figure 2.11. The cycle of the potential sweep can be repeated many times. At the same time, the cyclic voltammetry trace is recorded by plotting the current response of the working electrode versus the applied voltage.

A suitable scan rate v is very important for CV measurement: If v is too fast, the current is dominated by a capacitive current (non-Faradic current) because the redox equilibrium cannot be achieved during a very short time. If the scan rate is too slow, no stable CU trace will be obtained. The best scan rate thus lies in an intermediate range where the recorded current is mainly from redox reaction (Faradic current), and the electric double layer is kept completely charged, so the obtained CV curve can reflect the electrochemical property of the redox system. Cyclic voltammetry is a very powerful measurement method usually being used to obtain

information about the amount of reacting steps, the charge transfer process, the catalytic activity of an electrode surface and so on.

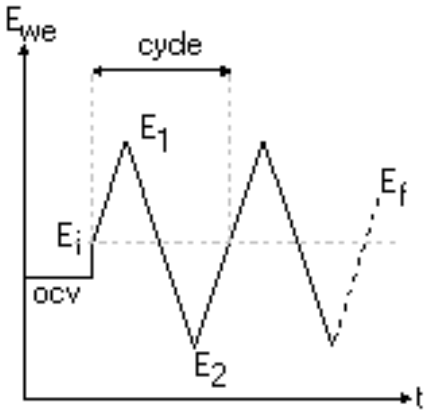

Fig. 2.13 periodic potential change in cyclic voltammetry [24].

2.4 Catalytic process at the surface of electrode

Any catalytic process in an electrochemistry system needs a catalyst, which can be a metal electrode or a semiconductor electrode. In general, the main impact of a catalyst on a reaction is to reduce the activation energy, but it doesn't change the energy of reactant and products. The catalyst accelerates the forward and backward reaction equally. The schematic energy influence of a catalyst is shown in figure 2.14.

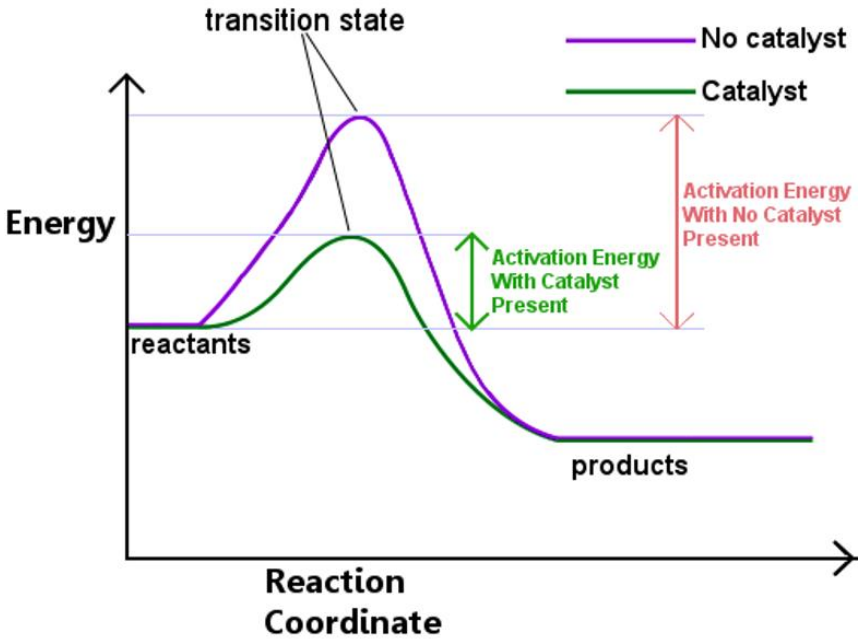

Fig. 2.14 The schematic energy change of a chemical reaction under influence of a catalyst .

Usually the catalyst resides on the surface of an electrode, and the reactant is in liquid phase or gas phase, so this electrochemical reaction also belongs to the class of heterogeneous catalysis. There are four important steps in the heterogeneous catalysis:

- The first step is the adsorption of a reactant to the catalyst surface via physisorption and chemisorption. The physisorption is essentially Van-der-Waals interaction between two molecules, whereas the chemisorption is via covalent or ionic bond between catalyst and reactants, and the strength of chemisorption can determine the activity of a catalyst.
- The second step is the diffusion of the adsorbed reactant to the active sites on the catalyst surface, which are defects, strain, lower atom coordination and so on [25].
- In the third step, a chemical reaction takes place, the adsorbed reactants react with each other and form products.
- The following fourth step is the desorption of the product which is decided by the bonding strength of the product and the catalyst.

For the hydrogen evolution reaction, there are three possible steps [26]:

1. Volmer step: $\mathrm{H^+ + e^- \rightarrow} H_{ad}$
2. Heyrovsky step: $\mathrm{H^+ + e^- +} H_{ad} \rightarrow H_2$
3. Tafel step: $\mathrm{2H_{ad}} \rightarrow H_2$

The Volmer step depicts a process in which a proton in solution is adsorbed on the catalyst surface and reduced to form an adsorbed hydrogen atom; the Heyrovsky step describes that an adsorbed hydrogen atom reacts with a proton in solution and an electron, so a hydrogen molecule is formed and desorbs from the catalyst surface; the Tafel slop depicts the formation of a hydrogen molecule by two adsorbed hydrogen atoms, and it desorbs from the catalyst surface [26]. The Volmer step is the first step in the hydrogen evolution reaction, later, the adsorbed hydrogen atom will form hydrogen gas via the mentioned Heyrovsky step or the Tafel step.

In a cyclic voltametry measurement, when the logarithmic current density is plotted versus the high overpotential, the Tafel slope is obtained, and we can reduce the rate-limiting step of HER [27]. These three steps of HER mentioned above have their characteristic Tafel slope value, the Tafel slope of the Volmer step is 120mV/dec, and the Tafel slope of the Heyrovsky step is 40mV/dec whereas the Tafel slope of Tafel step is 30mV/dec, these valued are experimentally

proved. In a real experiment with a different catalyst, the measured the Tafel slope can be compared with the characteristic Tafel slope, and the rate-limiting step can be found out.

2.5 References

[1] P.W. Atkins, “physical chemistry”, *Oxford University Press*, 1987, Oxford, UK.

[2] C. H. Hamann, A. Hamnett, W. Vielstich, “electrochemistry”, *Wiley-VCH*, 2007, 2., completely rev. and updated en edition, ISBN 978-3-527-31069-2.

[3] H. C. Helgeson and D. H. Kirkham, “Theoretical prediction of the thermodynamic behavior of aqueous electrolytes at high pressures and temperatures; II, Debye-Huckel parameters for activity coefficients and relative partial molal properties,” *Am. J. Sci.*, vol. 274, no. 10, pp. 1199–1261, 1974.

[4] R. Memming, “Semiconductor Electrochemistry”, *Wiley-VCH*, 2000, 2. edition, ISBN 978-3-527-31281-8.

[5] H. Gerischer, “physical chemistry (eds M. Eyring et al.)”, *Academic Press*, 1970, New York.

[6] N. S. Neghmouche, “Analytical Electrochemistry: The Basic Concepts”, *Anal. Electrochem.*, 2007.

[7] G. Inzelt, A. Lewenstam, and F. Scholz, “Handbook of reference electrodes”, *springer*, 2013, ISBN 978-3-642-36187-6.

[8] S. Licht, “semiconductor electrode and photoelectrochemistry”, number v.6 in Encyclopedia of electrochemistry, *Wiley-VCH*, 2002, ISBN 978-3-527-30398-4.

[9] F. J. Vidal-Iglesias, J. Solla-Gullón, A. Rodes, E. Herrero, and A. Aldaz, “Understanding the Nernst equation and other electrochemical concepts: An easy experimental approach for students,” *J. Chem. Educ.*, 2012.

[10] Generalic, Eni. "Standard hydrogen electrode." *Croatian-English Chemistry Dictionary & Glossary*, 20 Oct. 2018. KTF-Split. 1 Aug. 2020. <https://glossary.periodni.com>

[11] R. S. Nicholson, “Theory and Application of Cyclic Voltammetry for Measurement of Electrode Reaction Kinetics,” *Anal. Chem.*, 1965.

[12] R. Burt, G. Birkett, and X. S. Zhao, “A review of molecular modelling of electric double layer capacitors,” *Physical Chemistry Chemical Physics*, 2014.

[13] D. Stigter, “Micelle formation by ionic surfactants. I. Two phase model, Gouy-Chapman model, hydrophobic interactions,” *J. Colloid Interface Sci.*, 1974.

[14] K. B. Oldham, “A Gouy-Chapman-Stern model of the double layer at a (metal)/(ionic liquid) interface,” *J. Electroanal. Chem.*, 2008.

[15] H. Du, X. Lin, Z. Xu, and D. Chu, “Electric double-layer transistors: a review of recent progress,” *Journal of Materials Science*. 2015.

[16] Z. Zhang and J. T. Yates, “Band bending in semiconductors: Chemical and physical consequences at surfaces and interfaces,” *Chemical Reviews*. 2012.

[17] F. Nandjou and S. Haussener, "Degradation in photoelectrochemical devices: Review with an illustrative case study*," J. Phys. D. Appl. Phys.*, 2017.

[18] M. Grätzel, "photoelectrochemical hydrogen production" *Springer*, 2012, ISBN 978-1-4614-1379-0.

[19] J. O. Bockris, A. K. N. Reddy, and M. Gamboa-Aldeco, Modern Electrochemistry - Volume 2A, *Fundamentals of Electrodics*, 2002.

[20] H. Gerischer, "Semiconductor electrode reactions," Adv. *Electrochem. Electrochem. Eng.*, vol. 1, pp. 139–232, 1961.

[21] R. A. Marcus, "Exchange reactions and electron transfer reactions including isotopic exchange. Theory of oxidation-reduction reactions involving electron transfer. Part 4. - A statistical-mechanical basis for treating contributions from solvent, ligands, and inert salt," *Discuss. Faraday Soc.*, 1960.

[22] D. R. Gabe, "The centenary of Tafel's equation," *Transactions of the Institute of Metal Finishing*. 2005.

[23] J. P. de Campos da Costa, W. B. Bastos, P. I. da Costa, M. A. Zaghete, E. Longo, and J. P. Carmo, "Portable Laboratory Platform With Electrochemical Biosensors for Immunodiagnostic of Hepatitis C Virus," *IEEE Sens. J.*, 2019.

[24] EC-Lab Software User's Manual, Version 10.38-August 2014, BioLogic science instrument.

[25] J. K. Nørskov, T. Bligaard, B. Hvolbæk, F. Abild-Pedersen, I. Chorkendorff, and C. H. Christensen, "The nature of the active site in heterogeneous metal catalysis," *Chemical Society Reviews*. 2008.

[26] W. S. Jenks, photocatalytic "reaction pathways - Effect of molecular structure, Catalyst, and Wavelength", in P. Pichat (Editor) "photocatalysis and water purification", page 25-51, *Wiley-VCH Verlag & Co. KGaA*, Weinheim, Germany 2013, ISBN 978-3-527-64540-4.

[27] Y. Li, H. Wang, L. Xie, Y. Liang, G. Hong, and H. Dai, "MoS_2 nanoparticles grown on graphene: An advanced catalyst for the hydrogen evolution reaction," *J. Am. Chem. Soc.*, 2011.

Chapter 3

SAW and its application in chemistry

Surface acoustic waves are mechanical waves which propagate on the surface of a solid. Their mathematic description is governed by the elastic wave equation and respective boundary conditions. In the first part of this chapter, I will introduce the physical properties of 128°y-cut $LiNbO_3$, because this material is mainly used in my experiments. Its elastic and piezoelastic properties decide about the amplitude of surface acoustic vibration and polarization of the material surface when a SAW propagates on it. The second part describes in detail the solvation process of the wave equation and the boundary conditions. Moreover, a vanishing determinant is necessary for SAW to determine the wave vector and phase velocity. After finding out the phase velocity of SAW, amplitude and SAW-induced electric field can be also calculated. The third part will generally introduce the so called interdigital transducer which is normally used to excite SAW, and in the fourth part of this chapter, I will give a basic description of the relationship between SAW and a chemical reaction, especially photocatalysis and electrochemical reaction.

3.1 Surface acoustic wave and piezoelectric material

3.1.1 Physical properties of $LiNbO_3$

Lithium niobate is a ferroelectric material which is usually used for acoustic applications due to its pronounced piezoelectric and pyroelectric properties. It is a human-made single crystal dielectric material which doesn't exist in nature. The growth of the crystal is done by the Czochralski technique, which produces large, high-quality single crystals, and a number of different growth directions are available. All grown crystal structures are non-centro-symmetric, and therefore the crystal is normally poled into single domains when the temperature is below its ferroelectric Cure temperature (1142°C). The basic crystal cell of $LiNbO_3$ consists of a planar sheet of oxygen atoms in a distorted hexagonal close-packed structure, which exhibits three-fold rotation symmetry about its c axis. It has additionally three mirror planes which form a three-fold rotation axis. These two symmetry operations classify $LiNbO_3$ into the 3m point group. The structure of the $LiNbO_3$ crystal is shown in figure 3.1.
When the crystal is compressed along the x axis, the Li^+ and Nb^{3+} ions move closer to the center position of oxygen layers which leads to a reduction of the net polarization, then thereby leave

negative compensatory charges on the +c crystal face. This way, an induced polarization is formed. This phenomenon is called direct piezoelectric effect [1]. As a piezoelectric material, $LiNbO_3$ exhibits an induced polarization with applied stress, and the relationship between the polarization and the stress is linear and can be mathematically written as

$$p = \sum_{j,k} d_{ijk} \cdot \sigma_{jk} \tag{3.1}$$

where p is the induced polarization, σ_{jk} is the second-rank stress tensor, and d_{ijk} is the third-rank piezoelectric stress tensor.

If the strain is chosen as the independent variable, then the induced polarization would also be proportional to strain magnitude, and it can be written as:

$$p = \sum_{j,k} e_{ijk} \cdot s_{jk} \tag{3.2}$$

where e_{ijk} is the third-rank tensor and s_{jk} is the second-rank piezoelectric strain tensor.

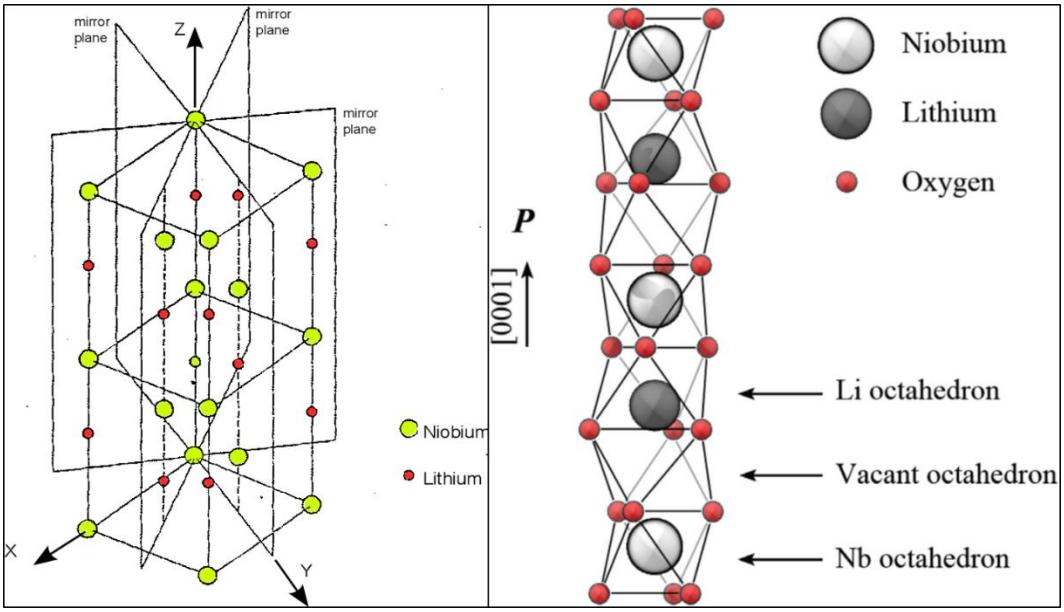

Fig. 3.1 the left picture is the structure of $LiNbO_3$ basic crystal cell with three mirror plane symmetry elements. The right picture is the schematic representation of $LiNbO_3$ crystal structure with highlight of the cationic positions with respect to the oxygen [2].

For a third-rank tensor, the ij subscripts can be customarily [3] simplified into a single subscript by the following substitution.

jk = 11→ 1; jk = 22→2; jk = 33→3;

jk = 12 or 21→6; jk = 23 or 32→4; jk = 13 or 31→5

usually the third-rank tensor contains 18 elements and can be written as a 3×6 matrix. Since the $LiNbO_3$ belongs to 3m point group, the piezoelectric tensors also have the same symmetry, and the d_{ijk} tensor can be reduced from 18 independent elements to 4 independent elements.

$$d_{ijk} = \begin{bmatrix} 0 & 0 & 0 & 0 & d_{15} & -2d_{22} \\ -d_{22} & d_{22} & 0 & d_{15} & 0 & 0 \\ d_{13} & d_{31} & d_{33} & 0 & 0 & 0 \end{bmatrix}$$

A piezoelectric solid also possesses an inverse piezoelectric effect. When $LiNbO_3$ is subjected to an electric field, it will change its shape (strain) and the coefficients between the applied electric field and induced strain are identical to the coefficients between applied stress and induced polarization. Thus, the strain can be expressed as

$$S_{jk} = \sum_i d_{ijk} \cdot E_i \tag{3.3}$$

where s_{jk} is the second-rank strain tensor.

The strain in a solid could also result from the applied stress, since a solid normally has elastic properties. Within the elastic limit of the solid, the caused strain linear relate to the magnitude of the applied stress by Hooke's law:

$$S_{jk} = \sum_{k,l} c_{ijkl} \cdot \sigma_{kl} \tag{3.4}$$

Where the elastic stiffness tensor c_{ijkl} is a fourth-rank tensor, and it is in a form as 6×6 matrix:

$$c_{ijkl} = \begin{bmatrix} c_{11} & c_{12} & c_{13} & c_{14} & 0 & 0 \\ c_{12} & c_{11} & c_{13} & -c_{14} & 0 & 0 \\ c_{13} & c_{14} & c_{33} & 0 & 0 & 0 \\ c_{14} & -c_{14} & 0 & c_{44} & 0 & 0 \\ 0 & 0 & 0 & 0 & c_{44} & c_{14} \\ 0 & 0 & 0 & 0 & c_{14} & c_{66} \end{bmatrix}$$

and $c_{66} = \frac{1}{2}(c_{11} - c_{12})$

A reciprocal expression is written as: $\sigma_{i,j} = \sum_{k,l} s_{ijkl} \cdot S_{kl}$ (3.5)

Where the s_{ijkl} is the elastic compliance tensor, and it is in a form as 6×6 matrix as well:

$$s_{ijkl} = \begin{bmatrix} s_{11} & s_{12} & s_{13} & s_{14} & 0 & 0 \\ s_{12} & s_{11} & s_{13} & -s_{14} & 0 & 0 \\ s_{13} & s_{14} & s_{33} & 0 & 0 & 0 \\ s_{14} & -s_{14} & 0 & s_{44} & 0 & 0 \\ 0 & 0 & 0 & 0 & s_{44} & 2s_{14} \\ 0 & 0 & 0 & 0 & 2s_{14} & s_{66} \end{bmatrix}$$

and $s_{66} = 2(c_{11} - c_{12})$

because of the symmetry operation of the 3m point group, each of the elastic stiffness tensor c_{ijkl} and the elastic compliance tensor s_{ijkl} has only 6 independent coefficients for $LiNbO_3$.

Every material has its permittivity value, which describes the linear relationship between the reduced electric flux density D and the applied electric field E, and the linear relationship of them can be written as

$$D_i = \varepsilon_{ij} \cdot E_j \tag{3.6}$$

where ε_{ij} is the second-rank permittivity tensor, and it can be expressed as a 3×3 matrix. According to the thermodynamic consideration of energy, on the diagonal elements of the permittivity matrix are non-zero. Moreover, because of the symmetric property of $LiNbO_3$, the independent permittivity element could be reduced to 2, so the permittivity tensor can be presented as

$$\varepsilon_{ij} = \begin{bmatrix} \varepsilon_{11} & 0 & 0 \\ 0 & \varepsilon_{11} & 0 \\ 0 & 0 & \varepsilon_{33} \end{bmatrix}$$

Some physical property of $LiNbO_3$ and the value of its tensor is summarized in table 1, and these properties are measured at room temperature.

Table. 3.1 some physical property and the value of its tensor for $LiNbO_3$ (at 25°C)

Congruent Melting Point (approximately)	1250°C
Point Group	3m
Space Group	R3c
Density	4.65 g/cm^3
Mechanical Hardness	5 (Mohs)
Specific Heat	0.15 cal/g·°C
Thermal Conductivity	0.01 cal/cm·sec·°C
Thermal Expansion	$\alpha_a = 15\times10^{-6}$/°C, $\alpha_c = 7.5\times10^{-6}$/°C
Piezoelectric Stress Constants (coulomb/m^2)	d_{15}=3.76; d_{22}=2.43; d_{31}=0.23; d_{33}=1.33
Elastic Stiffness Constants (constant field, 10^{11}newton/m^2)	c_{11}=2.03; c_{12}=0.53; c_{13}=0.75; c_{14} = 0.09; c_{33} = 2.45; c_{44} = 0.60; c_{66} = 0.75
Dielectric Constants (unclamped)	ε_{11} = 85; ε_{33} = 28.7

In my experiments, 128° y-cut $LiNbO_3$ are used to produce Rayleigh-type SAW, so these physical properties should be rotated by the Euler angle [0°, 38°, 0°]. [3]

3.1.2 Surface acoustic wave equation for piezoelectric material

The strain is expressed as the motion of a particle. Suppose a particle in the material moved from position **x** to a new position **x** + **u,** and the point **x** has coordinates (x_1, x_2, x_3), while the amount of displacement has components (u_1, u_2, u_3). Now, if **u** is dependent on **x,** there will be internal forces building up, and the strain relates to the internal forces. Therefore, the strain **S** at any point can be defined as

$$S_{ij} = \frac{1}{2}\left(\frac{\partial u_i}{\partial x_j} + \frac{\partial u_j}{\partial x_i}\right) \tag{3.7}$$

Displacements or rotations which move the material as a whole will cause no strain, because these movements lead to no internal force. Here, the internal force is expressed as a stress tensor T, and the relationship between the strain S and the stress T can be described by Hook's law

$$T_{ij} = c_{ijkl} \cdot S_{kl} \qquad \text{(Hook's law)}$$

When time t is considered in the movement of the particle, the equation of motion can be described by Newton's second law:

$$\rho \frac{\partial^2 u_i}{\partial t^2} = \frac{\partial T_{ij}}{\partial x_i} \tag{3.8}$$

The internal force T_{ij} per unit volume is equal to the mass density ρ multiply by the acceleration, which is $\frac{\partial^2 u_i}{\partial t^2}$. Combine equation (3.7), (3.8) and Hook's law, we can get

$$\rho \frac{\partial^2 u_i}{\partial t^2} = \frac{\partial}{\partial x_i} \frac{1}{2} c_{ijkl} \left(\frac{\partial u_i}{\partial x_j} + \frac{\partial u_j}{\partial x_i}\right) \tag{3.9}$$

The solution of the above equation is the wave propagation in a non-piezoelectric material in the direction of x:

$$u_i = u_i^0 \cdot \exp(j(kx_1 - wt))$$

Here, k is wave vector and ω is the angular velocity, and $j^2 = -1$.

For a piezoelectric material, the situation becomes more complex, because in piezoelectric materials, elastic stress and strain are coupled to electric fields. Therefore, in a homogeneous piezoelectric material, the stress T_{ij} for each particle is not only related to the strain by Hook's law, it is also depended to the applied electric field **E**, and it can be written in a linear relation:

$$T_I = c_{IJ}^E \cdot S_J - d_{Ij} \cdot E_j \tag{3.10}$$

For a – non piezoelectric "normal" material, the electric displacement D is usually caused by the applied electric field E and the permittivity tensor ε_{ij} of the material, but in a piezoelectric material, the electric displacement D is also determined by the strain S_J

$$D_i = e_{iJ} \cdot S_J + \varepsilon_{ij}^S \cdot E_j \tag{3.11}$$

Any wave has its propagation direction, and like the wave vector *k*, the wave displacements are also vectors. It can thus be decomposed like any other vector. For convenience, we decompose the wave into 3 directions, x_1, x_2, and x_3, which is in the directions of three-dimensional coordinates, as showed in figure 3.2. x_1 is in the propagation direction of the wave, and x_3 is perpendicular to the surface of the material.

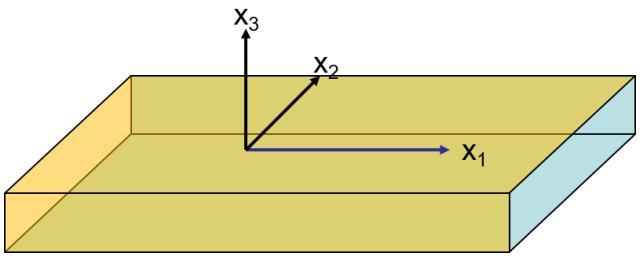

Fig. 3.2 coordinate system for a wave in material.

Since the wave has been decomposed into three components, the mathematical description of the wave can also be decomposed into three equations. For a surface acoustic wave, the wave solution is a little different from normal wave solution, $u_i = u_i^0 \cdot \exp(j(kx_1 - wt))$. Since we know that the surface acoustic wave only propagates on the surface of a material, its amplitude decays in the bulk material. After approximately two wavelengths below the surface, the surface wave is totally damped out. For such reason, the wave solution is in a form like

$$u_i = u_0^{(i)} e^{jkbx_3} e^{j(kx_1 - \omega t)} \qquad \text{(i=1,2,3,4)}$$

where attenuation is damping factor of the wave, x_1 represent the propagation direction of the wave, and the direction of x_3 is normal to the surface of the piezoelectric material. Here we have four wave solutions, because the substrate is a piezoelectric material, the u_4 solution describes the electric potential accompanied by the wave. The u_1 to u_3 solutions describe the mechanic particle movement of SAW in x_1, x_2 and x_3 directions. The total solution is assumed to be a linear combination of terms of this form.

The process of solving the wave equation in piezoelectric materials is complex. In general, the usual way to is to set a value to the unknown velocity v_{saw} to solve the wave matrix equation to get damping factor b value, then check whether the obtained solution in this way is compatible with the boundary conditions. If this is not the case, the process will be repeated again at a newly selected phase velocity v_{saw} until the error falls below a set limit. At the first step, we put equation (3.10) into equation (3.8) and combine equation (3.11), then a matrix equation was gotten as following:

$$\begin{bmatrix} T_1 \\ T_2 \\ T_3 \\ T_4 \\ T_5 \\ T_6 \\ D_1 \\ D_2 \\ D_3 \end{bmatrix} = \begin{bmatrix} c_{11} & c_{12} & c_{13} & c_{14} & c_{15} & c_{16} & -e_{11} & -e_{21} & -e_{31} \\ c_{21} & c_{22} & c_{23} & c_{24} & c_{25} & c_{26} & -e_{12} & -e_{22} & -e_{32} \\ c_{31} & c_{32} & c_{33} & c_{34} & c_{35} & c_{36} & -e_{13} & -e_{23} & -e_{33} \\ c_{41} & c_{42} & c_{43} & c_{44} & c_{45} & c_{46} & -e_{14} & -e_{24} & -e_{34} \\ c_{51} & c_{52} & c_{53} & c_{54} & c_{55} & c_{56} & -e_{15} & -e_{25} & -e_{35} \\ c_{61} & c_{62} & c_{63} & c_{64} & c_{65} & c_{66} & -e_{16} & -e_{26} & -e_{36} \\ e_{11} & e_{12} & e_{13} & e_{14} & e_{15} & e_{16} & \varepsilon_{11} & \varepsilon_{12} & \varepsilon_{13} \\ e_{21} & e_{22} & e_{23} & e_{24} & e_{25} & e_{26} & \varepsilon_{21} & \varepsilon_{31} & \varepsilon_{41} \\ e_{31} & e_{32} & e_{33} & e_{34} & e_{35} & e_{36} & \varepsilon_{31} & \varepsilon_{32} & \varepsilon_{33} \end{bmatrix} \cdot \begin{bmatrix} S_1 \\ S_2 \\ S_3 \\ S_4 \\ S_5 \\ S_6 \\ E_1 \\ E_2 \\ E_3 \end{bmatrix} \quad (3.12)$$

The strain matrix S_J and S_{ij} has a conversion relationship

$$\begin{bmatrix} S_{11} & S_{12} & S_{13} \\ S_{21} & S_{22} & S_{23} \\ S_{31} & S_{32} & S_{33} \end{bmatrix} = \begin{bmatrix} S_1 & \frac{1}{2}S_6 & \frac{1}{2}S_5 \\ \frac{1}{2}S_6 & S_2 & \frac{1}{2}S_4 \\ \frac{1}{2}S_5 & \frac{1}{2}S_4 & S_3 \end{bmatrix}$$

As a plane wave, the strain only varies along the directions of x_1 and x_3, and the strain in the direction x_2 is constant, so $S_2 = 0$. According to the definition of strain matrix S_{ij}, equation (3.7), and putting these four wave equations into equation (3.7), we can get that

$S_1 = S_{11} = \frac{du_1}{dx_1} = iku_1;$ $\quad S_2 = 0;$ $\quad S_3 = iku_3;$ $\quad S_4 = 2S_{23} = \frac{\partial u_2}{\partial x_3} + \frac{\partial u_3}{\partial x_2} = iku_2;$

$S_5 = ik(bu_1 + u_3);$ $\quad S_6 = iku_2$

Generally, an electric field is defined as negative space derivative of an electric potential, and in the situation of surface acoustic wave, the SAW-induced electric potential is present by wave solution u_4, so the relationship between SAW-induced electric field and u_4 are like:

$E_1 = -j\frac{\partial u_4}{\partial x_1} = -jku_4;$ $\quad E_2 = 0;$ $\quad E_3 = -jkbu_4$

Replace S_1, S_2, S_3, S_4, S_5, S_6, E_1, E_2, and E_3 in equation (3.12),

$$\begin{bmatrix} T_1 \\ T_2 \\ T_3 \\ T_4 \\ T_5 \\ T_6 \\ D_1 \\ D_2 \\ D_3 \end{bmatrix} = \begin{bmatrix} c_{11} & c_{12} & c_{13} & c_{14} & c_{15} & c_{16} & -e_{11} & -e_{21} & -e_{31} \\ c_{21} & c_{22} & c_{23} & c_{24} & c_{25} & c_{26} & -e_{12} & -e_{22} & -e_{32} \\ c_{31} & c_{32} & c_{33} & c_{34} & c_{35} & c_{36} & -e_{13} & -e_{23} & -e_{33} \\ c_{41} & c_{42} & c_{43} & c_{44} & c_{45} & c_{46} & -e_{14} & -e_{24} & -e_{34} \\ c_{51} & c_{52} & c_{53} & c_{54} & c_{55} & c_{56} & -e_{15} & -e_{25} & -e_{35} \\ c_{61} & c_{62} & c_{63} & c_{64} & c_{65} & c_{66} & -e_{16} & -e_{26} & -e_{36} \\ e_{11} & e_{12} & e_{13} & e_{14} & e_{15} & e_{16} & \varepsilon_{11} & \varepsilon_{12} & \varepsilon_{13} \\ e_{21} & e_{22} & e_{23} & e_{24} & e_{25} & e_{26} & \varepsilon_{21} & \varepsilon_{31} & \varepsilon_{41} \\ e_{31} & e_{32} & e_{33} & e_{34} & e_{35} & e_{36} & \varepsilon_{31} & \varepsilon_{32} & \varepsilon_{33} \end{bmatrix} \cdot \begin{bmatrix} jku_1 \\ 0 \\ jku_3 \\ jku_2 \\ jk(bu_1 + u_3) \\ jku_2 \\ -jku_4 \\ 0 \\ -jkbu_4 \end{bmatrix} \quad (3.13)$$

So T_1, T_2, T_3, T_4, T_5, T_6, D_1, D_2, and D_3 can be expressed as a function of u_1, u_2, u_3, and u_4. Then we need the wave equation (3.8), and put the wave solution $u_i = u_0^{(i)} e^{jkbx_3} e^{j(kx_1 - \omega t)}$ (i=1,2,3,4) into equation (3.8). We know that for a plane wave, any physical property only

varies along the direction of x_1 and x_3, and it don't vary in the direction of x_2, so we can get three equations at the end:

$$\frac{\partial T_1}{\partial x_1} + \frac{\partial T_5}{\partial x_3} = -w\rho u_1 \tag{3.14}$$

$$\frac{\partial T_6}{\partial x_1} + \frac{\partial T_4}{\partial x_3} = -w\rho u_2 \tag{3.15}$$

$$\frac{\partial T_5}{\partial x_1} + \frac{\partial T_3}{\partial x_3} = -w\rho u_3 \tag{3.16}$$

Where ω is angular velocity $\omega = \frac{2\pi}{T}$, and T is the period. Wave vector $k = \frac{2\pi}{\lambda}$ and the phase velocity $\upsilon = \frac{\lambda}{T} = \frac{\omega}{k}$. ρ is the mass density of the material.

Since the piezoelectric material is taken to be an insulator, so the div(**D**)=0. Hence, we get:

$$\frac{\partial D_1}{\partial x_1} + \frac{\partial D_3}{\partial x_3} = 0 \tag{3.17}$$

In order to finally solve the wave equation, we put u_1, u_2, u_3, and u_4 expressed T_1, T_2, T_3, T_4, T_5, T_6, D_1, D_2, and D_3 into equation (3.14), (3.15), (3.16), and (3.17), then we can get four equations. Write these four equations into matrix form:

$$\begin{bmatrix} M_{11} - \rho v^2 & M_{12} & M_{13} & M_{14} \\ M_{21} & M_{22} - \rho v^2 & M_{23} & M_{24} \\ M_{31} & M_{32} & M_{33} - \rho v^2 & M_{34} \\ M_{41} & M_{42} & M_{43} & M_{44} \end{bmatrix} \cdot \begin{bmatrix} u_0^1 \\ u_0^2 \\ u_0^3 \\ u_0^4 \end{bmatrix} = 0 \tag{3.18}$$

Where $M_{11} = c_{55} \cdot b^2 + 2c_{15} \cdot b + c_{11}$; $M_{22} = c_{44} \cdot b^2 + 2c_{46} \cdot b + c_{66}$;
$M_{33} = c_{33} \cdot b^2 + 2c_{35} \cdot b + c_{55}$; $M_{12} = c_{45} \cdot b^2 + (c_{14} + c_{56}) \cdot b + c_{16}$;
$M_{13} = c_{35} \cdot b^2 + (c_{13} + c_{55}) \cdot b + c_{15}$; $M_{23} = c_{34} \cdot b^2 + (c_{36} + c_{45}) \cdot b +$
c_{56};$M_{14} = e_{35} \cdot b^2 + (e_{15} + e_{31}) \cdot b + e_{11}$; $M_{24} = e_{34} \cdot b^2 + (e_{14} + e_{36}) \cdot b + e_{16}$;
$M_{34} = e_{33} \cdot b^2 + (e_{13} + e_{35}) \cdot b + e_{15}$; $M_{44} = -(\varepsilon_{33} \cdot b^2 + 2\varepsilon_{13} \cdot b + \varepsilon_{11})$;

The wave equation matrix (3.18) has non-trivial solutions, only if its determinant is zero. Thus, the usual way to solve this problem is to set a value to the unknown phase velocity v_{saw} and put it into the wave equation matrix (3.18). The zero determinant produces an eight-order algebraic equation in b, which therefore leads to eight solutions of b_n, which are in form of complex conjugate pairs. Only the b_n with a negative imaginary part are correct, because the surface acoustic wave is always damped inside the material. so for $x_3 \rightarrow 0$, the SAW disappears, and the wave solution $u_i = u_0^{(i)} e^{jkbx_3} e^{j(kx_1 - \omega t)}$ must be 0. As a result, the four damping factors are found by setting one phase velocity value, among them there are three roots with negative

imaginary value. Every wave solution component is linear combined by four solutions which have a different b_n value. Therefore, the wave solution is written as:

$$u_i = \sum_{n=1}^{4} u_i^{(n)} = \sum_{n=1}^{4} C_n a_{in}\, e^{jkb_n x_3} e^{j(kx_1 - \omega t)} \qquad \text{(i=1, 2, 3, 4)}$$

Here a_{in} is the amplitude of each partial wave, and the index *i* indicates the component of wave equation. At the same time, the index *n* indicates the component of b_n. This finally leads to 16 a_{in} values. C_n is the coefficient, which indicates the "mixing ratio" of the partial waves. C_n can be calculated by using two boundary conditions for surface acoustic waves. Now, we go to the last step in order to finally find out the right phase velocity. Here, the amplitudes and coefficients of the surface acoustic wave should satisfy the boundary conditions at the surface.

1. One is the mechanical boundary condition: the surface of the material should be stress free, which means that there should be no surface forces acting on it. The stress free condition can be written as $T_{31} = T_{32} = T_{33} = 0$;

2. The other boundary condition is the electrical boundary condition, which is imposed by Maxwell's equations: The normal component of D should be continuous across the interface, and it expressed as $D_3 = D_3'$, where D_3 is the electric displacement field in the piezoelectric substrate and D_3' the electric displacement field in the air.

We know that the electric potential at the surface can be mathematically described as

$$\acute{\emptyset} = u_4^{(i)} e^{-ikx_3} e^{i(kx_1 - \omega t)}$$

so we can deduce the electric displacement field in the air as follow

$$D_3' = \varepsilon_0 E_3 = -\varepsilon_0 \frac{d\acute{\emptyset}}{dx3} = ik\varepsilon_0 \acute{\emptyset}$$

Then, while putting the assumed solutions into the mechanical and electrical boundary conditions, we can get a set of four homogeneous equations in terms of unknown amplitudes and coefficients as before

$$\begin{bmatrix} \alpha_{1n}(c_{31} + bc_{35}) + \alpha_{2n}(c_{36} + bc_{34}) + \alpha_{3n}(c_{35} + bc_{33}) + \alpha_{4n}(e_{13} + be_{33}) \\ \alpha_{1n}(c_{41} + bc_{45}) + \alpha_{2n}(c_{46} + bc_{44}) + \alpha_{3n}(c_{45} + bc_{43}) + \alpha_{4n}(e_{14} + be_{34}) \\ \alpha_{1n}(c_{51} + bc_{55}) + \alpha_{2n}(c_{56} + bc_{54}) + \alpha_{3n}(c_{55} + bc_{53}) + \alpha_{4n}(e_{15} + be_{35}) \\ \alpha_{1n}(e_{31} + be_{35}) + \alpha_{2n}(e_{36} + be_{34}) + \alpha_{3n}(e_{35} + be_{33}) - \alpha_{4n}(\varepsilon_{13} + b\varepsilon_{33} - i\varepsilon_0) \end{bmatrix} \cdot \begin{bmatrix} C_1 \\ C_2 \\ C_3 \\ C_4 \end{bmatrix} = 0$$

For the existence of non-trivial solutions, the determinant matrix of above equation must be equal to zero. The value of the determinant decided by the velocity of SAW, if the determinant of this boundary condition matrix RBM is greater than the error to be tolerated, a different v_{SAW} value will be selected and the whole solution process will be repeated by using the new v_{SAW};

if the determinant of this boundary condition matrix RBM is equal or less than the tolerated error, the speed of the SAW has been found and the problem is solved. In addition, the zero determinant produces an algebraic equation in terms of a_{in}, and the displacement amplitudes ought to be some complex value, and as a consequence the boundary matrix determinant is also complex. After finding out the right v_{SAW}, the b_n, a_{in}, and c_n can be determined, so the expression of surface acoustic wave could also be obtained.

There is a dispersion relation with the found v_{SAW}:

$$\omega = v_{SAW} \cdot k = v_{SAW} \cdot \frac{2\pi}{\lambda} \tag{3.19}$$

so the relationship between v_{SAW} and frequency f is derived as:

$$f = \frac{v_{SAW}}{\lambda} \tag{3.20}$$

It should be noted that the v_{SAW} in first order is only decided by the property of the substrate material, and independent of the frequency f. The individual field solutions u_i have a fixed relationship to each other, and the final SAW solution is the superposition of these individual field solutions u_i, $u = \sum_{i=1}^{4} u_i$. The solved partial solutions u_i only provides relative values of displacements of particles in the substrate medium, and it is difficult to find absolute values for these variables because of the homogeneity of equations. Moreover, the wave solutions discussed above are surface acoustic waves which propagate on the free surface of the piezoelectric material. When the surface is for example covered by a thin massless metal layer, the electrical boundary condition boundary conditions will change, $D_3 = D_3' = 0$. Therefore, the v_{SAW} will be different from that for the free surface. It can be quite complex to incorporate the electrical and mechanical perturbations in the analytical solution, for instance, effect of the mass.

3.1.2 Surface acoustic wave solution for 128° y-cut $LiNbO_3$

First, the physical property values for the 128°y-cut $LiNbO_3$ are used to solve the v_{SAW}, as we have analyzed in the previous section, v_{SAW} is decided by the determinant of this boundary condition matrix, and a right v_{SAW} will let the error of the determinant of boundary condition matrix to be less than a tolerant value. Figure 3.3 shows the error values in the speed search for 128° y-cut $LiNbO_3$, here the RBMo represent the determinant of this boundary condition matrix for an open surface, and the minimization of RBMo lead to the v_{SAW} = 3983m/s for an open surface; the RBMs represent the determinant of this boundary condition matrix for a shorted surface, where the v_{SAW} = 3874m/s was achieved for a shorted surface.

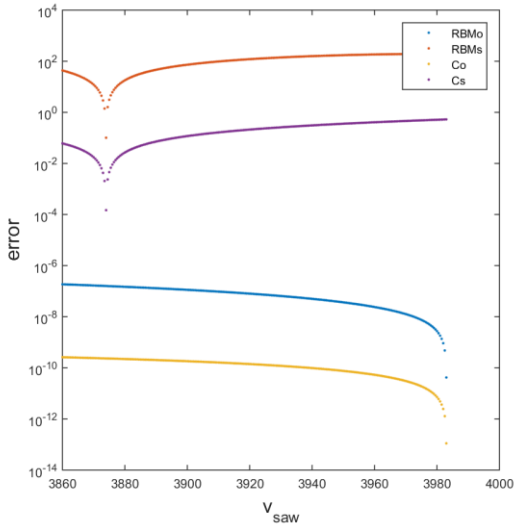

Fig. 3.3 the error of boundary matrix versus speed of v_{SAW} for 128° y-cut $LiNbO_3$. The minimum at 3983m/s corresponds to the Rayleigh-SAW for an open surface, and the minimum at 3874m/s corresponds to the SAW for a shorted surface.

After finding out the right velocity of SAW, then the v_{SAW} is put into the wave equation matrix (3.18), and we obtain 4 suitable values of the damping factor b_n, than a_n and c will be also determined. Fig. 3.4 is the 3D schematic illustration of surface acoustic wave in 128° y-cut $LiNbO_3$. Here, z is the direction perpendicular to the surface of 128° y-cut $LiNbO_3$, and z=0 indicates the surface of the substrate. In the figure, I only show the depth of 2λ under the surface. x is the SAW propagation direction, and the wave propagate from x=0 to x=2λ in the figure. Fig. 3.4(a) illustrates the SAW-induced electric potential in the material, and we can see that at the surface of the material, the electric potential is wave shaped and the positive potential and the negative potential are alternatively distributed. Below the surface, the electric potential has a peak first, and then decays gradually to zero at a depth of ≈2λ. Fig. 3.4(b) shows the particle displacement along the x direction, which is the same direction of the SAW propagation, at the surface of the material, the displacement has its maximum value and below the surface into the substrate, it decreases sharply and then increase again, finally it also decays to zero at the depth of ≈2λ. Fig. 3.4(c) shows the particle displacement along the z direction, which is perpendicular to the surface. At the surface of the material, this displacement has its maximum value and then gradually decays to zero at the depth of 2λ. The motion of the material is in the sagittal plane, which only contains the surface normal and the propagation direction. Moreover, the movement of an individual particle is elliptically polarized.

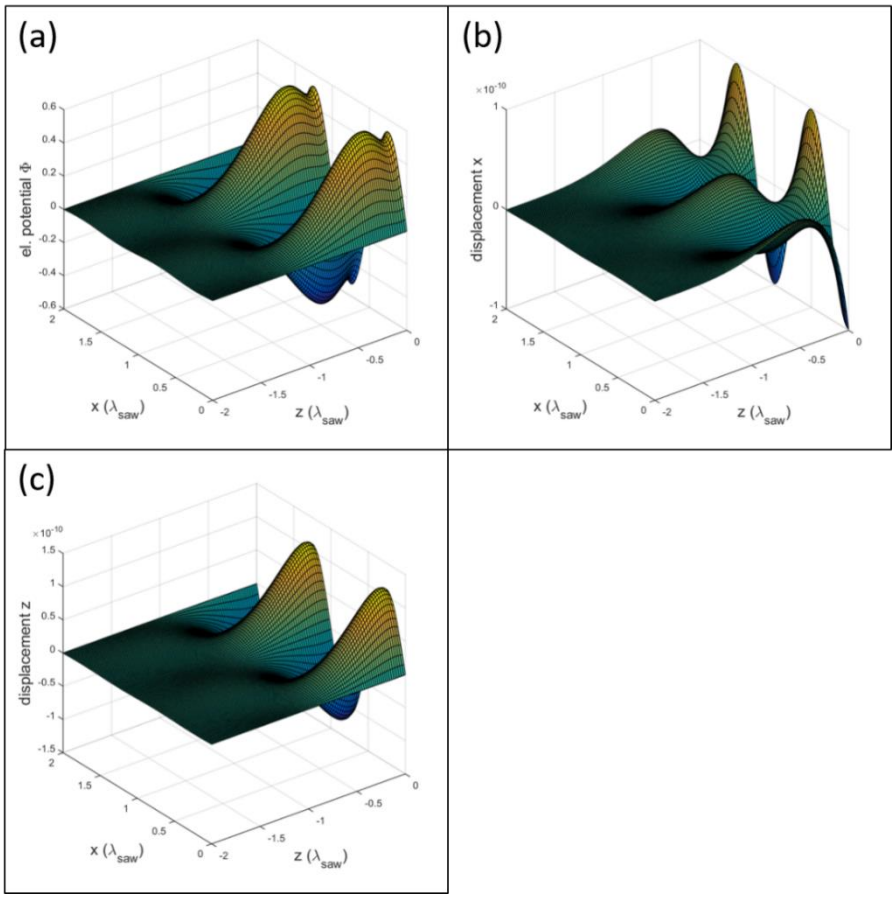

Fig. 3.4 the 3D schematic illustration of surface acoustic wave in 128° y-cut $LiNbO_3$.

For my experiment, the particle displacement and the electric potential at the surface are very important, because the chemical catalyst is located directly on the surface of the substrate. The particle displacement and the electric potential at the surface are illustrated in left panel figure 3.5. In the right panel of figure 3.5 shows the SAW-induced electric field at the surface, and the electric field can be deduced by $E = \partial\emptyset/\partial l$, and it is shown in the right panel of figure 3.5. As shown in figure 3.5, the out-of-plane displacement (u_z) is stronger than the in-plane displacement (u_x and u_y), and there are only two electric fields, one is normal to the surface (E_z) and the other is along the SAW propagation direction (E_x), and the absolute value of E_x is larger than E_z. there is no electric field at y direction, which is in the plane and perpendicular to the SAW propagation direction.

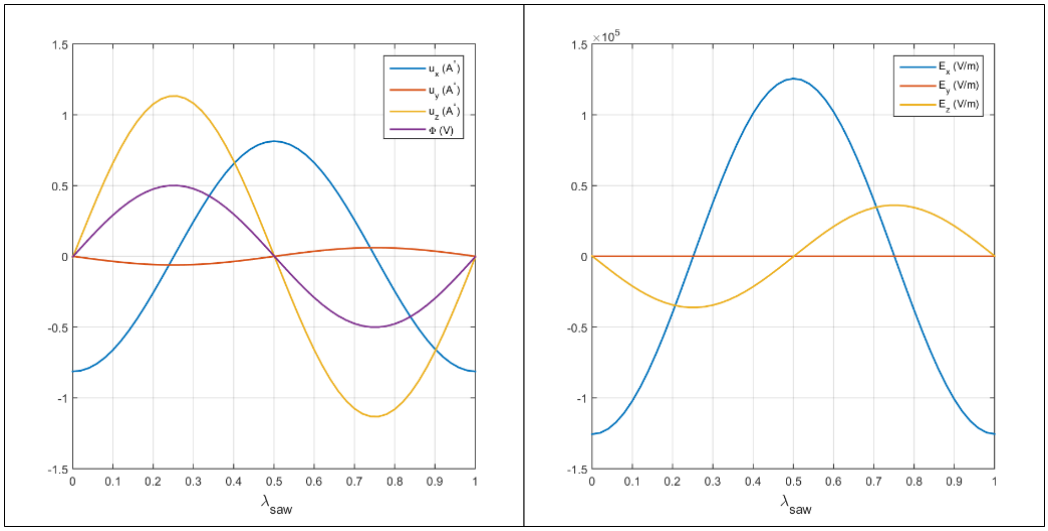

Fig. 3.5 The panel illustrate the particle displacement and the electric potential at the surface, and the right panel shows the SAW-induced electric field at the surface.

Moreover, the SAW induced electric potential (∅), electric field and amplitude of mechanic vibration are related to the power of the surface acoustic wave P_{SAW} [4].

$$\text{Potential:} \qquad P_{SAW} = \frac{1}{2}\frac{A}{\lambda} y_0 |\emptyset|^2 \tag{3.21}$$

Here, A is beam width of the SAW, λ is the wavelength and y_0 a material dependent constant ($y_{0,LiNbO_3}(128°) = 0.21mS$). From equation (3.21) we see that the increase of surface potential is related to the square root of power of SAW, as expected.

$$\text{Electric field:} \qquad E_x = -\frac{\partial \emptyset}{\partial x} = jk\emptyset, \qquad E_y = -\frac{\partial \emptyset}{\partial y} = 0, \qquad E_z = -\frac{\partial \emptyset}{\partial z} \tag{3.22}$$

here, E_x and E_y are SAW-induced in-plane electric field, and x is SAW propagation direction. E_z is the out-of-plane electric field, and the z direction is perpendicular to the surface of the substrate. Since SAW is travelling along the x direction, $\partial/\partial x$ can be represented by j·k, here k is the wave vector. The in-plane electric field E_y is always zero because SAW is a kind of travelling wave and is uniform in y direction. $\partial/\partial z$ can be represented as a sum of decaying exponentials because the SAW decays underneath the surface of substrate. From the equation (3.22) we know that these electric fields are proportional to the surface potential.

The displacement at the surface are also related to the surface potential ∅ through constants c_x, c_y and c_z.

$$\text{Mechanical vibration:} \qquad u_x = c_x \cdot \emptyset, \qquad u_y = c_y \cdot \emptyset, \qquad u_z = c_z \cdot \emptyset \tag{3.23}$$

where u_x is the displacement along x direction, u_y is the displacement along y direction and u_z is the displacement along z direction. The equations (3.20), (3.21) and (3.22) indicate that the SAW-induced surface potential, electric field and mechanical vibration are positively related to

square root of SAW power. When SAW power increases, these SAW-induced factors will also increase.

3.2 Interdigital transducer

Acoustic wave devices have been commercially used for more than 60 years, and it is especially widely used as a component of filters in the telecommunication industry. In order to determine the type of mode of a surface wave, the piezoelectric material and the geometry of the interdigital transducer (IDT) are very important factors. The IDT acts as a means of generating and receiving wave. In a simple delay-line SAW device there are usually two IDTs opposed to each other. One is used as a transmitter to convert the input rf voltage into SAW, and the other acts as a receiver to convert the received SAW back into an output rf voltage. Additionally, the generated surface waves travel along the delay-line and its amplitude is in the order of only $10^{-5}\lambda$. The IDT are made of arrays of metal electrodes fingers, being connected to two bus bars, separately. When these two bars are connected to a rf signal, with a proper frequency, the IDT causes expansion and contraction of the piezoelectric material underneath which leads to the launch of surface acoustic waves. Since for such a simple IDT, the SAW radiates bidirectionally, only half of the SAW power travels directly to the output IDT, whereas the other half SAW power travels toward the opposite direction and becomes finally lost, which results in an "internal" 3dB loss. Electronically, an IDT can be treated as a three port device, one electric port and two acoustic ports. SAW device are typically employed from 10MHz to 3GHz [5], at higher frequency there are physical limitations like mass loading, surface scattering and also because the IDT electrodes become too narrow to fabricate. At lower frequencies, the IDT will become impractically large.

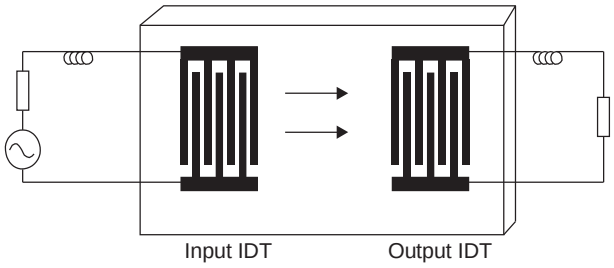

Fig. 3.6 Basic surface acoustic wave device

In my experiments, single electrode IDTs are used, and in this type IDTs have a uniform figure electrode separation and uniform finger overlap as shown in figure 3.6. The designed acoustic wavelength λ is equal to 4 times of the width of electrode, $\lambda = 4 \times d$. The center-to-center

interdigital spacing is λ/2. A SAW device with a designed resonance frequency f_0 can be calculated by $f_0=v_0/\lambda$, where v_0 is the SAW velocity in the piezoelectric material. The bandwidth B of the generated SAW signal is determined by the number of finger pairs: $B=2/N_p$, where N_p is the number of finger pairs.

An IDT can be represented by a parallel circuit, which consist of a radiation conductance $G_a(f)$, an acoustic susceptance $B_a(f)$ and a transducer with total capacitance C_t as shown in Fig. 3.7, and the conductance $G_a(f)$, an acoustic susceptance $B_a(f)$ and total capacitance C_t can be calculated by the following equations [6].

$$G_a(f) = G_a(f_0)\left[\frac{sinx}{x}\right]^2 \tag{3.24}$$

$$B_a(f) = B_a(f_0)[(\frac{sin(2x)-2x}{2x^2}] \tag{3.25}$$

and

$$x = (f - f_0)\frac{\pi N_p}{f_0} \tag{3.26}$$

where f_0 is resonance frequency, N_p the number of electrode pairs, and $G_a(f_0)$ is the conductance at resonance frequency.

$$G_a(f_0) = 8K^2 f_0 C_t N_p \tag{3.27}$$

and

$$C_t = C_0 W N_p \tag{3.28}$$

Here, K is the coupling coefficient of piezoelectric material, W is the overlap between the electrodes, and C_0 is the capacitance per electrode pair per unit length, its unit is pF/m, and its value can be obtained by the following equation:

$$C_0 = 2 \times (6.5\eta^2 + 1.08\eta + 2.37)(\varepsilon_r + 1) \tag{3.29}$$

here η is metallization ration, and $\eta = \frac{2\times d}{\lambda}$, d is the width of electrode and λ is the SAW wavelength. ε_r is the relative permittivity of the piezoelectric material.

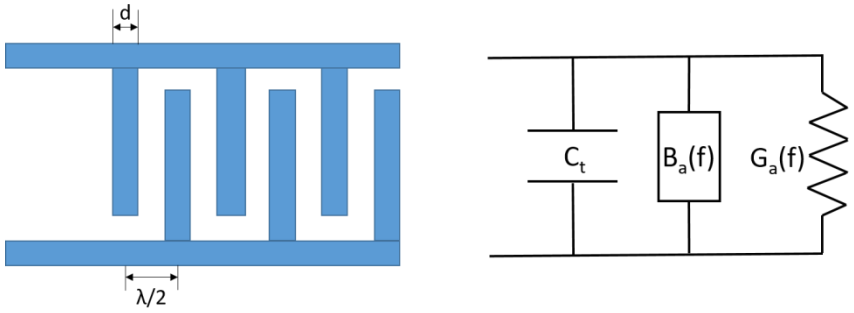

Fig. 3.7 basic structure of single electrode IDT and its equivalent circuit model.

The radiation conductance $G_a(f)$, an acoustic susceptance $B_a(f)$ and total capacitance C_t can be also modeled as a R, L and C equivalent circuit, where

$$R = \frac{1}{G_a(f_0)} \tag{3.30}$$

$$L = \frac{N_p}{4f_0 G_a(f_0)} \tag{3.31}$$

$$C = \frac{G_a(f_0)}{(\pi^2 f_0)N_p} \tag{3.32}$$

the most important character of an IDT is its impedance Z, which can be expressed as

$$Z = R + jwL + \frac{1}{jwC} \tag{3.33}$$

At the resonance frequency, the impedance of IDT should be equal to 50 Ohm on the purpose to matched with the impedance of the measurement system. As the result, the impedance of the IDT is mostly decided by the coupling coefficient K and total capacitance as reduced in equation (3.34), and according to the equations (3.28) and (3.29), we can design the overlap of the electrode finger, the number of finger pair to fit its impedance to 50Ohm.

$$Z_0 = \frac{1}{G_{a0}} + jw\frac{N_p}{4f_0 G_{a0}} + \frac{1}{jw\frac{G_{a0}}{(\pi^2 f_0)N_p}} = \frac{1}{G_{a0}} = \frac{1}{8k^2 f_0 C_t N_p} \tag{3.34}$$

3.3 SAW and photocatalytic water splitting

The following chapter is based in wide parts on our publication “SAW enhanced water splitting reaction with Methanol as a sacrifice material” [7].

TiO_2 is a widely used semiconductor catalyst for photochemical water splitting to produce hydrogen. However, there are some drawbacks of its photocatalytic properties due to its low efficiency of light adsorption, the fast charge carrier recombination and the slow surface redox reaction rate [8,9]. Therefore, much effort has been devoted to improve its photocatalytic efficiency, and the most important issue is to prolong the charge carrier lifetime by efficiently preventing electron hole recombination. In order to obtain longer lifetimes of the charge carriers in semiconductors, various heterostructures have been constructed, such as p-n junction [10], Schottky junctions [11] and z-scheme heterostructures [12]. The key point for these heterostructures is their built-in electric field at the material interface, which enhances the charge carrier separation and thus hinder their recombination. In an attempt to easily arise controllable electric fields in photocatalysts, there is a growing body of work which focuses on controlling the photochemical reaction by employing the polarization of ferroelectric materials. Ferroelectric materials have a non-centrosymmetric crystal structure, which leads to charge separation and thus polarization by supplying an external force. Many researches have shown

that this polarization can in fact enhance the separation of photoinduced charge carriers in a photocatalyst and to promote surface chemical reactions. Rohrer and coworkers for example have done some research on a heterostructure photocatalyst comprising of a ferroelectric core ($PbTiO_3$) and a non-ferroelectric TiO_2 shell [13]. They could show that the degradation rate for methylene blue by using such a $PbTiO_3$-TiO_2 heterostructure catalyst turns out to be about five times faster than $PbTiO_3$ or TiO_2 alone and any mixture of both. They reason that this enhancement of the catalytic effect is due to the ferroelectric polarization which causes a band bending at the interface between the ferroelectric and the photocatalyst. This band bending in turn enhances the separation of photoexcited electrons and holes.

A similar work on the piezo- and also ferroelectric materials $LiNbO_3$ and $LiTaO_3$ combined with the TiO_2 photocatalyst was pioneered by Inoue and coworkers in the 1980s [14]. In their experiment, they employed conventional Pt loaded TiO_2 for a water splitting reaction, and by determining the amount of produced hydrogen, they found that the activity for the following different material and polarization combinations turned out to be ranked like: $LiNbO_3$(neg. polar surface)/TiO_2 > $LiNbO_3$(pos. polar surface)/TiO_2 > $LiTaO_3$ (parallel polar surface)/TiO_2 > α-Al_2O_3(nonpolar surface)/TiO_2. The promoted catalytic activity was obviously not only due to polarization induced band bending in TiO_2, but also due to influenced adsorption of H_2 and O_2 on catalyst's surface.

After the discovery that static surface polarizations quite strongly affect the catalyst action on ferroelectric materials, also dynamic surface polarizations like those being produced by Surface Acoustic Waves (SAW) on piezoelectric materials have attracted attention in recent years. SAW can be easily excited and then propagate on piezoelectric crystals, and their frequency and vibration mode can be precisely designed and controlled. SAW propagates at the surface of substrate and are accompanied by the piezoelectric fields being produced by the local surface deformations of the wave. Since the surface acoustic waves hence not only provide well defined displacements of any surface volume element but they are also accompanied by strong electric fields, which provide a spatio-temporal surface polarization. However, this continuously varying system is different from the above mentioned static polarization, which could prevent the surface form achieving thermodynamic equilibrium with its environment [15]. Moreover, it is thus expected that the SAW driven time-dependent alternating polarization in fact can more efficiently activate surface mounted catalysts. On the other hand, also the SAW induced surface periodic spatial temporal deformations might also benefit the activity of surface mounted

catalysts, as these rapid deformations might also affect both adsorption and desorption of reactant on the catalyst surface [16, 17] and hence also could positively affect the active phase of catalyst.

3.4 SAW and electrochemical hydrogen evolution reaction

The following section is based in wide parts on our publication "Tunable electrochemical hydrogen evolution reaction employing Surface Acoustic Waves" [18].

Electrochemical water splitting is also an attractive method to generate hydrogen gas, and platinum is still the most efficient catalyst for the HER with its low overpotential, high exchange current density and small Tafel slope [19], but due to its scarcity and high cost, the water electrolysis approach is very expensive and this limit its widespread implementation. In the recent years, some non-Pt catalyst electrode has been employed for the hydrogen evolution reaction, like MoS_2 [20,21], gold single-crystal electrodes [22,23] and Ni-based alloys [24,25]. For example, Wang et al. reported a electrochemical cycling treated Au-NPs/GCES electrode, which could obtain a decreased Tafel slope of 76.6mV/dec toward HER [26]. Even though these non-Pt catalysts exhibit promising catalytic property on hydrogen evolution reaction, they are still inferior to Pt with their relatively high overpotentials and small exchange current density. One strategy is to reduce the amount of Pt by depositing Pt nanoparticles on oxide [26,27], since Pt content can achieve small Tafel slope and high exchange current density. Zhang et al. have studied the Pt-SnO_2 flower-like nanostructures which could achieved a current density of $40mA \cdot cm^{-2}$ at 300mV overpotential in $0.1MH_2SO_4$ solution, and this catalyst shows a Tafel slope of 111mV/dec and the exchange current density of $0.46mA \cdot cm^{-2}$ for hydrogen evolution reaction [27]. Ham et al. have reported the Pt decorated W_2C microsphere catalyst which a Tafel slope of 103mV/dec and the exchange current density of $2.08mA \cdot cm^{-2}$ for HER, and its current density could reach $15.8mA \cdot cm^{-2}$ at only 10mV overpotential [28]. All the relevant papers until now have been dedicated to change the structure of catalyst itself, on the other hand, the catalytic systems with tunable activity are also very interesting. We here study the HER activity of some non-Pt catalysts and the outer force of surface acoustic wave. the propagation of SAW is accompanied by a spatio-temporal mechanical vibration and the induced piezoelectric field on the surface, which enable the utilization in a number of applications, eg. micro- and nanoscale manipulation of particles, microfluidic device [29,30],enhancement of surface catalysis [31-33], etc. For instance, the Rayleigh type acoustic wave have a mechanical

displacement normal to the surface of $LiNbO_3$ substrate. When it is in contacts with a liquid phase, the normal displacement will cause tangential fluid motion along the interface, and lead to liquid circulation near it. This phenomenon is called the acoustically induced streaming effect [34], and probably this streaming effect could affect the activity of working electrode in an electrochemical reaction, which is rarely studied by other groups.

3.5 Reference

[1] Trolier-McKinstry S. (2008) Crystal Chemistry of Piezoelectric Materials. In: Safari A., Akdoğan E.K. (eds) "Piezoelectric and Acoustic Materials for Transducer Applications." *Springer,* Boston, MA. ISBN 978-0-387-76538-9

[2] S. Sanna and W. G. Schmidt, "$LiNbO_3$ surfaces from a microscopic perspective," *Journal of Physics Condensed Matter*. 2017.

[3] J. Tichý, J. Erhart, E. Kittinger, and J. Přívratská, "Fundamentals of piezoelectric sensorics: Mechanical, dielectric, and thermodynamical properties of piezoelectric materials." *Springer,* 2010. ISBN 978-3-540-43966-0

[4] S. Datta, "Surface Acoustic Wave Devices." *Prentice Hall,* 1986.

[5] V. K. Varadan, K. J. Vinoy, and K. A. Jose, *RF MEMS and Their Applications*. 2002.

[6] W. R. Smith, H. M. Gerard, T. M. Reeder, H. J. Shaw, and J. H. Collins, "Analysis of Interdigital Surface Wave Transducers by use of an Equivalent Circuit Model," *IEEE Trans. Microw. Theory Tech.,* 1969.

[7] S. Wang, R. Herrmann, A. Wixforth, C. Westerhausen, "SAW enhanced water splitting reaction with Methanol as a sacrifice material," *to be published*

[8] T. Hisatomi, J. Kubota, and K. Domen, "Recent advances in semiconductors for photocatalytic and photoelectrochemical water splitting," *Chemical Society Reviews*. 2014.

[9] A. Kudo and Y. Miseki, "Heterogeneous photocatalyst materials for water splitting," *Chem. Soc. Rev.,* 2009.

[10] J. Zhang, S. Z. Qiao, L. Qi, and J. Yu, "Fabrication of NiS modified CdS nanorod p-n junction photocatalysts with enhanced visible-light photocatalytic H_2-production activity," *Phys. Chem. Chem. Phys.,* 2013.

[11] X. Li *et al.*, "Graphene-on-silicon schottky junction solar cells," *Adv. Mater.,* 2010.

[12] P. Zhou, J. Yu, and M. Jaroniec, "All-solid-state Z-scheme photocatalytic systems," *Advanced Materials*. 2014.

[13] L. Li, Y. Zhang, A. M. Schultz, X. Liu, P. A. Salvador, and G. S. Rohrer, "Visible light photochemical activity of heterostructured $PbTiO_3$-TiO_2 core-shell particles," *Catal. Sci. Technol.,* 2012.

[14] Y. Inoue, M. Okamura, and K. Sato, "A thin-film semiconducting TiO_2 combined with ferroelectrics for photoassisted water decomposition," *J. Phys. Chem.,* 1985.

[15] M. B. Starr and X. Wang, "Coupling of piezoelectric effect with electrochemical processes," *Nano Energy*, 2014.

[16] H. Nishiyama, N. Rattana, N. Saito, K. Sato, and Y. Inoue, “Effects of Rayleigh surface acoustic wave upon adsorptive and surface properties of a thin NiO film,” *J. Phys. Chem. B*, 2000.

[17] H. Nishiyama, N. Saito, H. Chou, K. Sato, and Y. Inoue, “Effects of surface acoustic waves on adsorptive properties of ZnO and NiO thin films deposited on ferroelectric substrates,” *Surf. Sci.*, 1999.

[18] S.Wang, E. Mitterriter, A.Wixforht, U, Wurstbauer, C. Westerhausen, "Tunable electrochemical hydrogen evolution reaction employing SUrface Acoustic Waves." to be publishedn

[19] W. Sheng, H. A. Gasteiger, and Y. Shao-Horn, “Hydrogen Oxidation and Evolution Reaction Kinetics on Platinum: Acid vs Alkaline Electrolytes,” *J. Electrochem. Soc.*, 2010.

[20] J. Zhu *et al.*, “Boundary activated hydrogen evolution reaction on monolayer MoS_2,” *Nat. Commun.*, 2019.

[21] D. Voiry *et al.*, “Conducting MoS_2 nanosheets as catalysts for hydrogen evolution reaction,” *Nano Lett.*, 2013.

[22] J. Ferez, E. R. Gonzalez, and H. M. Villuiias, “Hydrogen evolution reaction on gold single-crystal electrodes in acid solutions,” *J. Phys. Chem. B*, 1998.

[23] Y. Xu, “The hydrogen evolution reaction on single crystal gold electrode,” *Int. J. Hydrogen Energy*, 2009.

[24] G. Lu, P. Evans, and G. Zangari, “Electrocatalytic Properties of Ni-Based Alloys Toward Hydrogen Evolution Reaction in Acid Media,” *J. Electrochem. Soc.*, 2003.

[25] V. Vij *et al.*, “Nickel-based electrocatalysts for energy-related applications: Oxygen reduction, oxygen evolution, and hydrogen evolution reactions,” *ACS Catal.*, 2017.

[26] Y. Wang et al., “Activation Effect of Electrochemical Cycling on Gold Nanoparticles towards the Hydrogen Evolution Reaction in Sulfuric Acid,” Electrochim. Acta, 2016.

[27] H. Zhang, C. Hu, S. Chen, K. Zhang, and X. Wang, “Synthesis of SnO_2 nanostructures and their application for hydrogen evolution reaction,” *Catal. Letters*, 2012.

[28] D. J. Ham, R. Ganesan, and J. S. Lee, “Tungsten carbide microsphere as an electrode for cathodic hydrogen evolution from water,” *Int. J. Hydrogen Energy*, 2008.

[29] X. Ding *et al.*, “Surface acoustic wave microfluidics,” *Lab on a Chip*. 2013.

[30] T. Dung Luong and N. Trung Nguyen, “Surface Acoustic Wave Driven Microfluidics – A Review,” *Micro Nanosyst.*, 2012.

[31] Y. Inoue, “Effects of acoustic waves-induced dynamic lattice distortion on catalytic and adsorptive properties of metal, alloy and metal oxide surfaces,” *Surface Science Reports*. 2007.

[32] S. J. Reese, D. H. Hurley, and H. W. Rollins, “Effect of surface acoustic waves on the catalytic decomposition of ethanol employing a comb transducer for ultrasonic generation,” *Ultrason. Sonochem.*, 2006.

[33] Y. Watanabe, Y. Inoue, and K. Sato, “Activation of a thin film Pd catalyst for CO and ethanol oxidation by surface acoustic waves,” *Surf. Sci.*, 1996.

[34] A. Yabe, Y. Hamate, M. Hara, H. Oguchi, S. Nagasawa, and H. Kuwano, “A self-converging atomized mist spray device using surface acoustic wave,” *Microfluid. Nanofluidics*, 2014.

Chapter 4

SAW assisted water splitting reaction

The following chapter is based in wide parts on our publication "SAW enhanced water splitting reaction with Methanol as a sacrifice material" (citation [7] in Chapter 3).

In this work, we carry out surface acoustic wave mediated catalytic reactions based on the photocatalysis of a water-methanol mixture gas by employing a catalyst chip design. A Pt modified TiO_2 thin film was deposited in the propagation path of a Rayleigh-type SAW. The effect of the surface acoustic wave on the activation of the Pt/TiO_2 catalyst in terms of water splitting was examined by an indirect but very sensitive and reliable technique: Here, the non-oxidative dehydrogenation of the alcohol in the methanol – water mixture is employed to produce formaldehyde and clean hydrogen gas. The formaldehyde being produced in this reaction in a quantity proportional to the one of the hydrogen yield is quite simply detected by a Hantzsch reaction of acetoacetanilide with formaldehyde and fluorometric measurement [1] (see below) and is used to determine the catalytic efficacy of the chip based reactor. To anticipate: Our experimental results convincingly show that the photo-dehydrogenation of methanol is clearly enhanced by applying an intense surface acoustic wave to the Pt/TiO_2 catalyst and exhibits a nonlinear relationship with the SAW power. To clarify the physical origin of the observed SAW enhancement of the catalytic efficacy, we have to consider the (i) mechanical surface deformation and (ii) the piezoelectric fields accompanying the SAW. In order to study the effect of any electric fields, we separate the catalyst layer from the piezoelectric SAW substrate by a very thin (60 nm) conductive metal film. This conductive layer is known to very efficiently attenuate the SAW induced electric fields but does not affect the SAW-induced mechanic vibration. Same photocatalysis experiments carried out again by using this metalized device-type catalyst, other than that, all experimental parameters have been kept the same as in the "mechanical plus electric field" studies. Our findings indicate that when the surface electric field is reduced, the catalysis-promoting effect of the SAW clearly decreases as compared to that with electric fields at the same SAW power.

4.1 Experimental setup

The SAW chip comprising one IDT for the generation of surface acoustic waves [2] with a resonance frequency around f=150.3MHz was fabricated using standard microlithography. The Pt modified Titanium dioxide nanoparticles serving as the photocatalyst were synthesized as described below, and then deposited within the propagation path of the surface acoustic wave by a simple spin coating method.

The gas-phase catalytic reaction takes place in a flow-type reactor cell, in which a tiny ($1cm^3$) cylindrical chamber with a quartz window on top was in direct contact with the $LiNbO_3$ sample and the Pt/TiO_2 catalyst. A UV light emitting diode (λ=365nm) was placed above the reactor cell, and its irradiation intensity is P_{LED} = $85mW/cm^2$ which was determined by a power meter (Thorlabs PM100A). In figure 4.1, a schematic of our setup is depicted.

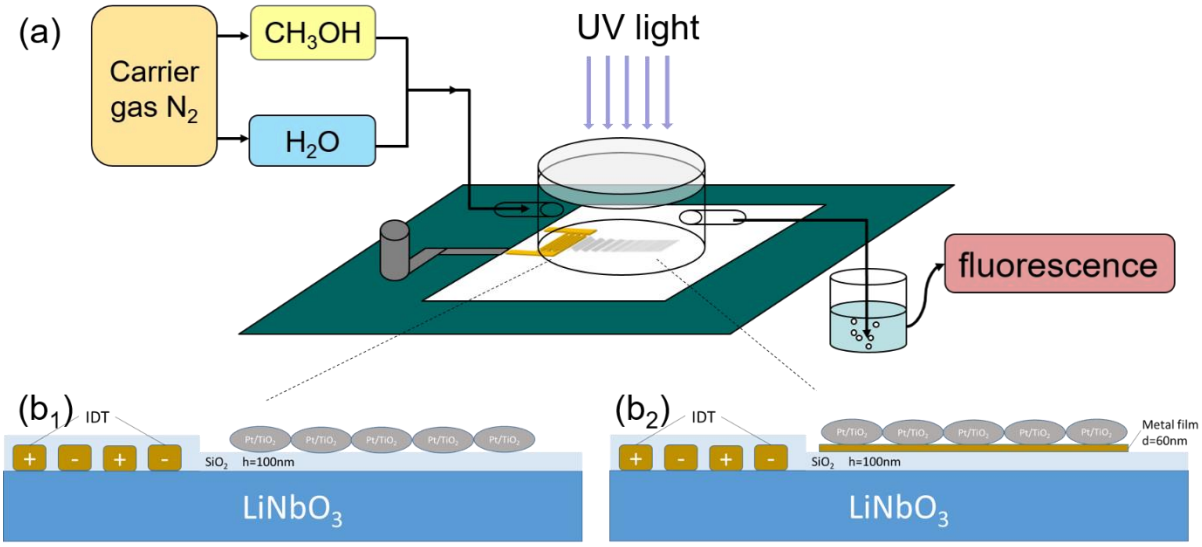

Fig. 4.1 (a) Setup: The green part represents a circuit board which holds an rf connector, the SAW chip with the catalyst layer in the propagation path of a surface acoustic wave and the micro reaction chamber. Through a quartz glass window on top of the cylinder the sample is illuminated with UV radiation. The reaction chamber has a gas inlet and a gas outlet. The inlet contains nitrogen, water and methanol vapor, and the outlet contains nitrogen, water and methanol vapor as well as eventually produced formaldehyde serving as an indicator for the hardly detectable H_2. Picture (b_1) represents the SAW-based Pt/TiO_2 catalyst device without metal layer, and (b_2) represents the SAW-based Pt/TiO_2 catalyst device with metal layer.

This SAW based catalyst was used for the methanol photodehydrogenation reaction for measurements with and without the assistance of our Rayleigh type surface acoustic waves. The influence of the SAW onto the catalytic efficiency was checked by determining the amount

of formaldehyde being produced. In order to find out the influence of the SAW-generated electric field, we also performed experiments with a thin metal film between the catalyst and the piezoelectric SAW substrate. Apart from this field shortening film, in both sets of experiments all parameters remained the same such that we could determine any effect of the SAW accompanying electric fields.

4.1.1 Synthesis of Pt modified TiO_2 nanoparticle

To synthesize the Pt modified TiO_2 nanoparticle, we deposited Platinum nanoparticles on the surface of TiO_2 powder by a reduction method [3]. The TiO_2 powder [Degussa (P25, anatase 78%)] was used without any pretreatment. 30mg TiO_2 was suspended in 5mL, 0.4M H_2PtCl_6 solution and then stirred vigorously for 8 hours at room temperature. Thereafter, 5mg $NaBH_4$ was gradually added to the slur. After sufficient stirring, the suspension was centrifuged and washed with pure water for 3 times. Afterwards, the sediment was dried and we put 20mg produced Pt/TiO_2 into 1mL ethanol to obtain the suspension used for spin coating. All the chemicals were purchased from Sigma Aldrich. Finally, the synthesized Pt/TiO_2 was inspected in a scanning electron microscope (SEM) to check their morphology as shown in Fig. 4.2.

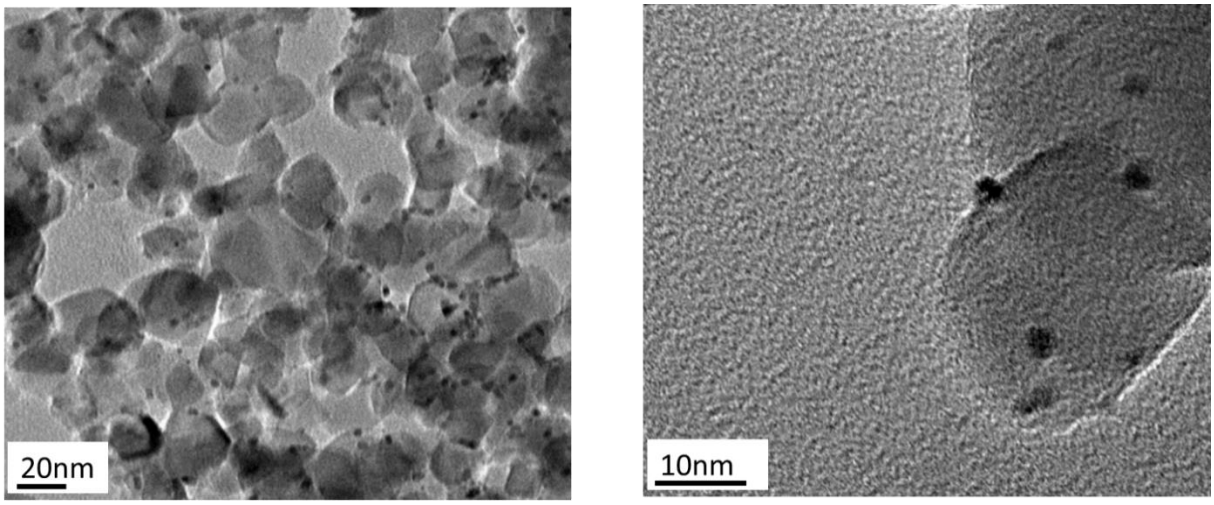

Fig. 4.2 SEM of synthesized Pt/TiO_2 catalyst.

The two SEM pictures in Fig. 4.2 illustrate that the diameter of TiO_2 (P25) nanoparticle was around 20nm and the size of Pt nanoparticle was around 1nm in diameter, with the latter nanoparticles located on the surface of TiO_2.

4.1.2 IDT fabrication and spin coating of the Pt/TiO_2 film

For the SAW chips, we used 128° rotated Y-cut $LiNbO_3$ single crystal substrates, on which Rayleigh type SAW are generated. The size of the $LiNbO_3$ chips is 17.5mm×17.5mm and the chip thickness is 0.5mm. The designed IDT had an aperture of W=2mm and a finger spacing of d=6.25μm, which results in a SAW wavelength of λ=25 μm. The IDT employed had 16 finger pairs. These IDT were micro lithographically fabricated near the short sides of the substrate, and consisted of 5nm Ti on the bottom, then 50nm Au and 5nm Ti on the top. Lastly, a h=100nm thick SiO_2 layer was deposited on top of the whole $LiNbO_3$ substrate by thermal evaporation, serving as a protection film. After fabrication, the resonance frequency of the IDT delay line was determined by a vector network analyzer (Rohde & Schwarz).

To finalize the SAW assisted catalysis samples, we spin coated (1500rpm for 5 seconds) 8μL Pt/TiO_2-ethanol suspension of the Pt/TiO_2 catalyst directly onto the propagation path of the $LiNbO_3$ SAW delay lines. Then, this coated substrate was baked at T=80°C for 5min to evaporate all ethanol. Finally, any accidentally deposited catalyst layer outside the SAW propagation path was carefully removed to ensure that all the present catalyst particles are influenced by the SAW. This resulted in an active catalyst area of around 2mm×8mm. The morphology of the films was measured by atom force microscopy and the thickness of the film was checked by a Dektak© profilometer. The results of both are presented in Fig. 4.3(a) and (b).

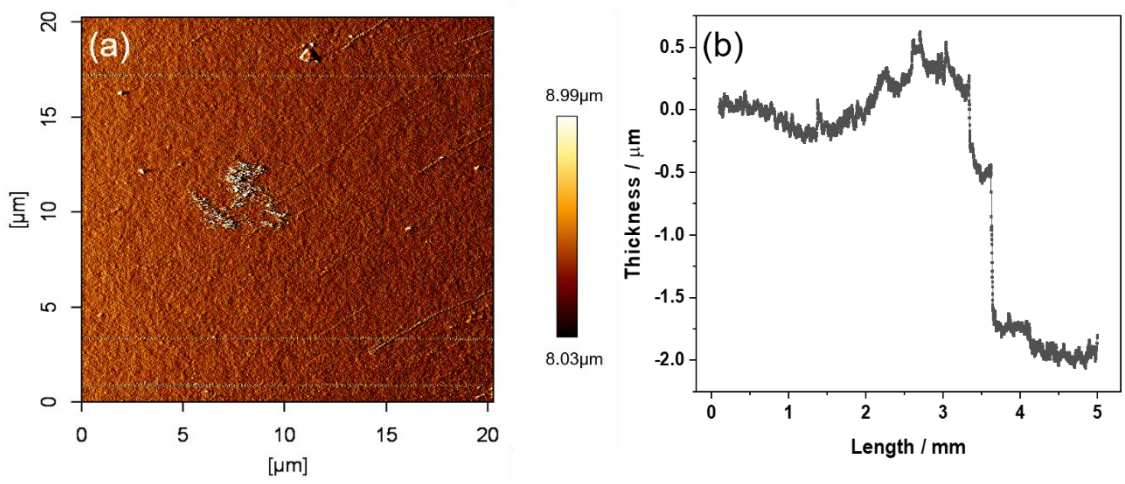

Fig. 4.3 (a) is the AFM picture of spin-coated Pt/TiO_2 catalyst film. (b) is the Dektak© profilometer measurement for the thickness of the catalyst film.

The AFM figure 4.3(a) shows that the roughness of the spin-coated catalyst film is relatively low. Fig. 4.3(b) shows the Dektak© measurement for the determination of the thickness of the

catalyst film. Here the positions 0 to 3.5mm represents the area of the catalyst film, and 3.5mm to 5mm is the area of substrate. We find that the thickness of the film is around 2μm, which is much less than the SAW wavelength (25μm). Moreover, this indicates that even though catalysts were deposited on the delay line of SAW chip, they should not cause any change in the SAW phase velocity. To check this, and that no other type of acoustic wave is excited, the following transmission measurements were taken.

4.1.3 S_{21} transmission signal

To characterize the SAW chip and to check whether the thin catalyst layer possibly alters the SAW propagation mode, we manufactured two otherwise nominally identical SAW delay lines with and without the thin catalyst layer and compared their rf transmission functions employing a network analyzer. We measured the S_{21} transmission in the time domain (from 0 to 0.6μsec) as a function of frequency from 50MHz to 800MHz. This way, we are able to distinguish different acoustic modes quite easily. The result is shown in Fig. 4.4.

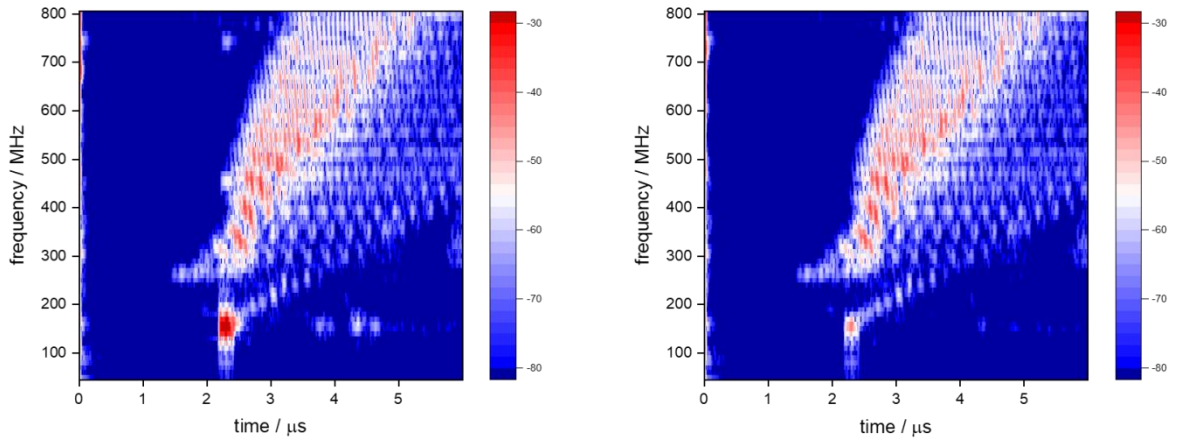

Fig. 4.4 S_{21} at different frequencies in time domain, the left graph shows the experiment with no catalyst deposited on the delay line and the right graph shows the experiment when catalyst was deposited on the delay line. The right bar shows the scale of the S_{21} signal in dB.

Basically, two acoustic modes and a few echoes are seen in Fig. 4.4: The one with the largest signal (red) at f=150.3MHz and Δt = 2.3μsec represents the Rayleigh SAW, since the velocity of the surface acoustic wave is 3980m/s and the length of delay line is 8.7mm, so the propagation time of surface acoustic wave from one IDT to another IDT is around 2.3μs. In the left picture, where no catalyst is present on the delay line, the S_{21} signal at 150.3MHz 2.3μs is stronger than the S_{21} signal in right picture at same frequency and same time. This is because

the elastic andelectric properties of the TiO_2 catalyst film will attenuate the S_{21} signal. The other S_{21} signal above 280MHz which exhibits a large slope results from bulk waves, these bulk wave are excited from the transducers directly. Comparing these two pictures, we can see that except a little attenuation (around 10dB) at the resonance frequency 150.3MHz and $\Delta t = 2.3\mu s$, there is no other obvious difference between the left picture and right one. This indicates that when catalyst film is located on delay line, it most likely does not generate any other type of acoustic wave. When the power was applied to the IDT, a certain high percentage thereof will convert into a surface acoustic wave with most of the acoustic energy being confined to the surface of $LiNbO_3$ and being able to interact and affect the combined catalyst film. The area of the nanoparticle film was kept around 2mm×8mm, and even though the catalyst causes attenuation, the surface acoustic wave could still pass through the whole catalyst film and reach the opposite IDT. This also demonstrates that the whole catalyst film was affected by SAW.

4.2 Determination of the amo2unt of produced formaldehyde

At the beginning of the photocatalytic reaction step, the methanol first becomes strongly adsorbed at the surface of TiO_2 to form methoxy species, and then the methoxy species directly react with the light-induced holes and are decomposed as follows [4]:

$$CH_3O^-(ad) + h^+ \rightarrow CH_3O\cdot(a) \quad (4.1)$$

$$CH_3O\cdot(a) \rightarrow CH_2O^{\cdot -}(a) + H^+ \quad (4.2)$$

$$CH_2O^{\cdot -}(a) \rightarrow CH_2O(a) + e^- \quad (4.3)$$

However, the flow-conditions and the extremely small amount of catalyst prevents further oxidation of the formaldehyde, so it is assumed that the formaldehyde is the main product in the photodehydrogenation of the methanol. On the other hand, the water gas acts as an electron consumer, and reacts with the Pt-trapped photo-generated electrons to form hydrogen gas [5].

$$H^+(a) + {e_{tr}}^- \rightarrow \frac{1}{2}H_2(g) \quad (4.4)$$

By measuring the amount of photocatalytically produced formaldehyde, being proportional to the amount of H_2 produced in the catalytic water splitting process, information about the efficiency of the SAW assisted photocatalytic activity of Pt/TiO_2 can be obtained. The quantity of the produced formaldehyde is determined by a Hantzsch reaction of acetoacetanilide (AAA) with formaldehyde which involves a cyclization between AAA and formaldehyde in the presence of ammonia so that it will produce a yellow dihydropyridine derivative product which

in turn can be detected in a fluorometric measurement with λ=370nm excitation [1]. This method is very simple and sensitive, and allows the measurement of formaldehyde at the μmol·L^{-1} level. In addition, the Hantzsch reaction can take place at room temperature without any heating system.

For calibration purposes, a series of formaldehyde standard solution was prepared having concentrations of 0, 0.856 μmol·l^{-1}, 1.712 μmol·l^{-1}, and 2.569 μmol·l^{-1}. After having 30 minutes Hantzsch reaction, they were spectroscopically measured at room temperature, which allows for the preparation of the calibration graph. Typical raw fluorescence emission data and the calibration graph are shown in Fig. 4.5. Fig. 4.5(a) illustrates that the emission intensity at 472nm responds linearly to the HCHO concentrations, in a range of 0 - 2.5 μmol·l^{-1}, and according to Li's work, the lowest determined level is 0.1 μmol·l^{-1} [1]. Fig. 4.5(b) shows the nice correlation between formaldehyde concentration and fluorescence intensity, the linear regression line was $y = 17630.8x + 41771.9$ with a correlation coefficient value of 0.9974. The x axis indicates the HCHO concentration in μmol·l^{-1}, and the y axis indicates fluorescence intensity. The obtained calibration graph can be used to calculate the amount of produced formaldehyde during the above described photocatalytic process.

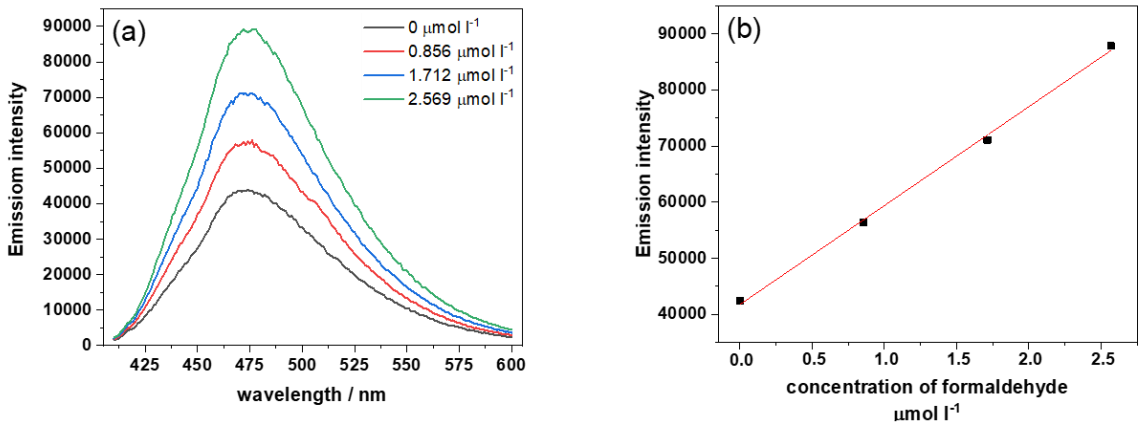

Fig. 4.5 (a) fluorescence emission intensity of standard formaldehyde solutions with different concentrations, (b) calibration graph of the raw data shown in (a).

4.3 Photocatalytic reaction with assistance of 40mW SAW

To actually determine the efficiency of the Hydrogen production in our experiments, Nitrogen was used as carrier gas and passed through liquid water and methanol at flow rates of 4.8mL/min and 0.2mL/min, respectively. Then, this mixture gas passed through the photocatalytic reaction cell. Before the experiment, the nitrogen-water-methanol mixture vapor passed through the reaction cell for one day to reach anaerobic conditions, then it bubbled in an adsorption solution for 30 minutes, and its fluorescence represents the base line for the subsequent "active" measurements with UV LED and SAW for 60 min (f_{SAW} = 150MHz and P_{SAW} = 40mW). During the SAW-assisted-photocatalytical process, every 30 min, the adsorption solution was exchanged by a fresh one and the fluorescence emission of the previous adsorption solution was checked immediately to determine the amount of formaldehyde produced.

For comparison, reference experiments were also carried out with UV illumination only (no SAW) to be able to investigate the effect of the SAW on the photocatalytic efficiency. The results are displayed in Fig. 4.6(a), (b) and (c). Clearly, a positive effect of the additional SAW interaction can be seen.

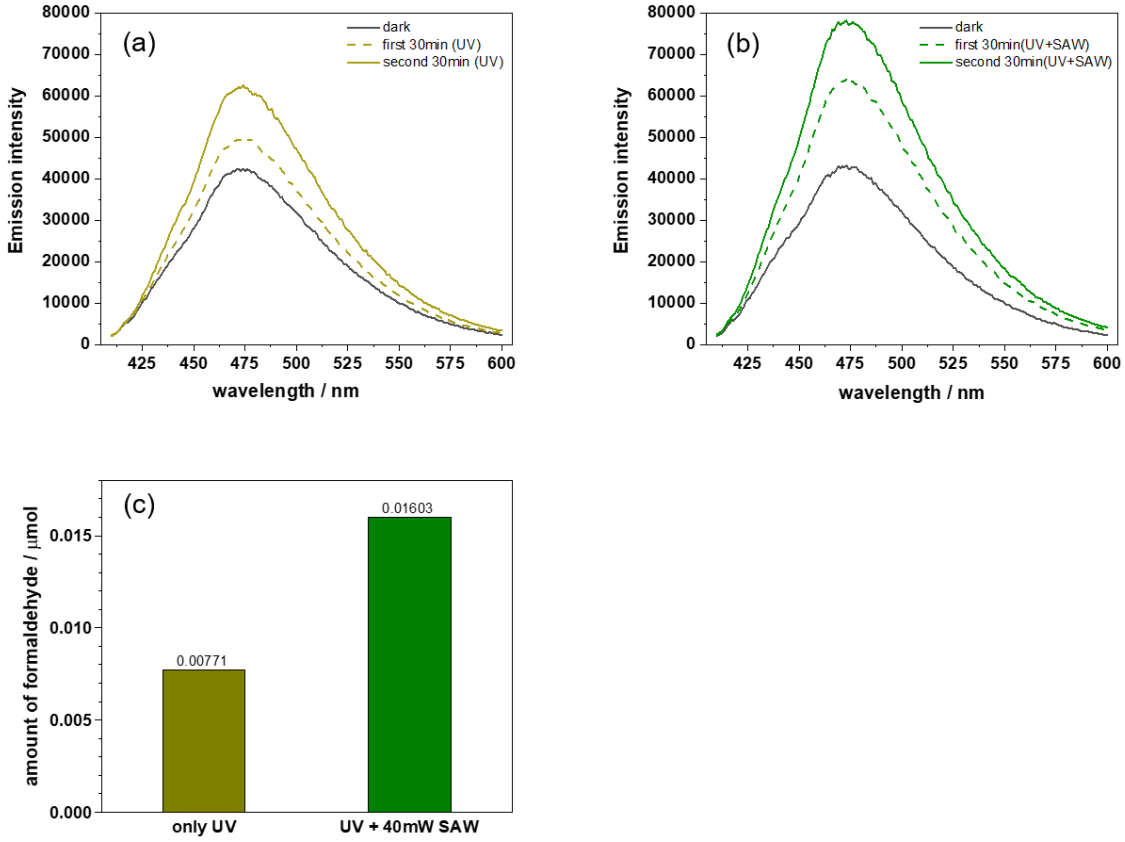

Fig. 4.6 Picture (a) is fluorescence emission intensity of the adsorption solution after 30minutes in the dark (black line), after first 30minutes UV illumination + no SAW (yellow dashed line), and another 30minutes UV illumination + no SAW (yellow compact line); Picture (b) is the same experiment as being depicted in the left panel but with SAW on at P_{SAW} = 40mW. Picture (c) shows the amount of formaldehyde being produced during the photocatalytic processes for UV illumination only and UV illumination plus P_{SAW} = 40mW surface acoustic waves. We observe a nearly 100% increase of the production efficiency under SAW interaction.

As can be seen from the figure, the additional effect of the P_{SAW} = 40mW surface acoustic wave results in a clear increase of the fluorescence emission intensity after t=30 min and t= 60 min, respectively, whereas the fluorescence intensities in the dark are almost the same. Based on our calibration data as being depicted in Fig. 4.5, we can now determine the amount of formaldehyde being produced during the reaction. The data presented in Fig. 4.6(c) illustrate that the amount of the produced formaldehyde is about 0.008µmol after 1 hour UV illumination, and doubles to 0.016µmol when a SAW is acting additionally upon the photocatalyst. The total amount of produced formaldehyde is very small, but on the other hand the active area of the catalyst film was only 2mm×8mm.

4.4 Influence of temperature

One might argue that the increase in formaldehyde production, indicating H_2 production in the photocatalytic process is due to an increased reaction temperature while the SAW is present, and the temperature is also critical for the resonance frequency of the IDT. Thus, temperature variation and shifts of the resonance frequency were investigated experimentally. A homemade tiny temperature sensor was attached to the cylinder reaction chamber. Silver glue was used to fill the gap between the sensor and the chamber. The temperature was recorded during the whole two photocatalytic reaction processes, 30 min in dark and 60 min under UV illumination, while one only took place under UV illumination and the other one is under both UV illumination and the SAW with P_{SAW}=40mW. The temperature change is shown in Fig. 4.7 and the resonance frequency shift and calculated output SAW energy at 150.3MHz is illustrated in Table. 4.1.

Here in Fig. 4.7, we depict the temperature change as a function of time. From 0 to 30 minutes, the UV light was turned off, so the recorded temperature is around room temperature (22.5°C). From 30 minutes to 60 minutes, the UV illumination and the SAW have been turned on, and the temperature increased immediately. As can be seen, both curves (UV only and UV plus SAW) are basically the same, and the total temperature increases by about 20°C during the experiment, and it obviously mainly caused by the UV illumination, the 40mW SAW cause a negligible additional temperature rise. Thus, it is safe to state that the SAW, which clearly produces a doubling in the catalytic efficiency, does not act via an additional temperature increase but rather via intrinsic SAW related effects.

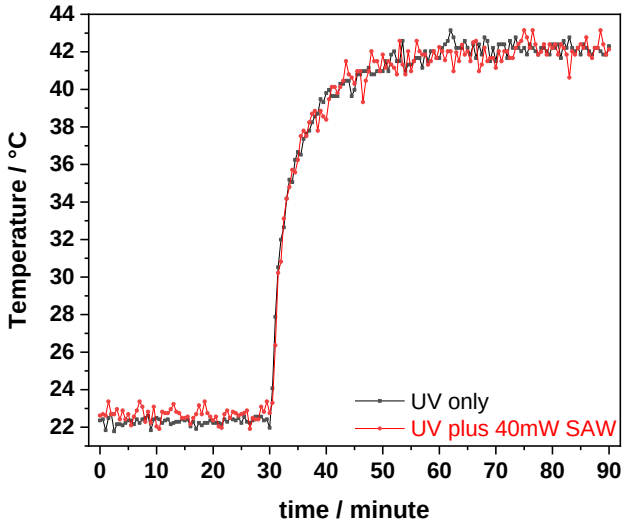

Fig. 4.7 Temperature change during the photocatalytical reaction process. From 0 to 30minutes, the UV light was off, then the UV illumination was turned on from 30 minutes to 60 minutes. the temperature increase has been measured (black trace). For comparison, the exact same experiment was performed but with the P_{SAW} = 40mW acoustic wave been turned on (red trace). The traces for SAW off and SAW on are basically identical, indicating that the SAW does not alter the temperature during the experiment. The overall increase is thus mainly caused by the UV illumination.

To estimate the effect of the changing temperature on the SAW resonance frequency $f_{SAW} = v_{SAW} / \lambda_{SAW}$ during the experiment, we separately measured the SAW resonance frequency as a function of temperature, using a network analyzer (see Table 4.1). As v_{SAW} is known to be temperature dependent, we also expect f_{SAW} to change during the course of the experiment.

Table. 4.1 SAW resonance frequency due to the temperature change during the photocatalytic experiment

time	temperature	Measured resonance frequency	S_{11} at 150.34 MHz	Output SAW power/ input power
After 30min in dark	22.5 °C	150.34 MHz	-8.98 dB	87.35%
After 30min under UV	41.1 °C	150.16 MHz	-8.94 dB	87.24%
After 60min under UV	42.3 °C	150.11 MHz	-8.92 dB	87.18%

The temperature coefficient for 128° rotated y-cut $LiNbO_3$ is 76ppm/°C [6]. Thus, we expect a change of f_{SAW} by about Δf_{SAW}=11.4KHz for every degree of temperature change. In Table. 4.1, we can see that the temperature increase after one hour's illumination turned out to be almost ΔT =20 °C (see also Fig. 4.7), and the resonance frequency shifted by Δf_{SAW} = -0.24MHz which nicely agrees with the expected value. During the experiment and over 1hour illumination time, however, we kept the output frequency of the rf generator constant at 150.3MHz. This in turn is equivalent to a slight change of the SAW power, being caused by the temperature induced shift of f_{SAW}. This slight decrease of the SAW power can be estimated once the frequency dependent transmission function S_{12} or the power reflection S_{11} of the IDT is known. In Fig. 4.8, we show the measured S_{11} of the emitting IDT as a function of frequency. As we can see, the temperature dependent Δf_{SAW} = -0.24MHz would result in only a very small power change which is estimated to be less than 0.1 dB for the for ΔT= +20° being caused by the UV illumination. Hence, the observed nearly 100% increase of the catalytic efficiency due to SAW interaction might even be a bit larger, taking the non-compensated shift of the SAW resonance frequency into account

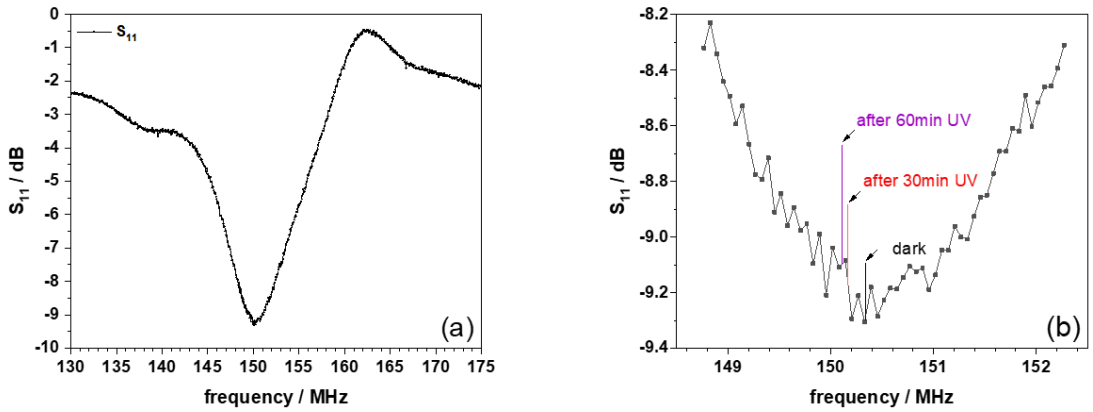

Fig. 4.8 (a) return loss S_{11} as function of frequency, measures by a network analyzer at room temperature, and (b) Zoom-in of (a) with indicated resonance frequencies before and after 30 and 60 min UV illumination, respectively.

4.5 Acoustic-photocatalysis and its dependence on the SAW power

On the purpose to study relationship between the SAW power and enhancement of photocatalytic reaction, photodehydrogenation of methanol was carried out for different SAW power levels, 10mW, 20mW, 30mW and 40mW separately. The Pt/TiO_2 catalyst was ewfreshed after each experiment. Here the activation coefficient was used to indicate the effect of SAW to the photocatalytic reaction. The activation coefficient was defined as $AC = M_{SAW+UV} / M_{UV}$, M_{SAW+UV} is the yield amount of formaldehyde when a SAW was applied during UV illumination, and M_{UV} is the yield amount of formaldehyde when SAW was not applied during UV illumination. The result is shown in Fig. 4.9.

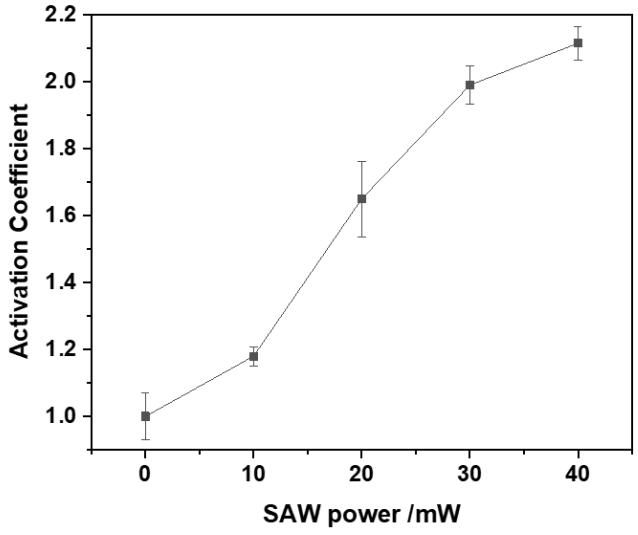

Fig. 4.9 Activation coefficient (as being defined in the text) for various SAW power levels $\mathbf{P}_{SAW}$ = 0mW, 10mW, 20mW, 30mW and P_{SAW} = 40mW. At least for our experimental f_{SAW} = 150.3MHz, the activation coefficient seems to first strongly increase and then to saturate for P_{SAW} >30mW.

Now that it has been unambiguously shown, that the SAW increases the catalytic reaction efficiency of our assay by a non-temperature related effect, we can state that the activation coefficient seems to first strongly increase and then to saturate for P_{SAW} >30mW. The increasing activation coefficient AC indicates a SAW-enhanced photocatalytic activity of Pt/TiO_2. In this experiment, the SAW propagate at the surface of $LiNbO_3$. This wave can cause well-defined displacements at the surface of the substrate, and these mechanical displacements are accompanied by electric fields and an electric potential because the distorted substrate is a piezoelectric material. The spatial and temporal changed positive and negative surface polarization hence leads to strong electric field near the surface. The SAW induced electric potential ($\emptyset$) is related to the square root of the power level of the SAW according to the equation (4.5), the SAW induced electric field and amplitude of the mechanic vibration are both related to the SAW induced electric potential according to the equation (4.6) and (4.7) [7].

$$\text{Potential:} \qquad P_{SAW} = \frac{1}{2}\frac{A}{\lambda} y_0 |\emptyset|^2 \tag{4.5}$$

here, A is beam width of the SAW, λ is the wavelength and y_0 a material dependent constant ($y_{0,LiNbO_3}(128°) = 0.21mS$) [7].

$$\text{Electric field:} \qquad E_x = -\frac{\partial \emptyset}{\partial x} = jk\emptyset, \qquad E_y = -\frac{\partial \emptyset}{\partial y} = 0, \qquad E_z = -\frac{\partial \emptyset}{\partial z} \tag{4.6}$$

here, E_x and E_y are SAW-induced in-plane electric field, and x is SAW propagation direction. E_z is the out-of-plane electric field, and z direction is perpendicular to the surface of substrate. Since the SAW is travelling along the x direction, $\partial/\partial x$ can be represented by j·k, here k is the wave vector. The in-plane electric field E_y is always zero because the SAW is in good approximation a plane travelling wave and is uniform in y direction. $\partial/\partial z$ can be represented as a sum of the decaying exponentials because the SAW decays underneath the surface of substrate.

The displacements at the surface are also related to the surface potential $\emptyset$ through the constants c_x, c_y and c_z.

$$\text{Mechanical vibration:} \qquad u_x = c_x \cdot \emptyset, \qquad u_y = c_y \cdot \emptyset, \qquad u_z = c_z \cdot \emptyset \tag{4.7}$$

here, u_x is the displacement along x direction, u_y is the displacement along y direction and u_z is the displacement along z direction.

Equations (4.5), (4.6) and (4.7) indicate that the SAW-induced surface potential, the electric field and the mechanical vibration are positively related to square root of the SAW power level. When the SAW power increases, these SAW-induced accompanying parameters will also increase. This gives rise to the interpretation that the SAW-induced surface deformations, electric fields and the electric potential could be the reason for the SAW power depended catalytic activity.

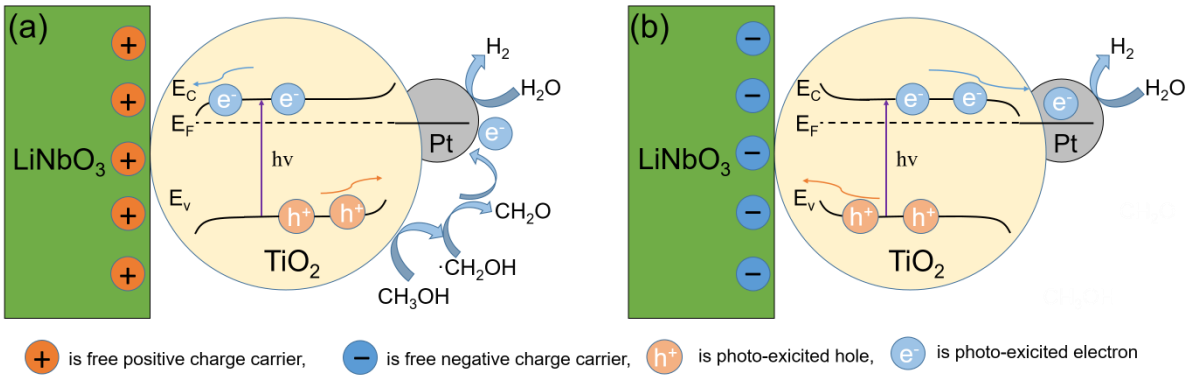

Fig. 4.10 Schematic energy level diagrams of TiO_2 under (a) negative polarization and (b) positive polarization normal to the $LiNbO_3/TiO_2$ interface. E_C represents the conduction band edge, E_V represents the valence band edge of the TiO_2, and E_F represents the fermi energy of TiO_2.

The SAW-induced electric field could directly affect the band structure of TiO_2. As we know, TiO_2 is a semiconductor catalyst, which has a well-defined conduction band and a valence band. When it is under the influence of a strong enough electric field, this external electric field could cause a certain band bending of the TiO_2. The SAW, being responsible for a dynamic poling of the $LiNbO_3$ substrate, also couples electric fields into the Pt/TiO_2 nanoparticles where it induces a dynamical band bending and the formation of depletion and accumulation layers in the TiO_2. To illustrate this idea, we sketch in Fig. 4.10(a) and (b) the schematic energy level diagrams under both negative and positive polarization. On positive poled $LiNbO_3$, there are many positive polarization charges at the interface of $LiNbO_3$, which causes a drift of the negative free charge carriers in the TiO_2 toward the interface to compensate the positive polarization, these redundant negative free charge carriers cause a negative charged depletion layer, and lead to downward band bending. Positive free charge carriers, on the other hand, move into the opposite direction, namely the interface between TiO_2 and gas phase, these positive free charge carriers cause a positive charged depletion layer there, and lead to upward band bending. As a

result, the SAW-induced external electric field lead to an internal electric field at the interface of $LiNbO_3/TiO_2$ and the interface of TiO_2/gas. There, under UV light illumination, electrons are excited from the valence band of TiO_2 to the conduction band of TiO_2, and leave holes in the valence band. The photoexcited electron-hole pairs can be separated by the external SAW-induced electric filed, the photoexcited electrons in the TiO_2 move toward the $LiNbO_3/TiO_2$ interface while the photoexcited holes drift towards the TiO_2/gas interface. Moreover, the upward-bent band at the TiO_2/gas interface tend to accumulate holes at the interface, then these holes take part in the oxidation reaction. Both the CH_3OH and the H_2O will interact with these holes. Methanol always serves as hole scavenger, and transient spectroscopic studies have revealed that the reaction of CH_3OH and the hole happens at a much faster rate than the one for the H_2O molecules and holes [3]. Here, the methanol does not only serve as hole scavenger, as a hydrogen-containing sacrificing material, it also contributes its hydrogen atom to produce hydrogen gas. The chemical reaction (4.1) produced $\cdot CH_2OH$ radical is an excellent electron donor [8], which dissociates a proton (reaction (4.2)) and injects its electron (reaction (4.3)) to the conduction band of TiO_2, which is called "doubling effect" [9,10]. The injected electron prefers to aggregate on the Pt nanoparticle being located at the surface of TiO_2, and it reduces the dissociated proton into hydrogen gas. Here, the Pt nanoparticle acts as an active site for the reduction reaction to produce hydrogen gas, because it can capture photogenerated electrons, and also lowers the overpotential for hydrogen production [3].

For a temporary negative poled $LiNbO_3$, the positive free charge carriers in TiO_2 will move toward the interface of $LiNbO_3/TiO_2$ and lead to upward band bending, at the same time, the negative free charge carrier in TiO_2 will drift to the interface of TiO_2/gas and lead to downward band bending. The photoexcited electron-hole pairs are subsequently spatially separated by the electric field travelling with the SAW and are driven into opposite directions, the photoexcited electrons drift to the interface of TiO_2/gas, and the downward band bending help the electrons to transfer firstly to Pt nanoparticle and then take part in the reduction reaction to produce hydrogen gas. This SAW-induced electric field and caused band bending quite efficiently prevents electrons and hole recombination and leads to longer lifetimes of these charge carriers, which in turn strongly promotes the photocatalytic reaction.

On the other hand, the SAW-induced mechanical vibration could also accelerate the chemical reaction by reducing the strain depended diffusion barrier of the reactant. For a heterogeneous

catalysis process, the reactant is firstly adsorbed on the catalyst's surface and then diffuses to the active site of the catalyst. Then, the chemical reaction can take place on the active site and the adsorbed reactant changes into the product. Some detailed analysis of the SAW promoted activation at atomic-level in surface catalytic process are done by Wu et al. and his theoretical and computational investigations illustrate that the action of Rayleigh acoustic waves could enhance the surface diffusion of adsorbed atom by tens and hundreds percent [11], which could also positively affect the activity of the catalyst.

4.6 Separation of the mechanical and electric contribution to the SAW effect on catalysis

In order to further elucidate the physical mechanism behind the observed beneficial interaction mechanism of a SAW, enhancing the efficiency of the photocatalytic reaction, we have fabricated a modified chip which was then used in the same reaction as described before. The modification consists of a simple metallization (5nmTi+50nmAu+5nmTi) of the SAW propagation path before we deposit the catalyst film in the usual manner. This metallization has no significant influence on the mechanical deformation of the chip surface, because the thickness of the metal (60nm) is much less than the wavelength of the SAW (25μm), but it can completely alter the electrical boundary conditions at the surface. A (thin and massless) conductive layer on the surface of a SAW substrate, however, efficiently shortens the piezoelectric fields accompanying the SAW and also renormalizes the SAW velocity [12] to a somewhat lower (Δv) value as compared to the open, non-metallized surface (v_0). The renormalization is parametrized in the so-called electromechanical coupling coefficient $K_{eff}^2 = 2\Delta v/v_0$. The SAW-induced electric potential for the open surface and the metalized surface are simulated using COMSOL software and shown in Fig. 4.11(a) and (b) separately.

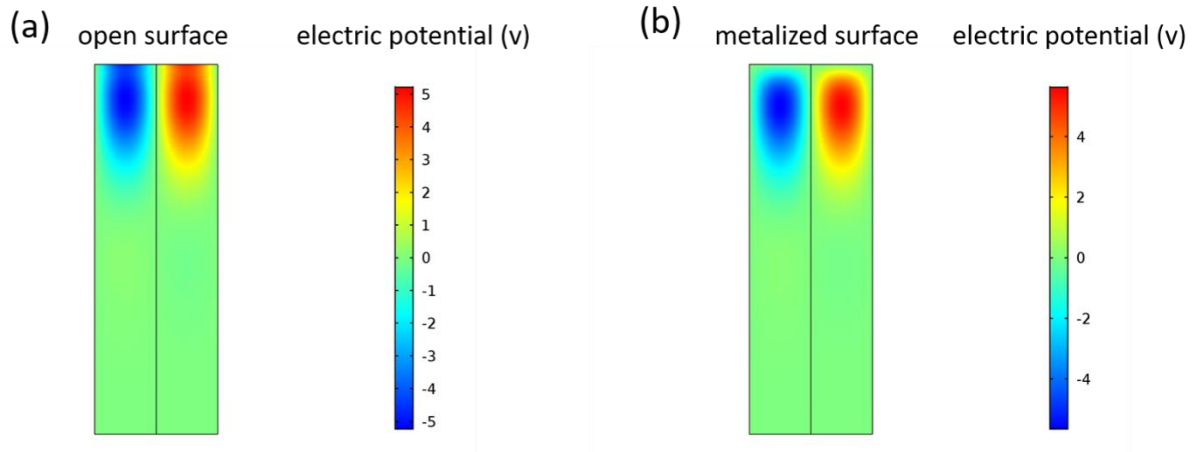

Fig. 11: COMSOL simulated electric potentials within a SAW substrate. We depict it from a side view of 128° y-cut $LiNbO_3$. The width of the $LiNbO_3$ slab in our calculation is 25µm (one wavelength) and the height is 75µm. The propagation direction of the wave is along the width of the rectangle. The surface of the $LiNbO_3$ substrate, where SAW propagate is at the top of the rectangle. (a) depicts the simulated electric potential when the surface is free, and (b) shows the simulated electric potential when surface is covered with a thin, massless metal film.

In order to study the mechanism of how the SAW related electric fields affect the photocatalytic reaction, the exact same photocatalytic reaction was carried out again at the SAW resonance frequency by using the Pt/TiO_2 catalyst but now with a thin metal film between the catalyst and the SAW substrate. To study the power dependence of the activation coefficient, different SAW Powers P_{SAW}= 10mW, 20mW, 30mW and 40mW SAW were applied separately during 1 hour UV illumination. The activation coefficients AC_1 for the normal SAW chip (open surface) and AC_2 for the metallized SAW chip are compared in Fig. 4.12.

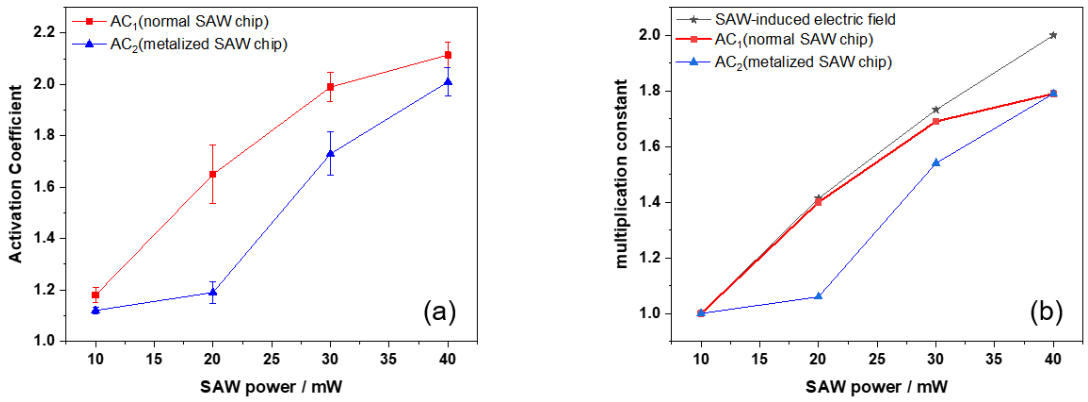

Fig. 4.12 (a) coefficient AC_1 and AC_2 under various SAW power, where the P_{SAW} = 10mW, 20mW, 30mW and 40mW separately. Resonance frequency was kept at f_{SAW} = 150.3MHz. (b) the multiplication constant for SAW-induced electric field (E_{field}), AC_1 and AC_2 under various SAW power, The SAW-induced electric fields (E_{field}) are normalized by the E_{field} which is produced by the P_{SAW}=10mW SAW, so the multiplication constant for

P_{SAW}=10mW, 20mW, 30mW and 40mW SAW-induced E_{field} are 1, $\sqrt{2}$, $\sqrt{3}$, and 2 respectively. Using the same method, all the AC_1(normal SAW chip) values were also normalized to AC_1 at P_{SAW}=10mW, and all AC_2(metalized SAW chip) values were normalized to the AC_2 for a P_{SAW}=10mW SAW.

We can clearly see that the value of AC_1(normal SAW chip) and AC_2(metalized SAW chip) both exceed unity, when P_{SAW} = 10mW, 20mW, 30mW and 40mW SAW is applied. This experimental finding in fact reveals that obviously both the "metal film modified" SAW chip and the non-metalized "normal" SAW chip enhance the catalytic activity of Pt/TiO_2. At the same SAW power, however, the AC_2 (metalized SAW chip) are always smaller than the AC_1 (normal SAW chip), this indicates that the obvious SAW-promoted catalytic efficiency was somewhat weakened by the 60nm metal film. The metal film cancels the SAW-generated electric potential at the surface ($\emptyset = 0$), and it short circuits the in-plane electric field E_x and E_y, which are parallel to the surface of substrate. The out-of-plane electric field E_z, which is perpendicular to the surface, is strongly reduced. In terms of mechanical vibrations, metalization is not a prominent factor, since the thickness of metal film (60nm) is much smaller than SAW wavelength (25μm) and the mass loading of such a thin film is negligible [13]. Hence, the metalized SAW chip and normal SAW chip basically provide the same mechanical vibration at the same SAW power. As a result, we consider the reason for the smaller AC_2 (metalized SAW chip) as compared to AC_1 (normal SAW chip) to be the SAW-induced electric field (E_{field}) although being reduced by the metal film. The reduced electric filed values, however, cannot cause a significant band bending of TiO_2. Moreover, these photo-excited electrons and holes will not be efficiently separated by the small external SAW induced electric field (E_{field}) and most of them have a chance to recombine, thus these photocatalytic reactions are not so significantly promoted as we observe it in the experiment for the normal chip.

For the normal SAW chip, AC_1 at P_{SAW} = 10mW was AC_1=1.18, and it was AC_1=1.65 at P_{SAW} = 20mW, which is 1.4 times bigger. However, for the metalized SAW chip, AC_2 at P_{SAW} = 20mW was AC_2=1.19 and thus only 1.06 times bigger than the AC_2 at P_{SAW} = 10mW. When the power of SAW is doubled from P_{SAW} = 10mW to 20mW, the SAW-induced mechanical vibration and electric field will become $\sqrt{2}$ times stronger, according to equations (4.5), (4.6) and (4.7). We know that the metal film causes only a negligible attenuation of the mechanical vibrations, so they should be increased from P_{SAW} = 10mW to P_{SAW} = 20mW by the same factor for both the normal SAW chip and the metalized SAW chip. However, we observe a significantly larger SAW mediated increase for AC_1 (normal SAW chip) but not for

AC_2(metalized SAW chip), so we take this fact as a signature to be safe to exclude the SAW-induced mechanical vibration as the main reason for SAW-promoted catalytic property. Again, in terms of SAW-induced electric fields (Ex, Ey and Ez), due to the shortcut and attenuation effect of the metal film, the in-plane electric field Ex=0 and Ey=0, the out-of-plane electric field Ez(metalized SAW chip) is smaller than the Ez (normal SAW chip). Therefore, this weaker electric field might not efficiently separate the electron-hole pair and prolong their lifetime, which might be the reason for the low AC_2 value under the influence of the P_{SAW} = 20mW SAW.

In Fig. 4.12(b), it is obvious that the multiplication constant of AC_1(normal SAW chip) is almost constant with the multiplication of the SAW-induced electric field when the applied SAW power is between 10mW to 30mW. As has been analyzed above, the SAW-induced electric field (E_{field}) is the main reason the promotion of catalytic activity, so E_{field} and AC_1 have the same rising tendency. However, the tendency deviates when the SAW power exceed P=30mW, the increase of AC_1 is lower than the increase of the SAW-induced E_{field}, the reason of which might be the further oxidation of formaldehyde. Even though the reaction rate of CH_3OH and the photoexcited hole is faster than the one for the H_2O molecules and holes, some hole will still inevitably react with H_2O molecule and oxidize it into free ·OH radical, and due to its strong oxidizing properties, the free ·OH radical could further oxidize formaldehyde into HCOOH or CO_2 [14]. Under the condition of big SAW power, the SAW-induced electric field will become stronger and this can help to separate photoexcited electron-hole pairs and hinder their recombination. Even though the illumination with UV light is still the same, but the amount of photogenerated electrons and holes becomes bigger, the amount of formaldehyde and ·O H radical generated by the oxidation of the holes also increases, but some amount of formaldehyde will be consumed by the oxidation of the free ·OH radicals. As the result, the finally detected amount of formaldehyde is not increasing with the increase of SAW induced electric field, explaining the differences in increase of AC_1 and E_{field} with increasing SAW power. For the metalized SAW chip, E_{field} is smaller because of the screening and attenuation effect of the metal film. At low SAW power, (10mW and 20mW), the SAW-induced electric field is not strong enough to cause significant band bending of TiO_2, at high SAW power (30mW and 40mW), E_{field} become stronger but still remains smaller than that caused by the non-metalized SAW chip at the same SAW power. Hence, the increased reaction rate is not fast

enough to promote further oxidation of formaldehyde, and AC_2 exhibit the same tendency as E_{field}.

4.7 Conclusion

We have performed experiments in which Rayleigh type piezoelectric surface acoustic waves with resonance of 150MHz acts upon well-known Pt/TiO_2 photocatalysts during the photocatalytic of a water splitting reaction with methanol as hole scavenger.

To quantify the SAW-enhanced catalytic efficiency, we employed a Hantzsch reaction to detect the photoexcited hole oxidized formaldehyde production. Here, acetoacetanilide (AAA) with formaldehyde in the presence of ammonia which produces a yellow dihydropyridine derivative product that can be quantitatively detected in a fluorometric measurement. Due to the "doubling effect" of methanol, we can thus approximately determine the amount of H_2 production. Our experimental findings show that the SAW in fact can improve the catalytic efficiency for the methanol photodehydrogenation and it is positive related to the applied SAW power. According to the comparison experiment with non-metalized SAW chip and metalized SAW chip

we argue that the SAW accompanying electric field is most likely the reason for this enhancement. The SAW, being responsible for a dynamic poling of the $LiNbO_3$ substrate, also couples electric fields into the surface deposited Pt/TiO_2 nanoparticle where it induces dynamical band bending and the formation of depletion and accumulation layers in the TiO_2. The photo excited electron-hole pairs are spatially separated by the SAW-induced electric field and band bending of TiO_2, and this efficiently prevents electrons and hole recombination and leads to longer lifetimes of these charge carriers, which finally enhance the photocatalytic reaction.

4.8 References

[1] Q. Li, P. Sritharathikhun, and S. Motomizu, “Development of novel reagent for Hantzsch reaction for the determination of formaldehyde by spectrophotometry and fluorometry,” *Anal. Sci.*, 2007.

[2] R. M. White and F. W. Voltmer, “Direct piezoelectric coupling to surface elastic waves,” *Appl. Phys. Lett.*, 1965.

[3] ákos Kmetykó et al., “Photocatalytic H_2 production using Pt-TiO_2 in the presence of oxalic acid: Influence of the noble metal size and the carrier gas flow rate,” *Materials (Basel).*, 2014.

[4] T. Chen et al., “Mechanistic Studies of Photocatalytic Reaction of Methanol for Hydrogen Production on Pt/TiO_2 by in situ Fourier Transform IR and Time-Resolved IR Spectroscopy,” *J. Phys. Chem. C*, 2007.

[5] Q. Hao, Zhiqiangwang, T. Wang, Z. Ren, C. Zhou, and X. Yang, “Role of Pt Loading in the Photocatalytic Chemistry of Methanol on Rutile TiO_2 (110),” *ACS Catal.*, 2019.

[6] N. Dewan, M. Tomar, V. Gupta, and K. Sreenivas, “Temperature stable $LiNbO_3$ surface acoustic wave device with diode sputtered amorphous TeO_2 over-layer,” *Appl. Phys. Lett.*, 2005.

[7] S. Datta, Surface Acoustic Wave Devices. *Prentice Hall*, 1986.

[8] F. Guzman, S. S. C. Chuang, and C. Yang, “Role of methanol sacrificing reagent in the photocatalytic evolution of hydrogen,” *Ind. Eng. Chem. Res.*, 2013.

[9] N. Hykaway, W. M. Sears, H. Morisaki, and S. R. Morrison, “Current-doubling reactions on titanium dioxide photoanodes,” *J. Phys. Chem.*, 1986.

[10] R. Memming, “Photoinduced charge transfer processes at semiconductor electrodes and particles,” 1994.

[11] C. Wu, V. Y. Zaitsev, and L. V. Zhigilei, “Acoustic enhancement of surface diffusion,” *J. Phys. Chem. C*, 2013.

[12] A. Wixforth, J. P. Kotthaus, and G. Weimann, “Quantum oscillations in the surface-acoustic-wave attenuation caused by a two-dimensional electron system,” *Phys. Rev. Lett.*, 1986

[13] B. Paschke, A. Wixforth, D. Denysenko, and D. Volkmer, “Fast Surface Acoustic Wave-Based Sensors to Investigate the Kinetics of Gas Uptake in Ultra-Microporous Frameworks,” *ACS Sensors*, 2017.

[14] H. Sheng, Q. Li, W. Ma, H. Ji, C. Chen, and J. Zhao, “Photocatalytic degradation of

organic pollutants on surface anionized TiO_2: Common effect of anions for high hole-availability by water," *Appl. Catal. B Environ.*, 2013.

Chapter 5
SAW-tuned electrochemical reaction

The following chapter is based in wide parts on our paper to be submitted publication, entitled "Tunable electrochemical hydrogen evolution reaction employing Surface Acoustic Waves" (citation [18] in Chapter 3).

In this experiment, we alternatively chose Au and Pt modified TiO_2 as non-Pt catalysts for the hydrogen evolution reaction. TiO_2 is a commonly used n-type semiconductor catalyst, and the flat band energy level of its conduction band lies just above the potential of the standard hydrogen electrode. Again, Rayleigh type surface acoustic waves are applied this time to affect the Au electrode and Pt/TiO_2 electrode. Our results demonstrate that under the influence of SAW, both the Au electrode and the Pt-TiO_2 electrode exhibit a better HER activity with a bigger exchange current density and lower overpotential needed to reach a current density of $10mA \cdot cm^{-2}$. Analyzing the Tafel slope and the recorded current with/without the affection of SAW, suggests that the enhanced HER activity of these catalysts can be attributed to the SAW-induced microstreaming effect, which dissipates the electric double layer near the electrode surface, and finally causes a decrease of the free energy of activation (ΔG^*) for the hydrogen evolution reaction. This study might be a first step towards an extensive combination of SAW with different catalysts for electrochemical hydrogen production.

5.1 Preparation of the electrochemical cell

5.1.1 Design and fabrication of Au electrode covered SAW chips

For the SAW chips, we lithographically fabricated a "tapered" interdigital transducer [1] (IDT) of Ti-Au-Ti(5nm-50nm-5nm) on a 17.5mm×17.5mm 128° rotated Y-cut $LiNbO_3$ single crystal substrates, on which the designed two IDT with an aperture of W=1mm and a finger spacing of d=14.6μm. This design results in a SAW resonance frequency of f=68MHz. Then, a 100nm thick SiO_2 layer was sputter-deposited on top of the whole $LiNbO_3$ surface to protect to IDT. On top of the SiO_2, an Au electrode with 1mm×1mm working window was lithographically fabricated between the IDT of the delay line as shown in Fig. 5.1(a).

5.1.2 SAW-based Pt/TiO_2 electrode device

The synthesis method of Pt modified TiO_2 nanoparticle is introduced in Chapter 4.2.1 and the spin coat process to form the Pt/TiO_2 film is the same as described in Chapter 4.2.2

5.1.3 Electrochemical cell

The designed electrochemical cell (EC) is tiny due to the small size of the working electrode window area (1mm×1mm). First, a Teflon cylinder frame with diameter of 1cm is attached to the SAW chip, and the surface of the $LiNbO_3$ substrate with the IDT and the working electrode (WE) acts as the bottom of the EC. The cylinder frame has two functions, one is to contain the aqueous electrolyte and the other is to host the counter electrode and the reference electrode to provide a stable condition for the electrochemical measurement. This small EC can hold approximately 600μL electrolyte solution. The bottom of the EC, except for a window above the working electrode was covered by a thin electrically insulation layer made from S1813 photoresist (MICROCHEM S1813, 2018.10). This S1813 layer also covered the IDT finger pairs to prevent a viscous attenuation effect of the liquid. At last, a cover glass was mounted on top of the EC to prevent the electrolyte solution from contamination and evaporation. An advantage of our designed small size EC is that it enables a short distance between all electrodes, especially between the working electrode and the reference electrode. The schematic structure of the designed electrochemical cell is illustrated in Fig. 5.1(b).

The electrochemical HER activity of the Au electrode and the Pt/TiO_2 electrode samples were characterized by cyclic voltammetry (CV) (see Chapter 2.3.2). An SP200 potentiostate (Bio-logic) is used in our experiments, and a ring-shape platinum wire is used as a counter electrode, and it was set parallel and directly above the WE to ensure a homogenous electric field between them. Ag/AgCl with 3M KCl acts as a reference electrode, but all the potential values following were measured against the reversible hydrogen electrode (RHE) to drive the hydrogen evolution reaction. The electrolyte solution was 0.1M H_2SO_4. Moreover, because of the high proton conductivity of 0.1 H_2SO_4 solution, the iR-correction is neglected in the discussion part.

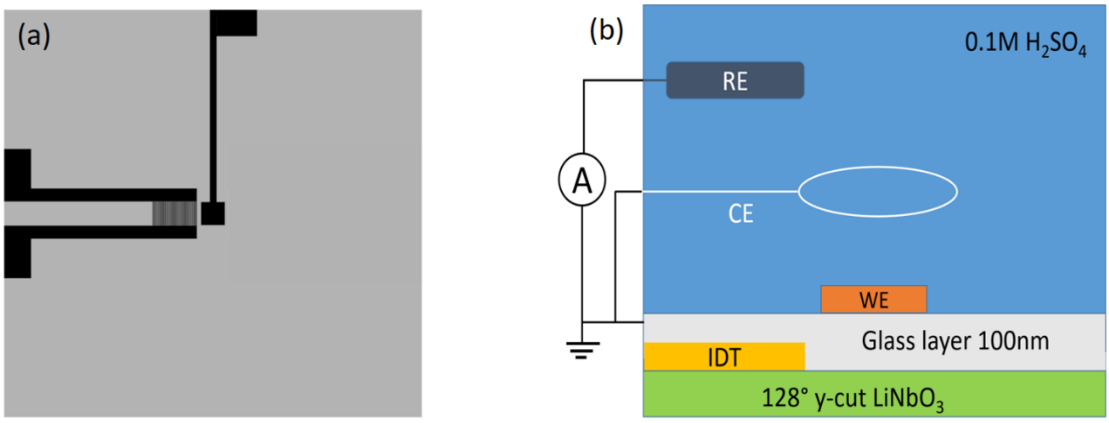

Fig. 5.1 (a) structure of the SAW chip (17.5 mm x 17.5 mm) with IDTs and the working electrode on the delay line. (b) structure of the electrochemical cell, where a ring-shaped platinum wire acts as counter electrode, and an Ag/AgCl electrode acts as reference electrode.

5.1.4 S_{11} signal of IDT

After finishing all preparations, the resonance frequency of the IDT was determined by a vector network analyzer (Rohde & Schwarz), and the S_{11} signal both for the empty EC and the solution filled EC was checked separately. The results of this IDT characterization is shown in Fig. 5.2.

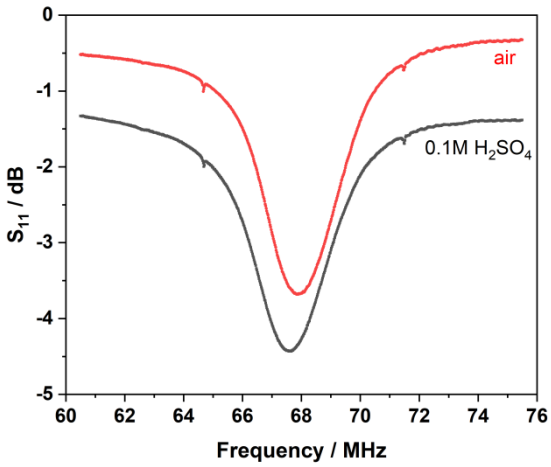

Fig. 5.2 S_{11} signal of IDT under air condition and under 0.1M H_2SO_4 solution.

We can see from Fig. 5.2 the resonance frequency is still located around 67.8MHz under both air and liquid solution, because of the IDT protection by the S1813 film. S_{11} relates the input power to the reflected power as being described in equation (5.1). Hence, we can control the SAW power by controlling the input power according to equation (5.3)

$$S_{11} = 10 \cdot \log(\frac{P_{ref}}{P_{in}}) \tag{5.1}$$

$$P_{in} = P_{ref} + P_{SAW} \tag{5.2}$$

$$P_{SAW} = P_{in}(1 - \frac{1}{10^{\frac{|S_{11}|}{10}}}) \tag{5.3}$$

Here P_{in} is the input power, $P_{ref}$is the reflected power and P_{SAW} is the output SAW power, and their unit are watt.

5.2 Electrochemical testing and analyzing of the Au electrode

The SAW combined cyclic voltammetry testing was conducted by two different methods, separately. In Method 1, a certain, constant SAW power was applied during one CV cycle, and in Method 2, a certain alternating power of the SAW was used in one CV cycle.

5.2.1 Testing and analyzing of the Au electrode -Method 1

Method 1: SAW being applied during one whole CV cycle

First, cyclic voltammetry scans from V=0 to -550mV were performed for around N=30 cycles in order to reach an established equilibrium. Then, the frequency generator was turned on to generate and launch a surface acoustic wave to influence the gold electrode. At the same time, the cyclic voltammetry (CV) curve was recorded. After one CV cycle with SAW being present, the frequency generator was turned off and the cyclic voltammetry still ran for around 5 cycles to reach equilibrium again. These processes were carried out continuously and the power of SAW were applied at P_{SAW}=10mW, 20mW, 30mW, 40mW, 50mW and 60mW, separately. The results are shown in Fig. 5.3. In order to highlight the differences in the curves, the polarization curves are only presented from V=0 to V=-450mV. All polarization curves with an overpotential range from 0 to 450mV under equilibrium condition are shown in Fig. 5.4(a).

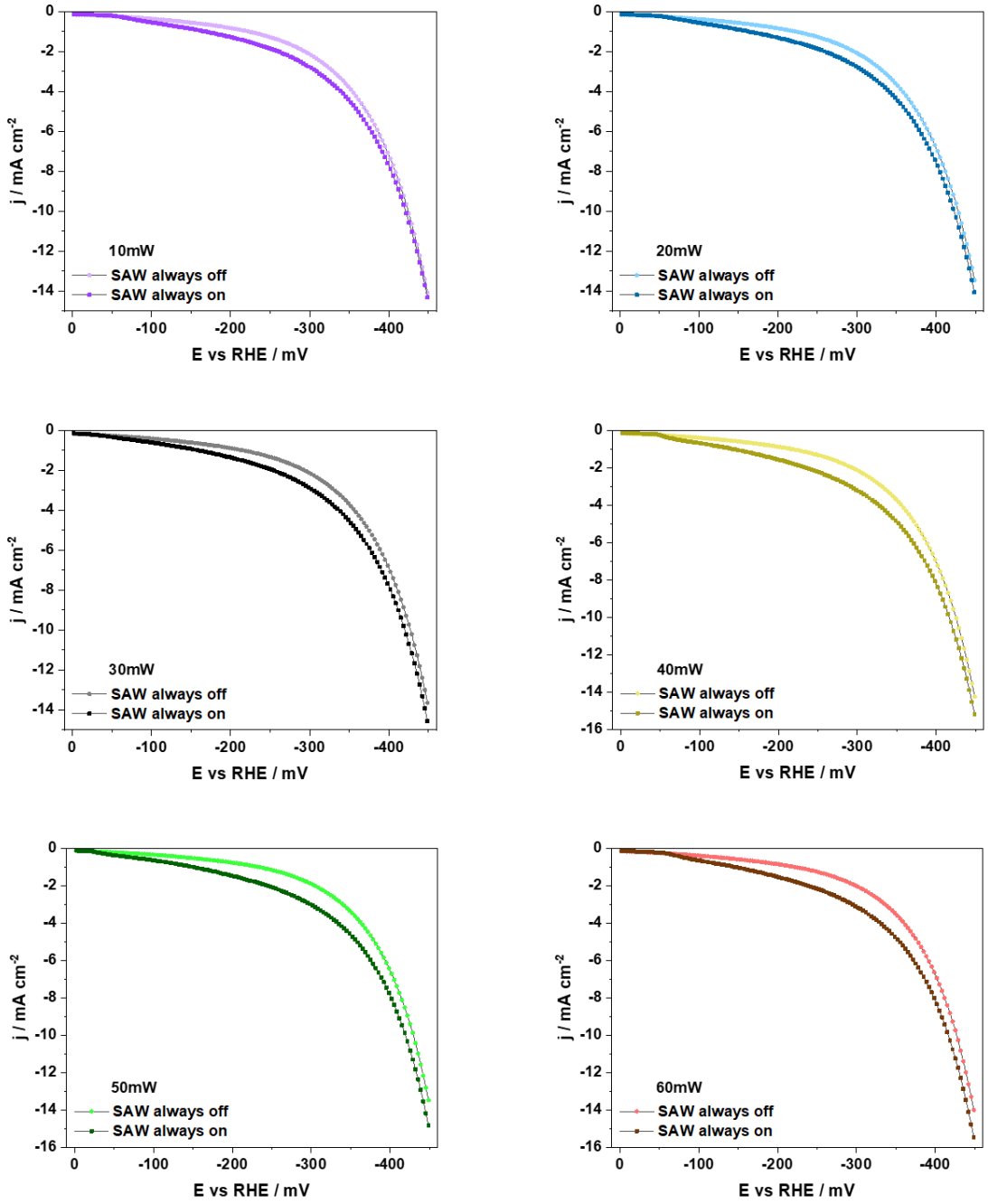

Fig. 5.3 SAW power dependent polarization curves of the gold electrode under constant influence of SAW. The SAW power was applied in P_{SAW}=10mW, 20mW, 30mW, 40mW, 50mW and 60mW, separately. Current density under the influence of different SAW power are depicted in different colors. In one picture, the current density which was recorded under the influence of SAW was displayed in dark color and the one recorded under equilibrium condition was displaced in light color. All the displayed polarization curves were taken in the forward scan (from 0V to -0.45V vs RHE). Cyclic voltammetry scan rate: v = 15mVs^{-1}. Electrolyte: 0.1M H_2SO_4.

The current density indicates how fast an electrochemical reaction happens: The higher the current density, the faster the electrochemical reaction. In the overpotential range between 0mV to -450mV, the current density under SAW influence is larger than the current density without

the influence of SAW, so we can deduce that the surface acoustic wave promotes the electrochemical reaction and thus also enhances the catalytic activity of Au.

When we put all these "SAW always off" polarization curves together in the figure 5.4(a), even though the interval of each "SAW always off" polarization curves covered around 5 cycles, they almost look identical. This indicates that after several cycles of cyclic voltammetry scan without applied SAW, the system can reach its equilibrium condition again. Moreover, this underlines the good reproducibility of the equilibrium current. As a result, these "SAW always off" polarization curve in Fig. 5.3 can be treated as reference.

The overpotential needed to reach a current density of j = 10 $mA \cdot cm^{-2}$ is often used for a quantitative comparison of the catalytic activity, as j = 10 $mA \cdot cm^{-2}$ is the current density necessary to obtain an efficiency of 12.3% of solar to hydrogen devices in industry. This is the efficiency required for the cost competitive water splitting [2]. The smaller the overpotential is, the more efficient the catalytic process could be. The corresponding overpotentials are extracted from Fig.5.3, and the needed overpotential becomes smaller when the Au electrode is influence by the SAW, so the overpotential decrease under influence of different SAW power levels are depicted in Fig. 5.4(b), where the decrease of overpotential is defined as the difference in overpotential with applied SAW and without applied SAW. The absolute value of this decrease in overpotential increases with increasing SAW power level and suggests a drop of the required energy for initiating the hydrogen evolution reaction and a good catalytic activity of the gold catalyst. Even though gold is not the best catalyst for the hydrogen evolution reaction [3], its catalytic property could be improved by Rayleigh-type Surface Acoustic Waves.

As explained above in more detail (chapter 2.2.5) the Tafel equation describes the dependence of the logarithm of the current density from the applied overpotential for an electrolytic process. Figure 5.4(c) show the log(-j) versus overpotential curves of all 'SAW off' and 'SAW on' measurements. Analyzing the Tafel slope allows a deeper understanding of the effect of SAW to the HER system. From Fig. 5.5(c), we can see that these Tafel slope values are bigger than 120 mV/dec for the HER. This indicates that the Volmer step is the rate limiting process of the hydrogen evolution reaction, which describes the process that the proton in solution was adsorped on the surface of the catalyst, $H^+(aq) + e^- \rightarrow H^*$ (Volmer step). Moreover, it is obvious that all 'SAW off' and 'SAW on' measurement have similar tafel slope values for the high overpotential range (-400mV to -550mV), and they have significant different Tafel slope

values at low overpotential range (-100mV to -300mV), where the Tafel slopes of 'SAW off' measurements are around 290mV/decade and the Tafel slopes of 'SAW on' measurements are around 317mV/decade. The big difference of Tafel slope value indicates that the SAW has big influence on the Au electrode at low overpotential, whereas it does not show a significant influence at high overpotential. The fact, that the Tafel slope values of the SAW influenced HER are bigger than the Tafel slope value of normal HER, indicates that the Volmer step becomes slower [4], and the slower Volmer step might appear due to the SAW induced streaming effect. Rayleigh acoustic waves have a mechanical displacement normal to the surface of the $LiNbO_3$ substrate. When the wave comes in contact with the liquid phase, the normal displacement will among others cause tangential fluid motion along the interface, and lead to liquid circulation near it. This phenomenon is called the acoustically induced streaming effect [5]. The Au electrode, which was deposited on the surface of $LiNbO_3$, will not affect the mechanical movement of SAW very much, therefore, the SAW streaming effect still exists, and causes fluid motion hindering the movement of protons directly toward the surface of Au electrode. Thus the proton adsorbing process from the liquid to the catalyst surface becomes slower, which leads to a larger Tafel slope. As we can see in the picture 5.4(c), the Tafel slope difference between SAW influenced HER and normal HER are very big at low overpotential, and the difference becomes smaller at high overpotential. This phenomenon might be caused by the varied diameter of hydrogen gas bubbles and the wavelength of the SAW, which is 50μm in my experiment on the chip. The hydrogen evolution reaction is a half-cell reaction in water electrolysis to produce hydrogen gas, and the first step is the adsorption of protons on the catalyst surface, then electrons will be transformed from the catalyst electrode to them, and electrochemical reaction takes pace to make protons to form hydrogen gas. At low polarization, because of the slow electrochemical reaction rate, the amount of produced gas bubbles is very little and the diameter of these bubbles are very tiny. Even though these hydrogen bubbles adhere at the surface of the electrode, they don't affect the SAW streaming effect too much when its diameter is smaller than the wavelength of SAW. The movement of protons towards the Au electrode surface could be significantly hindered. The situation is different at high overpotential, because of the fast electrochemical reaction rate, there are a lot of hydrogen gas bubbles produced with a larger diameter that becomes equal or bigger than the wavelength of the SAW. Since gas can be easily compressed these hydrogen bubbles which adhere to the surface of the electrode will behave like air cushions and will alleviate the SAW streaming effect very much. Weaker SAW streaming means less hindered proton movement, what is in

accordance with the fact that the value of the SAW influenced Tafel slope is close to the value of the Tafel slope without SAW influence.

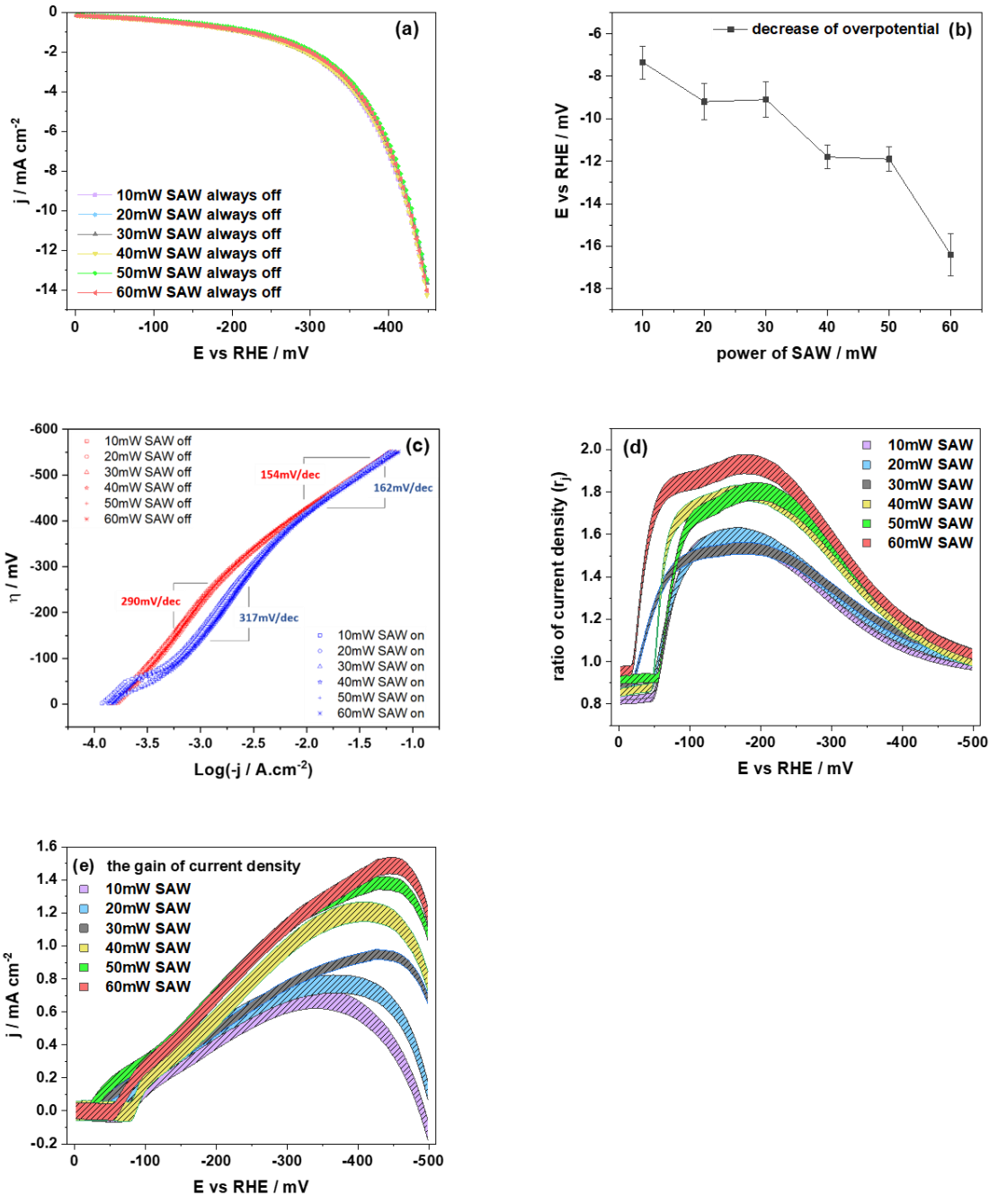

Fig. 5.4 (a) polarization curves of Au electrode under equilibrium conditions for data from Fig. 5.3. The according cycle numbers of "10mW SAW off", "20mW SAW off", "30mW SAW off", "40mW SAW off", "50mW SAW off", "60mW SAW off" is 68, 73, 78, 83, 88 and 93 respectively. (b) overpotential decrease for j = 10mA·cm^{-2} when SAW was used compared with the equilibrium condition without SAW. (c) log(-j) versus polarization curves of all 'SAW off' and 'SAW on' measurements. (d) ratio of current density r_j for different SAW power, calculated from data in Fig. 5.3 and equation (5.11); (e) gain of the current density from E=0 to -500 mV polarization under the influence of different SAW power levels; the stripes indicate the uncertainty of these measurements.

Except for the Tafel slope, the exchange current density (j_0), which is the current density at zero overpotential, is also an important parameter in the Tafel equation. It reflects the intrinsic rate of electron transfer between the electrode and the surrounding electrolyte and critically depends on the nature of the electrode. The logarithmic form of the exchange current density ($\log(j_0)$) can be extracted from the intersection of the linear extrapolation and the ordinate. From figure 5.4(c) we can see that the exchange current density $\log(j_0)$ for 'SAW on' is bigger than the $\log(j_0)$ for 'SAW off'. The more active the surface of the electrode is, the bigger the exchange current density becomes and the lower the energy barrier that the electron must overcome for moving between electrolyte and catalyst surface. In other words, the more current is generated at the same overpotential [6]. The decreased energy barrier could also due to the acoustic stream effect, as this effect can disturb the electric double layer in the acid solution near the electrode surface. The free energy of activation (ΔG^*) for the hydrogen evolution reaction includes the work for transferring the solvated proton from the outer to inner Helmholtz layer (W_{H^+}), according to the equation

$$\Delta G^* = \Delta G_{desorp} + W_{H^+} + \Delta G_{desolv} + \emptyset^* \quad (5.4)\ [7]$$

where ΔG_{desorp} is the desorption energy of the water molecules from the metal surface, ΔG_{desolv} the partial solvation energy of the proton and $\emptyset^*$ is the energy to transfer the electron through the metal/solvent interface.

Once the electric double layer is disturbed, the electric field in the double layer becomes weak, this leads to a smaller value of $W_{H^+(SAW)}$ and then decreases the activation energy to

$$\Delta G^* = \Delta G_{desorp} + W_{H^+(SAW)} + \Delta G_{desolv} + \emptyset^* \quad (5.5)$$

The decrease of the activation energy ΔG^*leads to an increase of the electron transfer according to a semi-classical treatment, where

$$k_{et} = \kappa_{el} \Gamma_n \upsilon_n \exp(-\frac{\Delta G^*}{RT}) \quad (5.6)\ [6]$$

Here, k_{et} is the electron transfer rate, κ_{el} is the electronic transmission coefficient ($\kappa_{el} \leq 1$) , Γ_n is the nuclear tunneling factor ($\Gamma_n \geq 1$), and υ_n is the nuclear frequency factor.

The first-order rate constant k can be related to the electron transfer rate k_{et} by equation (5.7)

$$k = \frac{1}{c_{ox}^0} \int k_{et}(z) c_{ox}(z) dz \quad (5.7)$$

Where c_{ox}^{0} is oxidant concentration in the bulk of solution, z refers to a distance perpendicular to the electrode surface, and $c_{ox}(z)$ refers to the oxidant concentration between the electrode surface to the bulk of solution [8].

Under standard conditions, the activation energy can be expressed as

$$k_0 = k' \exp\left(-\frac{\Delta G_0^*}{RT}\right) \tag{5.8}$$

With k' is a pre-exponential factor. The SAW-caused streaming could decrease the activation energy ΔG_0^* and enhance the rate constant k_0, which leads to a higher exchange current density j_0, since

$$j_0 = k_0 c_{H^+} \exp\left[-\frac{\alpha e(U_{redox} - U_{redox}^0)}{RT}\right] \tag{5.9}$$

where α is always equal to 0.5, c_{H^+} is the concentration of proton, and $e(U_{redox} - U_{redox}^0) = \Delta G_+^* - \Delta G_-^*$ is the energy difference between activation energy of forward reaction and backward reaction [8]. As a result, the bigger log(j_0) value for all 'SAW on' measurements may due to the SAW-caused streaming effect, which disturbed the electric double layer and decrease the free activation energy.

In figure 5.4(c) we can see that the for low polarizations (-150mV to -300mV) is different from the current density at high polarization (-400mV to -550mV), so different values of both, Tafel slope and log(j_0) are obtained at low polarization and high polarization, respectively. At low overpotential, the log(j_0) for all 'SAW off' are around log(j_0) =-3.77 and log(j_0) for all 'SAW on' are around log(j_0) =-3.48. At high polarization, the log(j_0) for all 'SAW off' are around log(j_0) =-4.77 and log(j_0) for all 'SAW on' are around log(j_0) = -4.57. The fact that the difference between the log(j_0, saw off) and the log(j_0, saw on) becomes smaller at high overpotentials might be a consequence of the appearance of lots of hydrogen bubbles with big diameter at the surface of the electrode at high overpotentials. These bubbles damp the acoustic steaming more efficiently and the electric double layer formed several nanometers above the gas bubble is only slightly disturbed by the SAW streaming. This lead to a small decrease of the activation energy (ΔG^*) due to the work of W_H^+ needed. Thus the decrease of the activation energy is less significant, which explains that the value of log(j_0, saw on) is closer to the value of log(j_0, saw off).

The change of the current density j_0 can be also proven by 'the ratio of current density(j)' between 'SAW on' and 'SAW off', and the 'ratio of j' is defined by equation (5.11). Since the

diffusion of protons is sufficiently fast, the current density can be expressed by a simple form of the Butler-Volmer relation:

$$j = j_0 \left[\exp(\frac{(1-\alpha)e\eta}{RT}) - \exp(-\frac{\alpha e\eta}{RT})\right] \quad (5.10)$$

where η is the polarization. If we compare the current density at the same polarization, then the ratio of the current densities r_j can be written as the ratio of the exchange current densities j_0. Since j_0 relates to the rate constant k_0 according to equation (5.9), and in combination with the equations (5.8), (5.4) and (5.5), r_j can be written as follows:

$$r_j := \frac{j(SAW\ always\ on)}{j(SAW\ always\ off)} = \frac{j_0(SAW\ always\ on)}{j_0(SAW\ always\ off)} = \exp(\frac{W_{H^+} - W_{H^+(SAW)}}{RT}) \quad (5.11)$$

here, r_j as function of SAW power can reflect the influence of the SAW power to increase of the exchange current density and indicates the decrease of the activation energy by SAW. The resulting r_j curves are shown in figure 5.4(d).

Before the SAW was turned on, the r_j is constant at a distinct value in a range between r_j =0.8 to 1 for each SAW power, theoretically it should hold r_j =1. The deviation might be caused by a measuring error. Then when the SAW was turned on, r_j rises sharply for all different SAW power levels applied. indicating that the SAW streaming effect disturbs the electric double layer strongly, and the energy of $W_{H^+(SAW\ on)}$ is almost zero between E = -100mV to -250mV. At higher overpotentials r_j decreases gradually to r_j =1 from -250mV to -500mV. The decrease of r_j might due to the gas bubble damped SAW streaming effect, as explained above, which lead to a big value of $W_{H^+(SAW\ on)}$, that approaches towards the value of $W_{H^+(SAW\ off)}$ with increasing overpotential. Thus, r_j becomes more and more close to r_j =1. From the change of r_j, we can conclude that the SAW enhanced current density may due to the decrease of the activation energy by SAW streaming.

Moreover, comparing r_j for P_{SAW}=10mW and P_{SAW}= 60mW shows an increase of r_j as the SAW power increases. This again can be understood by increase of streaming velocity and thus disturbance of the electric double layer, which lead to a more significant decrease of $W_{H^+(SAW\ on)}$.

The gain of current density is shown in figure 5.4(e). Here, the gain of the current density is defined as the absolute value of the current density under the influence of SAW HER minus the current density of the normal HER. Since the diffusion of the protons toward the electrode

surface is sufficiently fast, the current-potential dependence can be expressed by the simple form of the Butler-Volmer equation (5.10), so

the current gain = $j_{(SAW\ on)} - j_{(SAW\ off)}$

$$= (j_{0(SAW\ on)} - j_{0(SAW\ off)}) \times \left[\exp(\frac{(1-\alpha)e\eta}{RT}) - \exp(-\frac{\alpha e\eta}{RT})\right] \quad (5.12)$$

It is obvious in figure 5.4(e) that the gain of current density for all applied SAW power levels show the same tendency: first it increases with the rise of the negative polarization from 0 to -400mV, then after reaching its maximum value, it decreases when the polarization further increases. As we have analyzed before, because of effective SAW streaming effect at the low overpotential range, the value of $j_{0(SAWon)} - j_{0(SAWoff)}$ is relative big, so the current gain increases sharply with the increase of polarization; at high overpotential range, big hydrogen bubbles damped the SAW streaming effect, and lead to a decrease of the value of $j_{0(SAWon)} - j_{0(SAWoff)}$, but the polarization increases all the time, so at the polarization around -400mV, the current gain will reach its maximum value. From -400 to -500mV, the value of $j_{0(SAWon)}$ gets more and more close to the value of $j_{0(SAWoff)}$, so the decrease of $j_{0(SAWon)} - j_{0(SAWoff)}$ will dominant the change tendency of the current density gain. Figure 5.4(e) also obviously shows that when higher SAW power is applied, a higher gain of current density will be obtained. This in turn is in accordance with the assumption that a SAW streaming effect is the main underlying mechanism here.

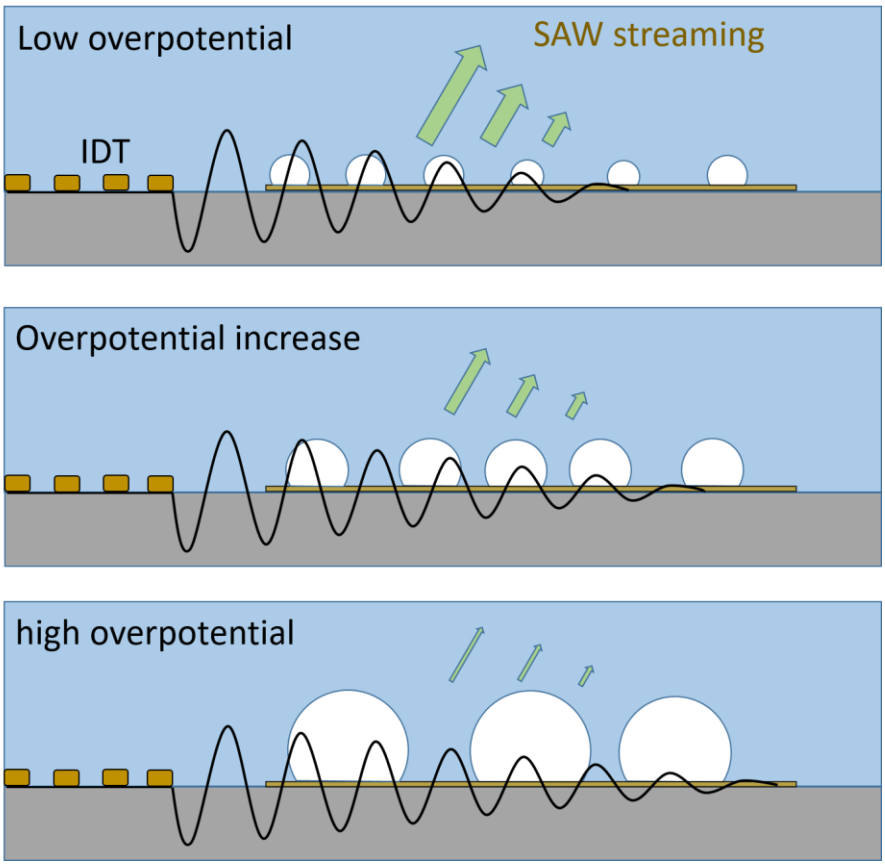

Fig. 5.5 Illustration of the relationship between SAW streaming effect and the diameter of the produced hydrogen bubbles. At low overpotential, the SAW streaming effect is not damped very much by these small bubbles, when the overpotential increases the SAW streaming effect become less and less due to the bigger diameter of the gas bubbles.

5.2.2 Testing and analyzing of the Au electrode -Method 2

Method 2: SAW was turned on and off in one CV cycle

In order to prove that actually the SAW increases the current density in the electrochemical experiment, the applied SAW was turned on and off in one cycle. At first, the cyclic voltammetry scan has to run 30 cycles to reach equilibrium, then the frequency generator was turned on and off alternatively for 45seconds within each cycle. When the frequency generator was turned on, surface acoustic waves were generated and influenced the gold electrode; when the frequency generator was turned off, the SAW disappeared immediately and electrode was again under undisturbed conditions. Fig. 5.6 shows all separately recorded CV curves under the influence of SAW for applied power levels of P_{SAW} = 10mW, 20mW, 30mW, 40mW, 50mW and 60mW.

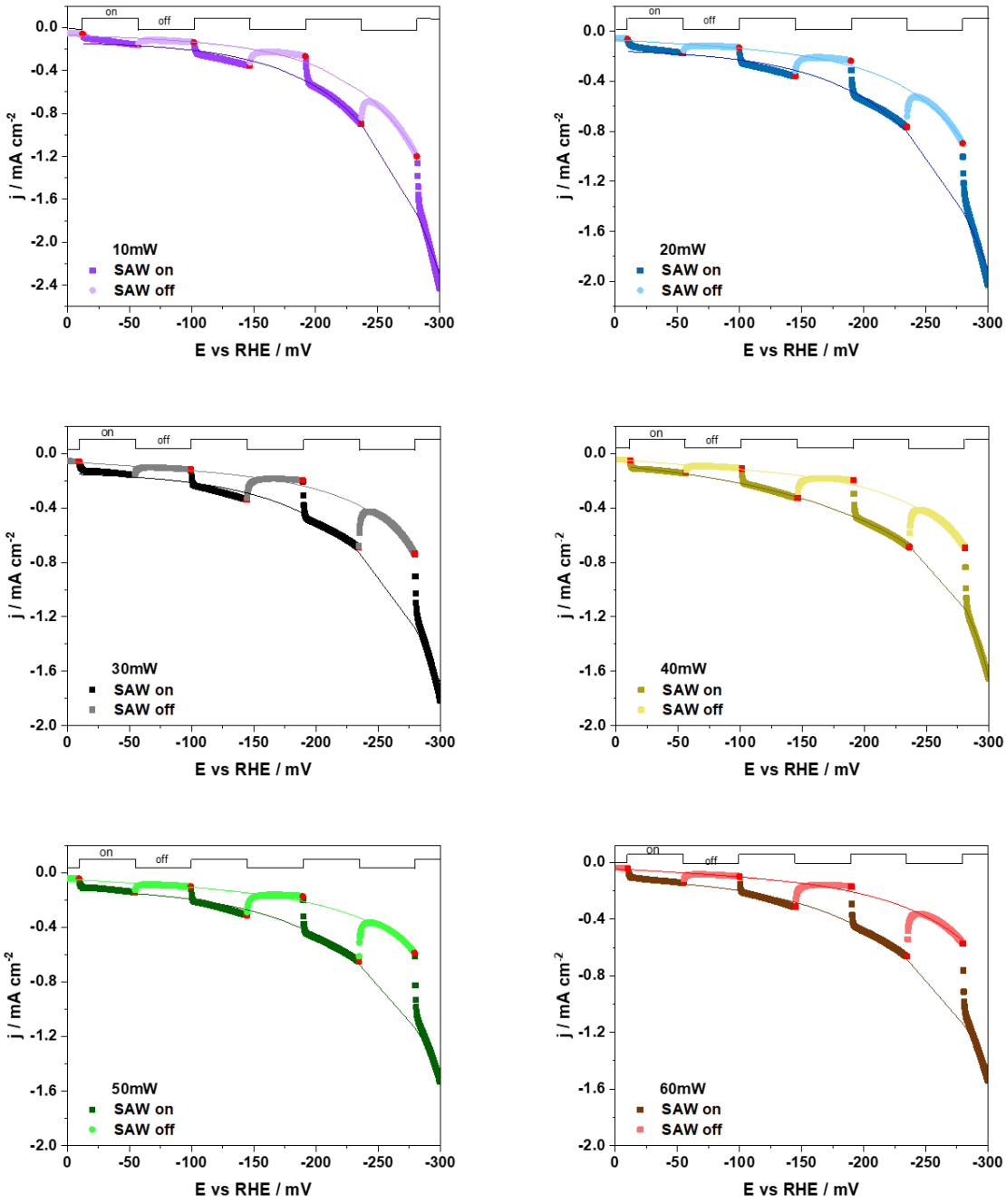

Fig. 5.6 SAW power dependent polarization curves of a gold electrode alternating with and without the influence of SAW. The SAW power was applied with P_{SAW} = 10mW, 20mW, 30mW, 40mW, 50mW and 60mW separately. The current density under the influence of different of SAW power are shown in different colors. In one scan, the current density which was recorded under the influence of SAW is displayed in dark color and the one recorded without the influence of SAW is shown in light color. The black line on the top represents the periodic switching on and off of the SAW. All the displayed polarization curves were taken in the forward scan (from 0V to -0.3V vs RHE). Cyclic voltammetry scan rate: v = 1mV·s^{-1}. Electrolyte: N_2 saturated 0.1M H_2SO_4. The red point in each polarization curve indicate the switch of SAW.

It is obvious that the current density jumps to higher value when the electrode was affected by SAW, and it jumps back to lower values when the SAW was turned off. The jump of the current density in one polarization curve directly indicate that the increase of j is caused by the SAW. As analyzed before, the SAW induced streaming effect could decrease the activation energy and then promote electron transfer rate and finally lead to an increase of the hydrogen production rate. Both the SAW-affected current density and the SAW-unaffected current density have the same shape, and can be fitted by using the Butler-Volmer equation separately, and the results are shown in Table. 5.1. Comparing the two fitted Butler-Volmer curves, allow for quantification of the SAW power dependent r_j from 0V to -0.3V. as shown in Fig. 5.7.

Table. 5.1 the Butler-Volmer equation fitted SAW-affected current and the SAW-unaffected current.

	Butler-Volmer equation	correlation coefficient value
10mW SAW off	$j = -0.06596 - 0.00646\exp(-\frac{E}{55.38})$	0.98999
10mW SAW on	$j = -0.13028 - 0.0154\exp(-\frac{E}{60.6})$	0.99189
20mW SAW off	$j = -0.06558 - 0.00232\exp(-\frac{E}{50.62})$	0.98538
20mW SAW on	$j = -0.14164 - 0.01946\exp(-\frac{E}{66.61})$	0.98942
30mW SAW off	$j = -0.06058 - 0.00143\exp(-\frac{E}{47.83})$	0.97329
30mW SAW on	$j = -0.133 - 0.0189\exp(-\frac{E}{68.07})$	0.9907
40mW SAW off	$j = -0.03986 - 0.00346\exp(-\frac{E}{56.08})$	0.98075
40mW SAW on	$j = -0.10228 - 0.0256\exp(-\frac{E}{74.41})$	0.99787
50mW SAW off	$j = -0.04452 - 0.000258\exp(-\frac{E}{55.66})$	0.98735
50mW SAW on	$j = -0.10136 - 0.024568\exp(-\frac{E}{74.74})$	0.96729
60mW SAW off	$j = -0.04264 - 0.00322\exp(-\frac{E}{58.26})$	0.9226
60mW SAW on	$j = -0.09246 - 0.03032\exp(-\frac{E}{79.04})$	0.97226

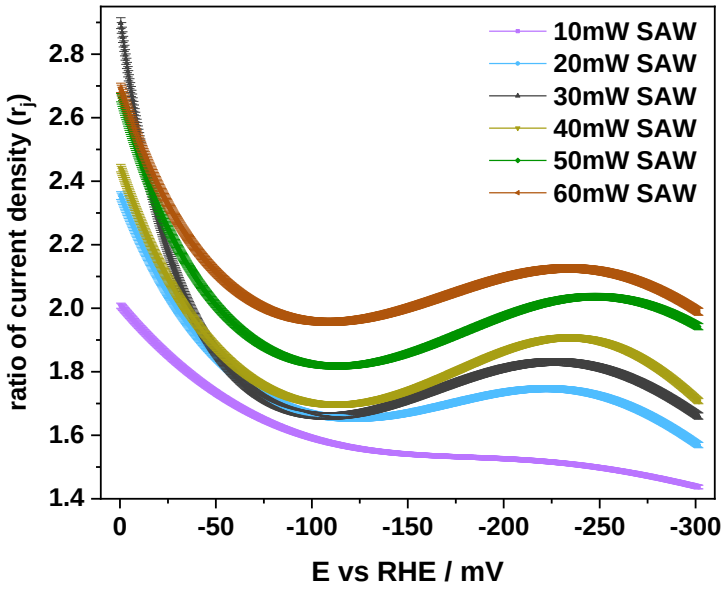

Fig. 5.7 ratio of current density r_j for different SAW power level within one polarization curve, and the data of j are obtained from 'SAW on' and 'SAW off' fitted Butler-Volmer equation.

It clearly shows that the value of r_j positively correlates with the applied SAW power. This can be understood along the same lines as discussed above (chapter 5.2.2.)

5.3 Electrochemical testing of an Au supported Pt/TiO_2 electrode

For an Au supported Pt/TiO_2 electrode, all the electrochemical testing employing method 1 and method 2 are performed in the same way as for the Au electrode, and the polarization curve with 10mW SAW power to 60mW SAW power are shown in Fig. 5.8 and Fig. 5.9.

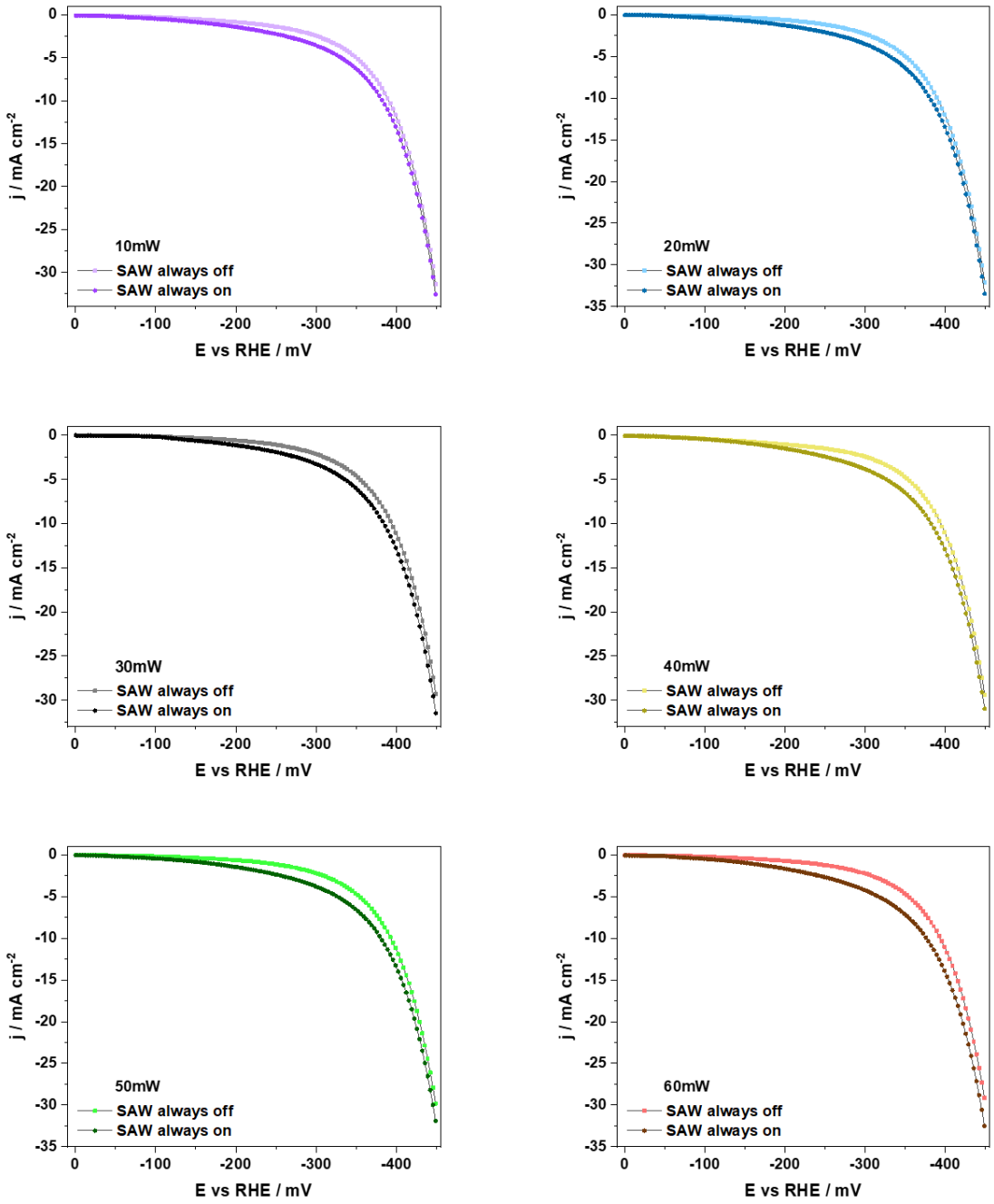

Fig. 5.8 SAW power dependent polarization curves of Au supported Pt/TiO_2 electrode under the constant influence of SAW. The applied SAW power levels P_{SAW} = 10mW, 20mW, 30mW, 40mW, 50mW and 60mW were recorded separately. In each graph, the current density recorded under the influence of SAW is shown in dark color and the one recorded under equilibrium conditions is shown in light color. All the displayed polarization curves were taken in the forward scan (from 0V to -0,45V vs RHE). Cyclic voltammetry scan rate: v = 15mVs^{-1}. Electrolyte: 0.1M H_2SO_4.

Figure 5.8 shows the current density curves for a SAW affected Au supported Pt/TiO_2 electrode. The increase of the current density is more significant for P_{SAW} =60mW SAW. All these 'SAW always off' polarization curves in figure 5.10(a) are similar, which shows the high

reproducibility of the equilibrium current. Similar as shown for the Au-electrode above there again is a big difference between the 'SAW always on' and the 'SAW always off' curves. This indicates that SAW application here increases the current density of the Pt/TiO_2 electrode. This phenomenon becomes even more obvious as shown in figure 5.9, where the current density increases immediately when the SAW is turned on, and it jumps back when the SAW is turned off.

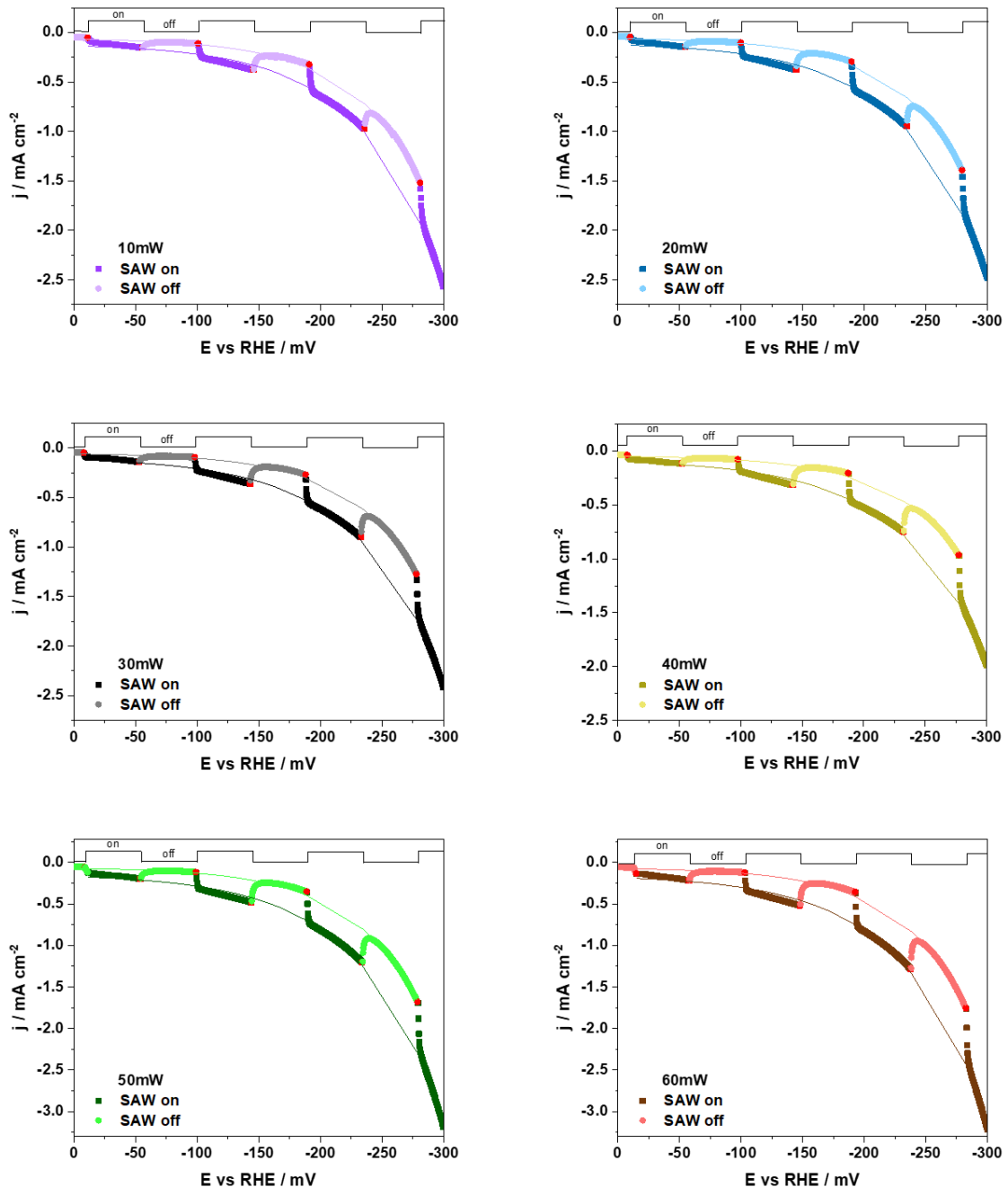

Fig. 5.9 SAW power dependent polarization curves of Pt/TiO_2 electrode under alternative influence of SAW. The SAW power was applied in 10mW, 20mW, 30mW, 40mW, 50mW and 60mW separately. Current density under influence of different of SAW power are showed in different color. In one scan, the current density which was

recorded under influence of SAW was displayed in dark color and the one recorded without disturbance of SAW was displaced in light color. The black line on the top represent the periodic switching of SAW. All the displayed polarization curves were taken in the forward scan (from 0V to -0.3V vs RHE). Cyclic voltammetry scan rate: v = 1mVs^{-1}. Electrolyte: N_2 saturated 0.1M H_2SO_4. The red point in each polarization curve indicate the switch of SAW.

Table. 5.2 the Butler-Volmer equation fitted SAW-affected current and the SAW-unaffected current.

	the Butler-Volmer equation	correlation coefficient value
10mW SAW off	$j = -0.05572 - 0.01165\exp(-\frac{E}{58.38})$	0.99483
10mW SAW on	$j = -0.1117 - 0.02238\exp(-\frac{E}{63.93})$	0.99741
20mW SAW off	$j = -0.05071 - 0.01036\exp(-\frac{E}{57.68})$	0.99418
20mW SAW on	$j = -0.09949 - 0.02553\exp(-\frac{E}{66.24})$	0.99731
30mW SAW off	$j = -0.0498 - 0.00971\exp(-\frac{E}{57.65})$	0.99308
30mW SAW on	$j = -0.09374 - 0.02666\exp(-\frac{E}{67.53})$	0.99627
40mW SAW off	$j = -0.03152 - 0.00847\exp(-\frac{E}{59.34})$	0.98713
40mW SAW on	$j = -0.07838 - 0.02479\exp(-\frac{E}{69.57})$	0.99423
50mW SAW off	$j = -0.0572 - 0.0131\exp(-\frac{E}{57.99})$	0.99184
50mW SAW on	$j = -0.13982 - 0.03278\exp(-\frac{E}{66.63})$	0.99516
60mW SAW off	$j = -0.06153 - 0.01193\exp(-\frac{E}{57.15})$	0.99106
60mW SAW on	$j = -0.1508 - 0.03372\exp(-\frac{E}{67.05})$	0.99381

Fig. 5.9 shows the current density in one cycle for periodically launched SAW with power levels of P_{SAW}= 10mW to 60mW SAW (according to the electrochemical testing method 2). Obviously, the current density jumps to higher values when the electrode is affected by SAW, and it jumps back to lower values when the SAW is turned off.

5.4 Analyzing the current density of an Au supported Pt/TiO_2 electrode

Figure 5.10(b) shows the decrease of overpotential when 10mW, 20mW, 30mW, 40mW, 50mW, and 60mW SAW power was applied to influence the Pt/TiO_2 electrode. The result demonstrates that with increasing SAW power level less overpotential is needed to reach the current density of $j=10mA\cdot cm^{-2}$. Thus, the SAW can not only improve the catalytic property of an Au electrode, but also enhances the catalytic property of a Pt/TiO_2 electrode.

The Tafel slope values shown in figure 5.10(c) indicate that here the Volmer step is the rate limiting process for the HER on TiO_2. These 'SAW on' and 'SAW off' curves have a significant different Tafel slope value for the low overpotential range, where the Tafel slope values for these 'SAW on' curves are about 306.2 mV/dec and they are about 285.4mV/dec for these 'SAW off' curves. The slower Volmer step for 'SAW on' might also due to the SAW streaming effect, as explained in detail above (5.2.1).

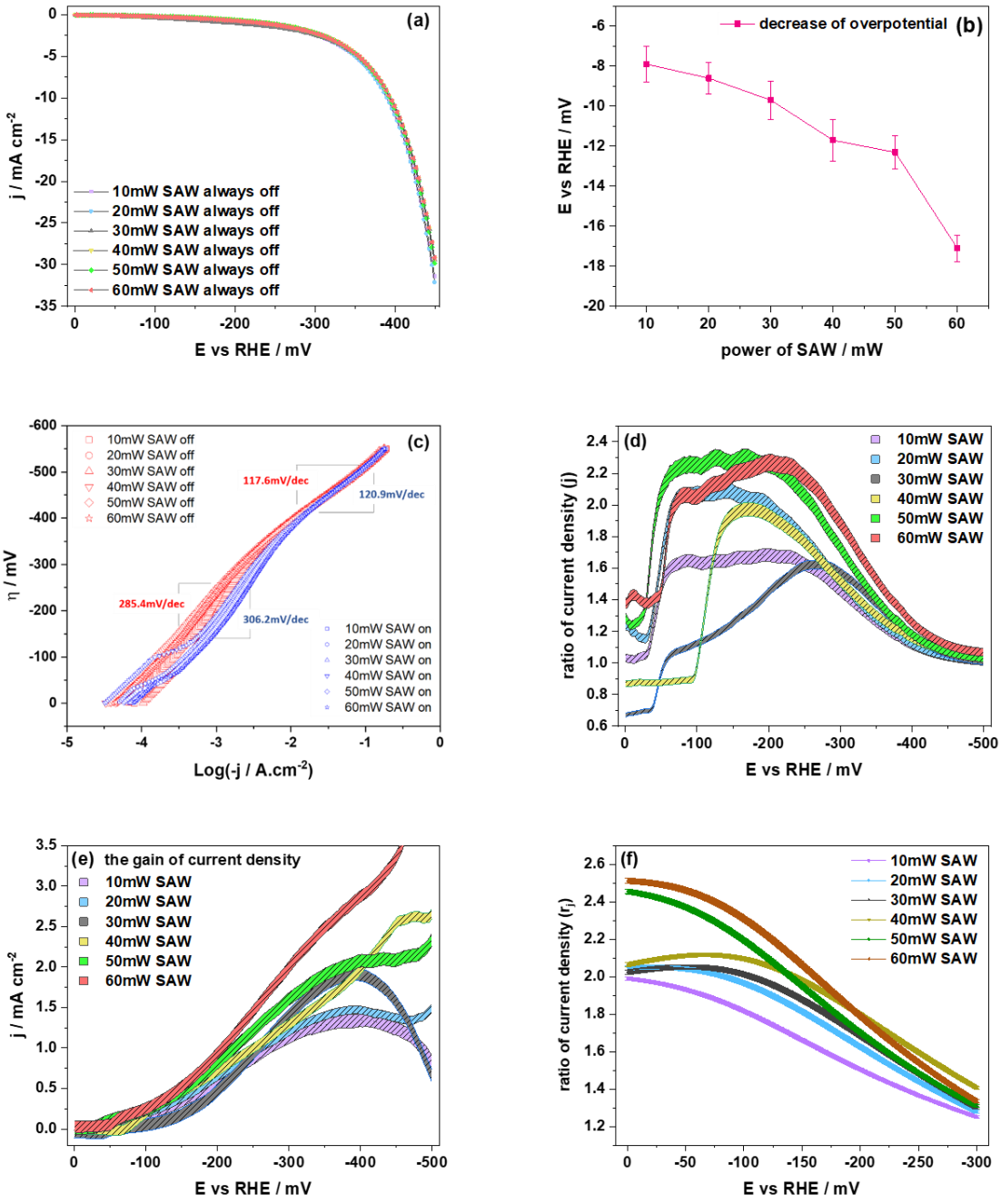

Fig.5.10 (a) Polarization curves of Au supported Pt/TiO_2 electrode under equilibrium conditions, before the SAW was launched with the power level given in the legend. (b) decrease of overpotential to reach 10 mA·cm^{-2} as function of overpotential for various SAW power levels. (c) overpotential as function of log(-j) of all 'SAW off' and 'SAW on' measurements. The values of the Tafel slope are marked (method 1); (d) ratio of current density(j) for different SAW powers (method 1); (e) current density gain from 0 to -500 mV polarization for applied surface acoustic waves of different SAW power. The strip indicates the uncertainty of these measurements (method 1). (f) the ratio of the current density (r_j) for different SAW power calculated from the fitted Butler-Volmer equation with the data gotten from the electrochemical testing method 2.

The current density gain showed in figure 5.10(e) differs from that for the Au electrode shown in the figure 5.5(e). At high overpotentials the current density gain still increases for the Pt/TiO_2

electrode. That phenomenon might due to the SAW-induced mechanical vibration on the Pt/TiO_2 electrode. Comparing figure 5.3 and figure 5.9 we can see that the current density for Pt/TiO_2 electrode is higher than for the Au electrode at the same overpotential. This could be understood by a higher amount of hydrogen bubbles produced on the TiO_2 surface due to the higher activity. The diameter of these bubbles will certainly be relative big. These big bubbles will block the active sites of TiO_2, but they are more easily desorbed by the SAW-induced mechanical vibration due to their big size. Therefore, SAW could help to desorb the big hydrogen bubble and let the blocked active site of TiO_2 to be exposed to the reactant again, and the current density still increases at high overpotential for the Pt/TiO_2 electrode. This was not observed for the Au electrode. A reason could be the lower amount and/or size of produced hydrogen bubbles.

5.5 Conclusion

This experiment impressively has shown that the Rayleigh type SAW enhance the catalytic activity of both Au and Pt/TiO_2, and the overpotential needed to reach a current density of j= $10mA \cdot cm^{-1}$ is decreased by the application of SAW. Moreover, this effect increases with increasing SAW power. By analyzing the mechanism of the electrochemical HER on these two materials, we identified SAW induced acoustic streaming effect as potential main reason for the enhancement of the HER. This streaming effect could dissipate the electric double layer near the surface of the electrode and lead to a decrease of the activation energy. Finally, the HER becomes faster indicated by the increase of the current density under the influence of SAW. Moreover, the effect increases with increasing SAW power. This could be understood as a consequence of the increasing streaming velocity with increasing SAW power and hence a reduction of the work to transfer protons from outer to inner Helmholtz layer more. At high overpotentials, a lot of produced hydrogen bubbles could damp the SAW streaming effect and then cause only a slightly disturbed electric double layer, so the current density gain gradually decreases for the high overpotential range for the Au electrode; however, for Pt/TiO_2 electrode, which produces more hydrogen bubbles at the high overpotential, the aggregated big bubbles can be easily desorbed from the surface of TiO_2 with the help of SAW-induced mechanical vibration. Thus in contrast to the Au electrode here the current density gain still increases in the high overpotential range.

5.6 Reference:

[1] C. Westerhausen et al., “Controllable acoustic mixing of fluidsc in microchannels for the fabrication of therapeutic nanoparticles,” *Micromachines,* 2016.

[2] J. D. Benck, Z. Chen, L. Y. Kuritzky, A. J. Forman, and T. F. Jaramillo, “Amorphous molybdenum sulfide catalysts for electrochemical hydrogen production: Insights into the origin of their catalytic activity,” *ACS Catal.*, 2012.

[3] Y. Wang et al., “Activation Effect of Electrochemical Cycling on Gold Nanoparticles towards the Hydrogen Evolution Reaction in Sulfuric Acid,” Electrochim. Acta, 2016.

[4] Y. Shi *et al.*, “Hot Electron of Au Nanorods Activates the Electrocatalysis of Hydrogen Evolution on MoS2 Nanosheets,” *J. Am. Chem. Soc.*, 2015.

[5] A. Yabe, Y. Hamate, M. Hara, H. Oguchi, S. Nagasawa, and H. Kuwano, “A self-converging atomized mist spray device using surface acoustic wave,” *Microfluid. Nanofluidics,* 2014.

[6] S. Litster and G. McLean, “PEM fuel cell electrodes,” *Journal of Power Sources*. 2004.

[7] A. R. Zeradjanin, A. Vimalanandan, G. Polymeros, A. A. Topalov, K. J. J. Mayrhofer, and M. Rohwerder, “Balanced work function as a driver for facile hydrogen evolution reaction - Comprehension and experimental assessment of interfacial catalytic descriptor,” *Phys. Chem. Chem. Phys.*, 2017.

[8] R. Memming, *Semiconductor electrochemistry*. John Wiley & Sons, 2015.

Summary and future work

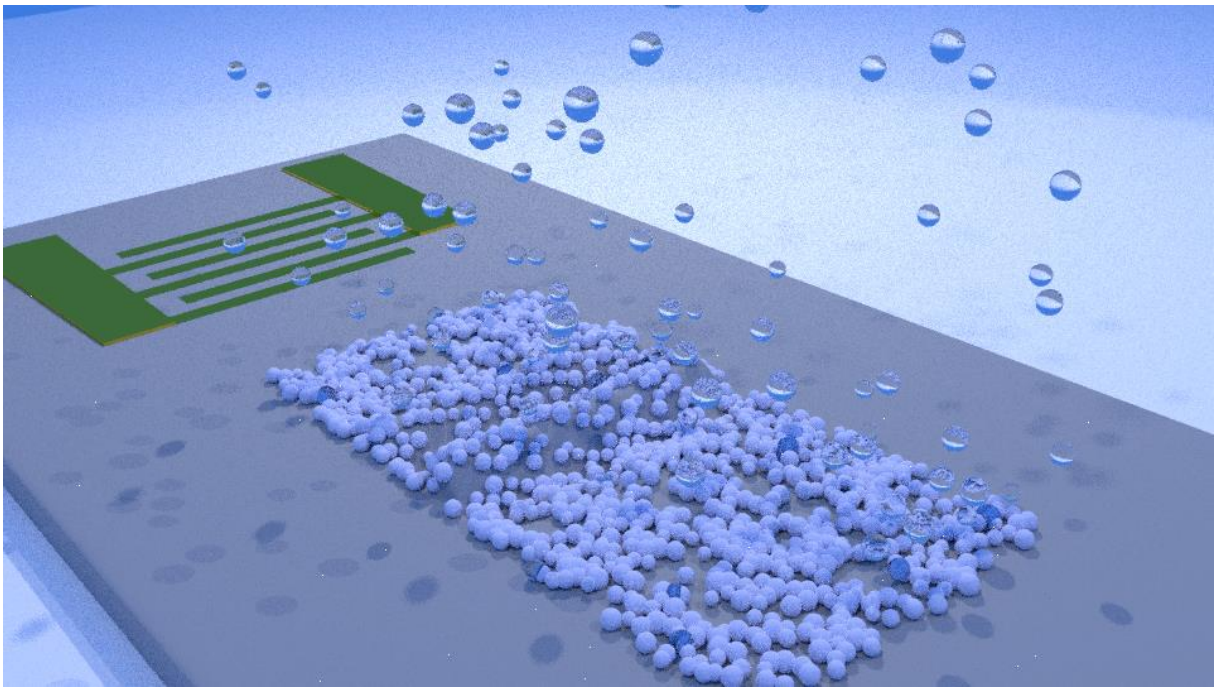

Fig 6.1 Animation simulation of SAW assisted hydrogen evolution reaction by Blender software.

The experiments in this thesis have focused on the application of Rayleigh type surface acoustic waves(SAW) on chemical reactions to produce hydrogen gas, one is the photocatalytic water splitting reaction in the gas phase with methanol as sacrifice material, the other is the electrochemical hydrogen evolution reaction in the 0.1M H_2SO_4 liquid solution. The results revealed that SAW indeed can enhance both reactions. In general, there might be two reasons for the SAW-induced chemical reaction enhancement: one is the mechanical surface vibration accompanying the SAW, and the other are the SAW-caused electric fields on the surface. The propagation of SAW is accompanied by the electric fields, as a consequence of the local surface deformation of the piezoelectric substrate by the SAW.

For the photocatalytic water splitting reaction, methanol was used as a sacrifice material to accelerate the reaction and to quantify the catalytic efficiency. Pt modified TiO_2 was used as photocatalyst and Rayleigh waves with a frequency of f=150MHz were applied to promote the catalytic property of TiO_2. In order to quantify the catalytic efficiency, the produced formaldehyde was detected by the Hantzsch reaction, as it is easier than the direct detection of the hydrogen production. Our experiment results show that 40mW SAW power can enhance

the catalytic efficiency by up to 100%, and the SAW-caused enhancement phenomenon increased with increasing SAW power. Moreover, with reference experiments we narrowed down the SAW accompanying electric fields as most likely reason for the enhancement of the chemical reaction. The SAW-induced electric field could interact with electric band structure of TiO_2 and induce dynamic band bending and format depletion and accumulation layers in TiO_2, drive photo-excited electrons and holes into opposite directions and prolong their life time.

For the electrochemical hydrogen evolution reaction, Rayleigh waves also enhanced the catalytic activity of Au and Pt/TiO_2. The overpotential needed to reach a distinct current density was significantly decreased by the application of SAW. Moreover, the effect increases with increasing SAW power level. By analyzing the mechanism of the electrochemical HER on these two materials, we concluded that the surface mechanical vibration is the main reason. Rayleigh type SAW have a vertical displacement normal to the surface, and this displacement causes liquid streaming effects, which could dissipate the electric double layer near the surface of the electrode and lead to a decrease of the activation energy. Finally, the HER becomes faster which is indicated by the increase of current density under the influence of SAW.

In our research, we found that the mechanism for the SAW assisted chemical reaction for these two reactions are different, because the phases of these reactants are different. The photocatalytic water splitting reaction is in the gas phase, while the electrochemical hydrogen evolution reaction is liquid solution In general, we found that surface acoustic wave can enhance the catalytic property of Pt/TiO_2 catalyst, and increase the produced amount of hydrogen gas, when the chemical reaction happens in gas phase, SAW-induced electric field will play an important role to enhance the phototcatalyst, and when the chemical reaction happens in liquid phase, the SAW-induced mechanical vibration will become the main reason for the promoted chemical reaction. In liquid phase, the SAW-caused electric field could not play a big role, because the liquid damping is very serious. SAW can only travel 10-12 wavelength, and the amplitude of mechanical vibration exponentially decay, and the attenuated SAW amplitude leads to very small electric fields, so the intensity of the electric field acting on the catalyst and the affected area are very small. However, the SAW streaming effect is different, due to the mobility of water, the liquid streaming effect is still very significant even though it is far from the IDT, so we argue that many of our catalysis enhancing observations are caused by the SAW streaming effect, a statement that has to be confirmed in the future,

though, by e.g. measuring the SAW streaming effect as a function of the bubble size and surface coverage. However, in the gas phase, i.e. at the location of a bubble, there is no liquid damping, so SAW-induced vibration and SAW-accompanying electric fields could be the reason, for band bending of the semiconducting TiO_2.

This opens up a whole new field of applications. Promising future work should cover both, a variation of the SAW frequency and wave type. Other types of SAW than Rayleigh waves, for example shear waves could influence larger areas of catalyst on the surface, as the attenuation length is much longer.